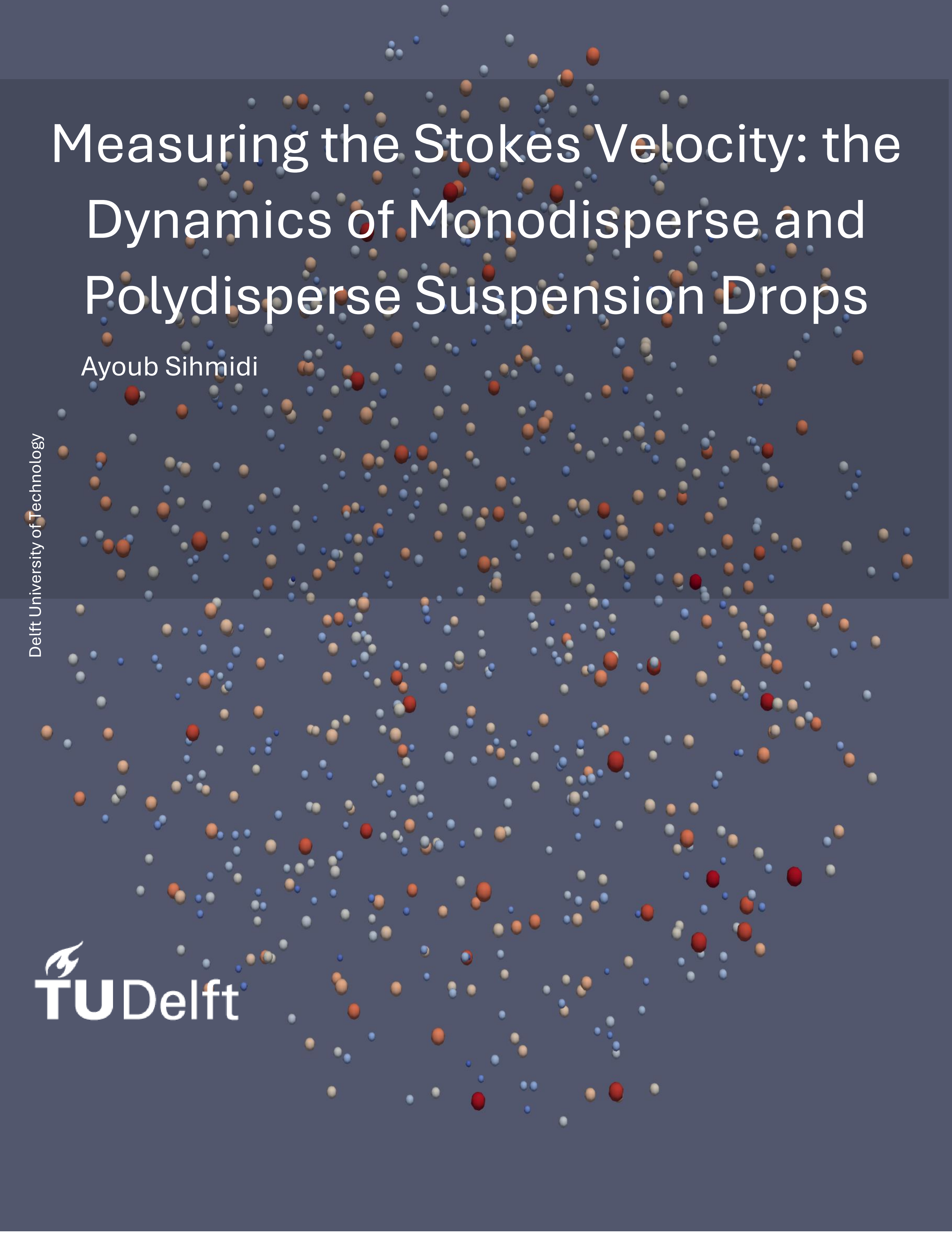

Measuring the Stokes Velocity: the Dynamics of Monodisperse and Polydisperse Suspension Drops

Ayoub Sihmidi

Delft University of Technology

TU Delft

DELFT UNIVERSITY OF TECHNOLOGY

ME-EFPT MASTER THESIS
ME55035

Measuring the Stokes Velocity: the Dynamics of Monodisperse and Polydisperse Suspension Drops

---

Authors:
Ayoub Sihmidi (4972589)

Supervisors:
Prof. dr. ir. Lorenzo Botto
ir. Heng Li

September 25, 2024

Delft
University of
Technology

Acknowledgments

First and foremost, I would like to praise God who has blessed me with innumerable favours and blessings and guided me to what I could not have done by myself. Secondly, I want to thank my parents, who raised me and invested a great deal into me and sacrificed many things for their children.

I then want to express my thanks to professor Prof. Dr. Ir. Lorenzo Botto for allowing me to conduct research in his group and giving me the opportunity to attain new knowledge and skills while doing so. He was always very accommodating, kind and provided useful and constructive feedback. Then I would like to thank my daily supervisor, ir. Heng Li, who gave me extensive support during and outside of the weekly meetings. In the beginning, he went to great lengths to explain to me the required theoretical and practical concepts and during the months that followed, he attentively followed my progress and provided feedback and steered me where necessary. I also want to thank Prof. Dr. Ir. Claire Chassagne and her research staff who kindly welcomed me at Deltares to have a look at their experimental setup and have lunch with them.

I also want to thank my wife for her patience, support and care during this project. I want to thank my sisters and brother for their support and always being there for me. And finally I want to thank my friends, extended family and teachers.

Abstract

In the last decade, interest in deep-sea mining (DSM) has surged. The expansion of the global economy, advancement of technologies and the transition to more renewable energy solutions have caused an increased demand for metals like lithium and cobalt and rare earth elements. With land resources diminishing, there is a growing interest in the vast deposits that the deep sea holds in enriched mineral deposits. To evaluate the effect of DSM operations on sea life, it is important to study the dynamics of resettling sediment plumes and their effect on the ocean environment. A convenient method to do that is by studying the settling of suspended sediment material in small-scale lab setups. When discharging a suspension drop into a water tank, settling velocities can be several times higher than normal (Stokes) settling velocities, leading to an error in the estimation of particle properties. To make these experiments more useful and effective, it is thus important to study for what conditions settling velocities of suspension drops are sufficiently close to the Stokes velocity.

We first studied monodisperse suspension drops, using a Stokesian Dynamics technique. Here, we theoretically predicted for which particle size, number of particles and volume fraction the suspension drop would reach the desired velocity. The unforeseen trend was that drops with higher volume fraction may be more desired because they decelerate more rapidly, due to the greater loss of particles and earlier break-up. There was qualitative agreement with the simulations. Moreover, because the velocity increases with the number of particles present in the drop, it is important to take into account the size of the drop. We also proposed a simple model for including the slower moving particles that trail the particle cloud and showed how the mean velocity of all particles in time gives a good estimate of the experimentally measured velocity. Based on the simulations, we predicted for which particle size a_{crit} a drop with given size and volume fraction decelerates to two times the Stokes velocity, within a certain distance. We also showed how the measured velocity distribution can indicate whether the measured settling velocity is close to the Stokes velocity or not.

We studied polydisperse clouds with a log-normal size distribution and varying standard deviations. The evolution of polydisperse clouds is very similar to that of monodisperse clouds. The biggest difference is that the leakage rate of particles increases with increasing polydispersity. The initial phase of particle leakage is also much more pronounced for polydisperse drops. Due to this, the velocity of the cloud drops faster, and the cloud breaks up earlier than its monodisperse equivalent. It was also found that smaller particles have a greater probability of leaving the cloud, this effect becoming significantly more pronounced at higher standard deviations. Due to this, small particles have on average longer time to decelerate and there is a size-dependent error for polydisperse drops. At extremely low volume fractions, polydispersity acts as an inhibitor to cloud formation and particles are seen to segregate based on size. Finally, we found no significant differences in behavior of polydisperse clouds with continuous size distributions compared to those with discrete size distributions.

Based on all the simulation data, we presented a set of formulas that can be used to estimate the (mean) particle size limit as a function of drop properties. A preliminary analysis showed how these expressions can be used to generate curves with which the volume fraction can be selected based on the size of the drop and the mean particle size. Thus, we have presented a verifiable approach to the optimization of the suspension drop settling experiment, that can be validated and used to study properties of settling suspended materials.

Contents

List of Tables

List of Figures

1 Background

In nature and everyday life, suspensions are abundant. Suspensions are encountered not only in nature (e.g. blood) but are also inherent to many industrial processes. Typical examples of suspensions encountered in industry are paint, ink, some food items, many cosmetic products and some pharmaceuticals (medicine is often ingested using water as the carrier). Moreover, industrial feeds in the process industry often contain impurities. Hence, the properties of a flowing suspension are of crucial interest to many fields and applications. Note that the definition of a suspension can also include aerosols (liquid or solid dispersed in a gas) and granular media (solid dispersed in a fluid which itself does not play a major role). In what follows, suspension shall only be used to refer to solid particles - of arbitrary shape, so this includes fibers among other encountered shapes - dispersed in a liquid. The particles contained in suspensions vary in size on the order of nanometers (these form colloidal suspensions) to micrometers and larger (non-colloidal). In the former type, the net gravitational force (gravity minus buoyancy) is on average balanced by forces caused by the impeding bombardment of solvent molecules with the suspended particles (so called Brownian forces). The result is that the particles remain in suspension. In non-colloidal suspensions, gravity dominates Brownian effects and thus sedimentation occurs, because the random movements are lesser in amplitude for larger particles.

The dynamics of suspensions have been a topic of investigation for more than a century. There is a great deal of theoretical and experimental work that give an understanding of some fundamental suspension phenomena. In particular the theory of flows where particle inertia is negligible compared to viscous forces (also called Stokes flow), is well developed. For example, there exist analytical solutions for the flow generated by a rigid spherical particle in an otherwise stationary fluid (also called disturbance flow). With this flow field, the fluid traction can be computed an integrated over the surface of the particle, giving the infamous formula for the Stokes drag. Because of the vanishing inertia of the particle, the net gravitational force has to be counteracted by the drag force, giving the fall speed of the sphere (the Stokes velocity). Building upon this solution, it is possible to approximate the solution for two falling spheres, leading to the interesting finding that two spheres fall at a greater speed than an isolated sphere. This trend does not persist, as it is yet another fundamental result that increasing the amount of suspended particles will lead to a reduction in fall speed compared to the Stokes velocity. This and more will be uncovered in greater detail in the next section.

It is interesting to note that merely the consideration of the hydrodynamic interactions between particles suspended in a viscous liquid can give rise to some very interesting and perhaps unexpected phenomena. One of those phenomena is that extremely small perturbations to initial conditions can result in major differences in the interaction behaviour (also called Chaotic dynamics). Hence the idea grows that by including the necessary but basic physics (gravity, hydrodynamic forces and in limited cases Brownian forces and lubrication forces), it is possible to study the behaviour of suspensions. And this is what has been done in many proceedings (see [1] for a comprehensive review). However, a lot of suspension phenomena are still not well understood or even fully uncovered. For example, most research has focused on monodisperse suspensions (all particles having equal size), even though the majority of suspensions have some degree of polydispersity (a distribution of particle sizes).

One such topic that has not yet received much attention is the behaviour of particle clouds suspended in a liquid. These clouds settle multiple times faster than the speed of an isolated particle due to hydrodynamic interactions between the particles. These clusters are encountered in many settings and may form due to several reasons. Moreover, this phenomenon is relevant to many applications. For example, in deep-sea mining (DSM) polymetallic nodules are harvested and the waste sediment is discharged back into the ocean (Fig. 1). The settling of this particle plume and influence of ocean currents is important for optimising this process as well as ecological considerations [2, 3, 4, 5, 6, 7, 8]. Understanding particle cloud behaviour is also essential for understanding certain geophysical flows [9, 10] and flows in porous media [11]. Finally, particle clouds are also relevant to certain health applications, like understanding the deposition of cigarette smokes in the lungs [12] and inventing novel mechanisms for drug delivery [13].

One of the reasons that many suspension related phenomena are only now being researched (apart from the sheer amount of them), is the rapid advancement of computing power and algorithms for numerical analysis and simulation of physical systems. Experimental equipment for fluid mechanics has also rapidly evolved (e.g. PIV, LIF). It remains that suspensions are quite difficult to analyze experimentally. The speed of the settling front (in sedimentation) can be determined experimentally, as well as the viscosity of the suspension using rheometry. However, it is nearly impossible to observe and measure the particle interactions that lead to this collective behaviour. Luckily, there exist several simulation methods that can be used in this domain of study, varying in their accuracy and speed (Section 2.5). This opens the door to the study of these collective phenomena and their understanding and is also a very valuable tool for researchers and engineers that wish to do quantitative studies.

In the next section, an overview will be presented of the most significant results in the area of suspension dynamics and numerical techniques for simulation of suspensions. This will set the stage for the topic of the current study. Then, recent important findings regarding this subject will be summarized. And finally, an outline of the research topics and questions will be given.

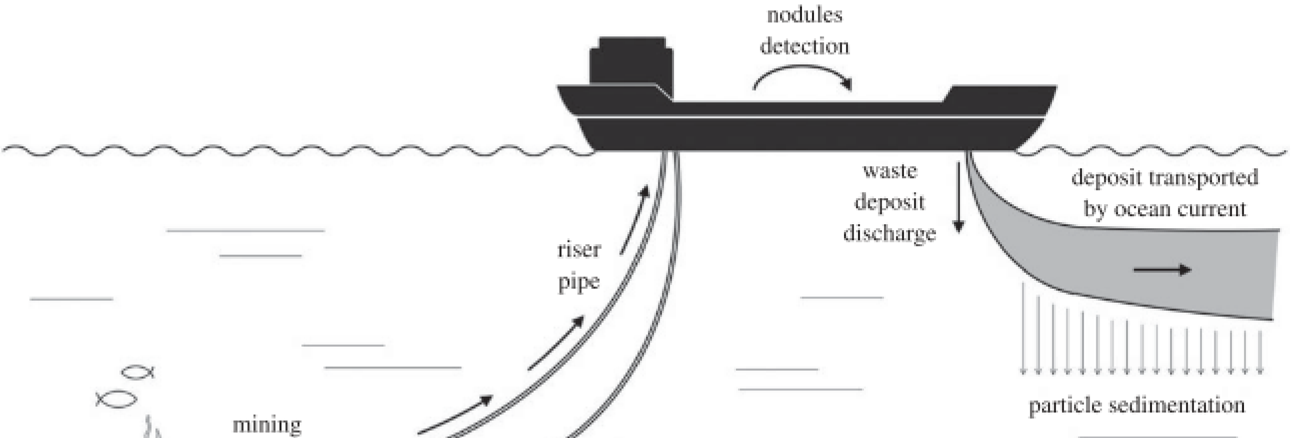

Figure 1: During deep-sea mining operations, polymetallic nodule rich sediment is mined from the ocean bed and thereafter discharged back into the ocean. Reproduced from [2].

2 Literature review

2.1 Stokes flow basics

To discuss the dynamics of a sedimenting suspension, we need consider both the fluid as well as the particle dynamics. The fluid dynamics are described by the well known Navier-Stokes (NS) equations. In the case of small enough particles, the characteristic length scale of the flow becomes small so that the velocity scale is also small. The Reynolds number, which characterizes the relative importance of inertial effects to viscous effects, is then very close to zero allowing us to neglect the convective acceleration terms in the Navier-Stokes equations. The Stokes number, which signifies the ratio between a characteristic fluid time scale and that for a particle, is also approximately zero for many settling suspensions due to the size of the particles. If both these conditions are met, the nonlinear Navier-Stokes equations can be simplified to the linear Stokes equations:

$$\begin{aligned} \nabla \cdot \mathbf{u} &= 0, \\ -\nabla p + \mu \nabla^2 \mathbf{u} &= 0. \end{aligned} \tag{1}$$

At many instances in studying *creeping flow* we make use of this linearity. It also follows from these equations that both the pressure and the vorticity are harmonic, meaning that information in the flow is (in theory) propagated at infinite speeds. One method often employed in studying fluid flow, is the linear decomposition of the velocity field. Assuming $\Delta\mathbf{x}$ sufficiently small, the velocity field $\mathbf{u}^\infty$ can be written as:

$$\begin{aligned} \mathbf{u}^\infty(\mathbf{x}) &= \mathbf{u}^\infty(\mathbf{x_0}) + \nabla\mathbf{u}^\infty(\mathbf{x_0}) \cdot (\mathbf{x} - \mathbf{x_0}) + \mathbf{h.o.t.} \\ &\approx \mathbf{U}^\infty + \boldsymbol{\Omega}^\infty \cdot \mathbf{x} + \mathbf{E}^\infty \cdot \mathbf{x}. \end{aligned} \tag{2}$$

Note that the velocity field $\mathbf{u}^\infty$ is referring to the ambient velocity field existing in the flow without the disturbance caused by the particle. That the second order tensor $\nabla\mathbf{u}$, containing all first order spacial derivatives of the velocity, can be decomposed into a symmetric and anti-symmetric portion. These are respectively the rate of strain tensor E_{ij} and the rate of rotation tensor Ω_{ij}. Keeping only the linear first order term, we can thus approximate the velocity field as the sum of a uniform translation, a straining part and a rotating part. Due to the linearity of Stokes flow, we can study the flow for a translating, rotating and straining particle or flow around a particle individually and add the flow fields to obtain the overall flow (the superposition principle) when all three elements are present. However, in the case of sedimentation we are largely interested in the solution for a single translating sphere.

First, because of linearity, both the velocity and the pressure should be linear in the driving force U^∞. The solution can be readily constructed by using the series [14] of spherical solid harmonics (the pressure is harmonic and goes to zero at infinity). To obtain the pressure (a scalar), U^∞ is dotted with the first order tensor harmonic (up to a multiplicative constant). The velocity (a vector also linear in U^∞) can be obtained by multiplying U^∞ with the zeroth- and second order tensor harmonics, next to a particular solution driven by the pressure gradient. Subsequently applying the boundary condition $\mathbf{u} = -\mathbf{U}^\infty$ at the surface of the sphere and the continuity equation, the flow field and pressure field can be obtained as:

$$\begin{aligned} \mathbf{u}(\mathbf{x}) &= -\frac{3a}{4}\mathbf{U}^{\infty}\left(\frac{\mathbf{I}}{r}+\frac{\mathbf{xx}}{r^3}\right)-\frac{3a^3}{4}\mathbf{U}^{\infty}\left(\frac{\mathbf{I}}{3r^3}+\frac{\mathbf{xx}}{r^5}\right), \\ p-p_{\infty} &= -\frac{3\mu a\mathbf{U}^{\infty}}{2}\frac{\mathbf{x}}{r^3}. \end{aligned} \tag{3}$$

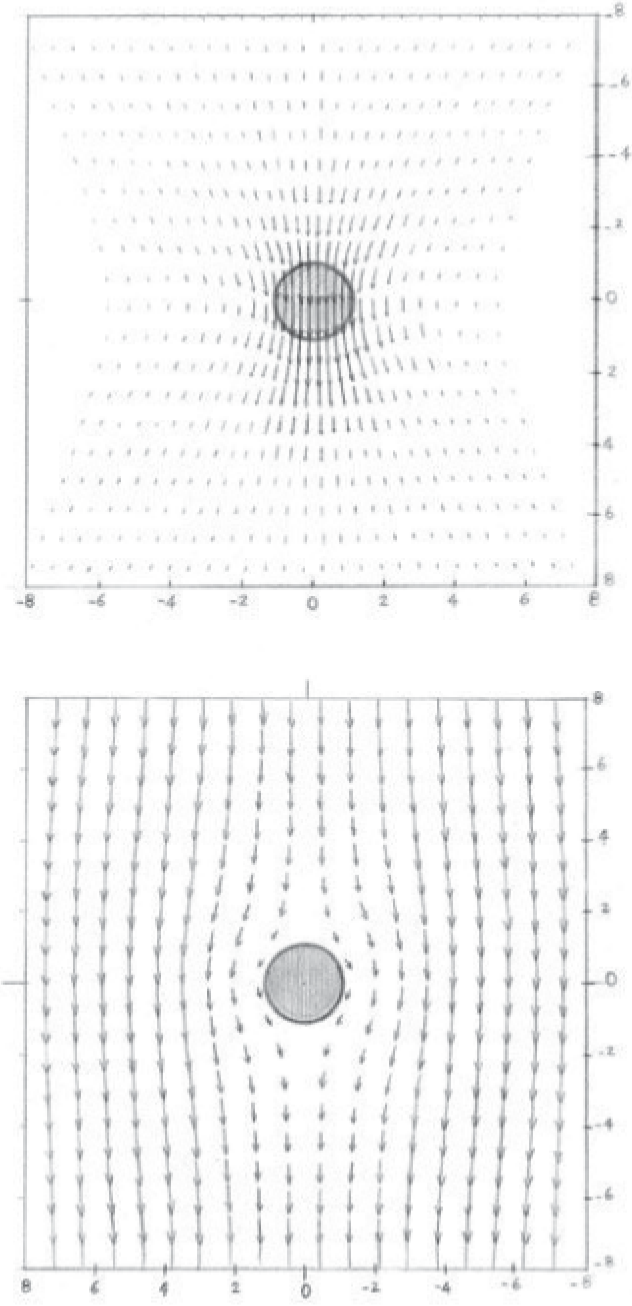

Figure 2: Disturbance flow streamlines for a translating sphere (top) and complete streamlines for a sphere fixed in a uniform stream (bottom). Reproduced from [1].

The streamlines for this type of flow are shown in Figure 2. The first image shows the (disturbance) flow generated by a translating sphere: the particle is displacing fluid for its downward motion and in its wake fluid is drawn in. The second image shows what the flow would look like if the sphere was fixed, and the fluid translates uniformly. Equation (3) tells us that the dominant fluid disturbance decays as r^{-1}. There is also a more rapidly decaying portion, as r^{-3}. This latter disturbance is associated with the finite size of the particle, whereas the former does not scale with the size, as will be explored later. Note that a disturbance in the fluid velocity that scales with r^{-1} decays rather slowly. As we will see, this is the main mechanism by which co-settling particles interact and will regularly be referred to as long-range hydrodynamic interactions.

Now that we have obtained the velocity field, the hydrodynamic force (drag) on the single settling particle can be obtained by summing the contributions of fluid surface traction:

$$\mathbf{F}_{\mathrm{h}} = \int_{S_{\mathrm{p}}} \boldsymbol{\sigma} \cdot \mathbf{n} \, dS. \tag{4}$$

Where, for a Newtonian fluid, the Cauchy stress tensor equals $\sigma_{ij} = -p\delta_{ij} + 2\mu E_{ij}$. Using equation (3), it is found that the traction vector is $\frac{3\mu}{2a}\mathbf{U}^{\infty}$ everywhere on the surface of the sphere. The integral in (4) is dramatically simplified as the product of the constant traction vector multiplied with the surface area of the sphere, which gives the *Stokes drag*:

$$\mathbf{F}_{\mathrm{h}} = 6\pi\mu a \mathbf{U}^{\infty}. \tag{5}$$

This is a fundamental result for sedimentation and tells us that the drag on a single particle scales linearly with the size of the particle a. If a particle settles in a fluid under the influence of gravity, it starts experiencing a hydrodynamic drag from the fluid. As the particle velocity increases, the drag increases according to equation (5) until the (net) gravity and drag are in equilibrium whereupon the particle reaches its terminal settling velocity. When the Stokes number is low, the stationary regime sets in almost instantaneously. Upon equating the Stokes drag and the net gravity force on the sphere $\mathbf{F_g} = \frac{4}{3}\pi a^3(\rho_p - \rho_f)\mathbf{g}$, we obtain the Stokes velocity:

$$\mathbf{U}_S = \frac{2}{9}\frac{a^2}{\mu}(\rho_p - \rho_f)\mathbf{g}. \tag{6}$$

2.2 Green's function and resistance functions

Now, we will build to yet another fundamental building block for studying the theory of sedimentation: the Stokeslet. Consider the velocity field in (3). As the particle is assumed to be in force equilibrium, it is useful to express the velocity field in terms of the driving external force $\mathbf{F_e}$. This could be gravity, an external electric field and so on. This external force will be equal to the drag force. Using $\mathbf{F}_{\mathrm{e}} = -\mathbf{F}_{\mathrm{h}} = 6\pi\mu a\mathbf{U}$, we rewrite the velocity field as:

$$\mathbf{u}(\mathbf{x}) = \left(\frac{\mathbf{I}}{r} + \frac{\mathbf{xx}}{r^3}\right) \cdot \frac{\mathbf{F}_{\mathrm{e}}}{8\pi\mu} + \left(\frac{\mathbf{I}}{3r^3} - \frac{\mathbf{xx}}{r^5}\right) \cdot \frac{a^2\mathbf{F}_{\mathrm{e}}}{8\pi\mu}. \tag{7}$$

If we keep the external force constant and let the particle radius a go to zero, the last term in this equation goes to zero. Hence, this fluid velocity disturbance is associated with the size of the particle. Conversely, there is a disturbance that only depends on the external force is independent of the particle radius (hence 'point force'):

$$\mathbf{u_{PF}} = \left(\frac{\mathbf{I}}{r} + \frac{\mathbf{xx}}{r^3}\right) \cdot \frac{\mathbf{F}_\mathrm{e}}{8\pi\mu} = \mathcal{G} \cdot \frac{\mathbf{F}_\mathrm{e}}{8\pi\mu}. \tag{8}$$

Here, $\mathcal{G}$ is also coined the Oseen-Burgers tensor and it is the Green's function for the Stokes equations [1]. Something extremely useful regarding this, is that we can use the Green's function (which tells us the velocity disturbance due to *one* point force) to compute the velocity field due to a distribution of point forces located on the outer surface of an arbitrary particle. After all, what causes the disturbance in the fluid is the traction at the particle surface. This may be written as:

$$\mathbf{u}(\mathbf{x}) = \sum_{i=1}^{N} \frac{\mathcal{G}(\mathbf{x} - \mathbf{x_i})}{8\pi\mu} \cdot \mathbf{F}_\mathrm{i}. \tag{9}$$

Where $\mathbf{F}_\mathrm{i}$ is the point force applied at position $\mathbf{x}_\mathrm{i}$. The logical extension is then to generalize this sum to an integral of point forces distributed over the surface. The resulting formula is:

$$\mathbf{u}(\mathbf{x}) = \int_{S_p} \frac{\mathcal{G}(\mathbf{x} - \mathbf{y})}{8\pi\mu} \cdot (\boldsymbol{\sigma} \cdot \mathbf{n})(\mathbf{y}) \, dA(\mathbf{y}). \tag{10}$$

The final central concept is that of resistance functions. Often, interest lies in the motion of particles and its evolution. Notice in equation (4) that the drag force is linear in the stress tensor σ. The stress tensor (for a Newtonian fluid) is itself linear in the fluid velocity field $\mathbf{u}$. Finally, the velocity field in a particulate flow in the Stokes regime will be linear in the forcing $\mathbf{U}$. Therefore, the hydrodynamic drag $\mathbf{F}_h$ is also linear in $\mathbf{U}$. This leads us to write:

$$\mathbf{F}_h = -\mathbf{R_{FU}} \cdot \mathbf{U}. \tag{11}$$

The second order tensor $\mathbf{R_{FU}}$ relates the particle velocity to the force. It can be shown that this tensor is proportional to μL, an unsurprising scaling. Often these relations are non-dimensionalized, to remove the effect of particle size. Moreover, this tensor is anisotropic for an arbitrary shaped particle but can show isotropy in several or all directions if the particle has one or more planes of symmetry. Using the formula for the Stokes drag (5), we can write for a spherical particle:

$$\mathbf{R_{FU}} = \mu a \begin{pmatrix} 6\pi & . & . \\ . & 6\pi & . \\ . & . & 6\pi \end{pmatrix}.$$

Moreover, it can be shown that the resistance tensor is always symmetric, and all its eigenvalues (in diagonalized form) are positive, dimensionless (it was already determined that $\mathbf{R}$ scales with variables μ and L) numbers determined by the particle shape. Finally, often the desire is to compute the particle motion from the forces, which is essentially the inverse problem of (11). In that case, we use $\mathcal{M} = \mathcal{R}^{-1}$.

2.3 Advanced solutions

We have explored the solution to the Stokes equation for translation. The velocity and pressure fields for a sphere fixed in a rotating flow and straining flow can be derived in a likewise manner. They are given in Chapter 2 of the work by Guazzelli & Morris [1]. Moreover, similarly to the linear relation we could write between the forcing $\mathbf{U}$ and the hydrodynamic force $\mathbf{F}^{\mathrm{h}}$, a rotating flow (described by the rate of rotation ω_i) will induce a hydrodynamic torque $\mathbf{T}^{\mathrm{h}}$ and their relation can be described by a second order tensor $\mathbf{R}^{\mathrm{T}\omega}$. The torque is a very known concept in mechanics, being related to the change in angular momentum. A straining flow described by the rate of strain tensor $\mathbf{E}^{\infty}$ induces what is called a stresslet (also a second order tensor S_{ij}) and their relation is captured in $\mathbf{R}^{\mathrm{SE}}$. The stresslet reflects the added stress due to the rigid particle's resistance to straining motion. It is not needed for describing the motion of the particles (like the force and torque), but is important for determining the bulk stress. Finally, there can also exist cross-couplings, for example, between the force and the rate of strain, or the torque and the velocity. Putting everything together, we get

$$\begin{pmatrix} \mathbf{F}_{\mathrm{h}} \\ \mathbf{T}_{\mathrm{h}} \\ \mathbf{S}_{\mathrm{h}} \end{pmatrix} = - \begin{pmatrix} \mathbf{R}_{\mathrm{FU}} & \mathbf{R}_{\mathrm{F}\omega} & \mathbf{R}_{\mathrm{FE}} \\ \mathbf{R}_{\mathrm{TU}} & \mathbf{R}_{\mathrm{T}\omega} & \mathbf{R}_{\mathrm{TE}} \\ \mathbf{R}_{\mathrm{SU}} & \mathbf{R}_{\mathrm{S}\omega} & \mathbf{R}_{\mathrm{SE}} \end{pmatrix} \cdot \begin{pmatrix} \mathbf{U} - \mathbf{U}^{\infty} \\ \boldsymbol{\omega} - \boldsymbol{\omega}^{\infty} \\ -\mathbf{E}^{\infty} \end{pmatrix}. \tag{12}$$

Note that this can also be written in the mobility formulation, to calculate the (angular) velocities and rate of strain from the hydrodynamic force, torque and stresslet. This is more common, especially in cases when particle inertia is negligible as in this case the hydrodynamic force/torque is equal to the external force. Note that $\mathbf{U}^{\infty}$, ω^{∞} and $\mathbf{E}^{\infty}$ are the ambient fluid velocity, rate of rotation and rate of strain, respectively. $\mathbf{U}$ and ω are the particle (angular) velocities.

If the ambient flow can not be fully represented with a linearly varying flow field, an additional term appears in the equation relating the velocities of particle and fluid to the force and torque. The equations including these terms are called Faxén laws (see Chapter 3 in [15]):

$$\begin{aligned} \mathbf{F} &= 6\pi\mu a \left[\left(1 + \frac{a^2}{6}\nabla^2 \right) \mathbf{U}^{\infty} - \mathbf{U} \right] \\ \mathbf{T} &= 8\pi\mu a^3 \left[\boldsymbol{\omega}^{\infty} - \boldsymbol{\omega} \right] \\ \mathbf{S} &= \frac{20}{3}\pi\mu a^3 \left(1 + \frac{a^2}{10}\nabla^2 \right) \mathbf{E}^{\infty}. \end{aligned} \tag{13}$$

Here, the fluid variables are evaluated at the center of the particle. Finally, one more concept that will be useful is the multipole expansion. Originally a concept from electrostatics, the idea is to expand the term $\mathcal{G}_{ij}(\mathbf{x} - \mathbf{y})$ in equation (10), giving

$$u_i(\mathbf{x}) = -\frac{F_j^{\mathrm{h}}}{8\pi\mu}\mathcal{G}_{ij}(\mathbf{x}) + \frac{M_{jk}}{8\pi\mu}\frac{\partial \mathcal{G}_{ij}}{\partial x_k}(\mathbf{x}) + \cdots, \tag{14}$$

where the integrals in the original equation can now be written as the force F^{h} and moments M_{jk} (containing the torque and stresslet) because the y-dependence in $\mathcal{G}$ was removed. These two terms are respectively the force monopole and dipole and other multipoles (quadrupole, octupole) follow from the higher order terms. We see again the importance of the Green's function, as it is this function and its derivatives that shape the solution.

2.4 Multiparticle dynamics

2.4.1 Pair of particles

Up until now we have only considered the single particle settling behaviour. When two particles settle together, we may expect them to behave as individually settling particles if the separation is extremely large. If this is not the case, the particles will interact hydrodynamically. The flow generated by the settling of one particle will influence the second particle's motion and vice versa. One way to systematically study these effects, is with the method of reflections (see Chapter 6 in [15]). We first assume that both particles move at the velocity following from Stokes' law. The fluid velocity disturbance induced by the settling of particle 1 is equal to the Stokeslet. This flow will cause an additional velocity of particle 2, which is approximately equal to the dominant term in equation (3), with $\mathbf{x} = \mathbf{r}$. The procedure is identical for the addition to the velocity of particle 1 causes by the motion of particle 2. We can superimpose this interaction effect onto the single particle settling velocities. The result for this first reflection is:

$$\begin{pmatrix} \mathbf{U}_1 \\ \mathbf{U}_2 \end{pmatrix} = \begin{pmatrix} \frac{\mathbf{I}}{6\pi\mu a_1} & \frac{1}{8\pi\mu}\left(\frac{\mathbf{I}}{r} + \frac{\mathbf{rr}}{r^3}\right) \\ \frac{1}{8\pi\mu}\left(\frac{\mathbf{I}}{r} + \frac{\mathbf{rr}}{r^3}\right) & \frac{\mathbf{I}}{6\pi\mu a_2} \end{pmatrix} \cdot \begin{pmatrix} \mathbf{F}_1^e \\ \mathbf{F}_2^e \end{pmatrix}. \tag{15}$$

These interactions keep getting reflected, and using computers it is possible to calculate through many of these reflections to achieve an accurate result. Note that the tensor relating external forces to particle velocities in equation (15) is the mobility tensor $\mathcal{M}$. Moreover, because the particles interact through the intermediate fluid we see that the force acting on particle 1 affects particle 2. One very interesting result is that the resulting particle velocities are greater than the single particle settling velocities. In other words, two particles settle faster than one. The flow generated by each particle drags the other particle along in the direction of the flow. Also, because of the additional term containing the dyad **rr**, there are now components of the velocity in the directions not aligned with gravity (i.e. there is sideways motion). Finally, for two particles of equal size and exposed to an equal external force, all velocity components will be equal. Thus, the particles maintain equal spacing.

When the particle spacing is on the order of the particle radius, many reflections are needed to achieve an accurate result. In this case, results from lubrication theory (Chapter 9 of [15]) can be used to speed up the calculations. When two particles move towards other at close proximity, the interstitial fluid needs to be pumped out. This requires large pressures, which is accompanied by large forces (conversely, movement in the opposite direction creates suction). In fact, the lubrication force diverges as the particles move closer together. This leads to a remarkable damping of the relative motion. Keeping up with the resistance formulation, we can include lubrication interactions as

$$\begin{pmatrix} \mathbf{F}_1^l \\ \mathbf{F}_2^l \end{pmatrix} = -\mathcal{R}^l \cdot \begin{pmatrix} \mathbf{U}_1 \\ \mathbf{U}_2 \end{pmatrix}. \tag{16}$$

It is a recurring theme in the current discussion that a distinction is made between long range interactions and short range interactions. The former can be best described in the mobility formulation, using the method of reflections, and the latter is best handled using lubrication theory. This concept is exploited by some simulation techniques, like Stokesian Dynamics [16].

A particle pair of unequal size shows contrasting behaviour. Because the settling velocity of a particle scales with its size, the particles will move relative to each other. This relative moment renders this case much more dynamic, as the particle interactions will be dominated alternatively by long range and short range interactions. The motion of a triplet also provides some insight. The middle particle will always settle faster, due to it experiencing the flow generated by both particles. It is also found that velocities will be twice as large when the particles are aligned in the direction of the flow (vertical for sedimentation) compared to when the particles are aligned in the direction perpendicular thereto (horizontally). This is because the disturbance flow (see Fig.2) for the settling sphere is twice as large in the vertical direction, compared to the horizontal direction. The time evolution of a triplet (as well as the dissimilar doublet) can be computed using numerical techniques, showing features of chaotic dynamics.

2.4.2 Hindered settling

We move from the study of single particles to a collection of settling particles. While the trend up until now was that particles settle faster collectively, this is not actually the case for a suspension. This is due to the fact that the settling particles create a back-flow of fluid, drastically increasing the drag, in proportion to the amount of particles present. This is called *hindered settling*. As a result, the particle settling velocity is actually lower than the Stokes velocity. The function that describes the ratio between the Stokes velocity and the (averaged) particle settling velocity is called the hindered settling function:

$$\langle \mathbf{u} \rangle_{\mathrm{p}} = \mathbf{U}_{\mathrm{S}} f(\phi). \tag{17}$$

The ratio between the particle averaged velocity and the theoretical Stokes velocity depends on the solid fraction ϕ. The precise functional correlation is a topic of long debate. The formula

$$f(\phi) = \frac{(1-\phi)^2}{(1+\phi^{1/3})\exp(5\phi/3(1-\phi))} \tag{18}$$

gives the best fit to all experimental data [17]. The correlation with the most widespread use is that derived from experiments by Richardson and Zaki [18]:

$$f(\phi) = (1-\phi)^5. \tag{19}$$

For very small ϕ, equation (19) has a linear form with slope 5 and equation (18) has the form of a power law with exponent 1/3. It is interesting to note that the form of these equations relates to the details of the assumed microstructure of the suspension [19]. First, using the method of reflections, the correction to the Stokes velocity due to particle interaction is found to be O(a/r), where r is the distance between the particles and a the size of the particle. If the particle arrangement is random, the probability of there being a second particle within a distance O(r) to interact with is O(ϕ). This leads to the linear correction to the Stokes velocity. If there is a periodic arrangement, the correction would be proportional to the average separation O($a\phi^{-1/3}$), leading to the power law correction. And indeed, it has been shown that suspensions that are dominated by Brownian motion (where it is more likely that particles are arranged randomly) settle according to the linear hindered settling function, at least in the dilute regime [20]. Little is known about the microstructure in suspensions that leads to the observed deviation from this behavior, as the microstructure depends on the hydrodynamics which itself depends on the microstructure, leading to complex interactions.

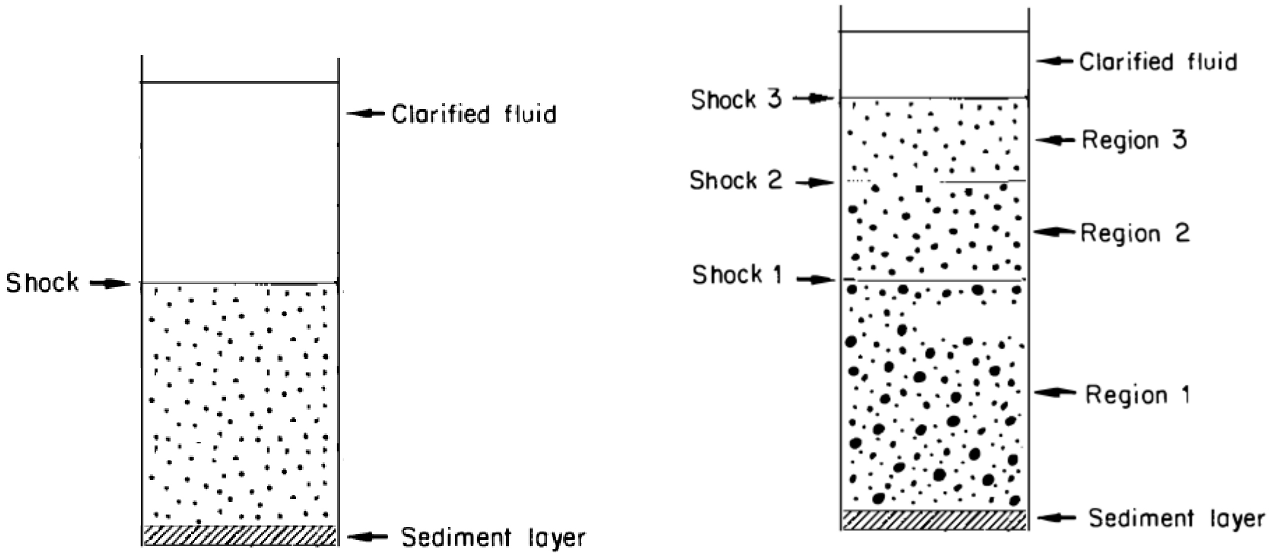

(a) Monodisperse suspension (b) Tridisperse suspension

Figure 3: Schematic showing the different regions formed in a suspension with varying degrees of polydispersity. Reproduced and modified from [19].

In a settling monodisperse suspension, three regions are formed (Fig. 3a). The bottom region is filled with sediment, the middle region consists of a dispersion at the original concentration, and a top region with clear fluid is formed. At the interface of the regions occupied by clear fluid and bulk suspension, a sharp shock is observed. Using a simple advection equation to express the conservation of particles and combining that with the hindered settling function, a self-sharpening mechanism is uncovered [21]. Moreover, it can be shown that the velocity of this front is equal to the hindered settling speed of the particles. This has led to the method by which settling velocities are measured in experiments (by measuring the front velocity).

2.4.3 Polydispersity

When the suspension contains species of different sizes, both qualitative and quantitative differences can be observed. After some time, several regions form in the settling suspension. Just like in the previous case, a sediment layer and a layer with clear fluid at the top can be seen. In between, the number of distinct regions that form is equal to the number of particle species. The layer above the sediment contains all species, and each layer above it is missing the fastest settling species in the region below it (Fig. 3b). Similarly to the monodisperse case, shocks can be observed between these regions. However, if the particle size distribution is continuous (i.e. all particle sizes are present within a certain range), there are no shocks but rather a continuous concentration gradient along the height of the vessel for each species [19]. As for the determination of the hindered settling function for the polydisperse case, there remains work to be done. Several attempts have been made, of which many are modifications to the monodisperse correlations. The approach that gives the best agreement is by using the local solid fraction in equation (19) as well as to calculate the Stokes velocity (6) of a species i by replacing the fluid density with the density of the suspension, excluding species i [19].

2.4.4 Particle clouds

A very interesting phenomenon in sedimentation is the settling of particle clouds or clusters. A particle cloud is a cluster of particles surrounded by clear fluid around its exterior, and also dragging fluid within its interior, the amount of which is dependent on the solid volume fraction. Perhaps surprisingly, the cloud can maintain its shape as well as the separation with the clear fluid outside it for a considerable time. Moreover, the cloud falls with a velocity greater than the Stokes velocity for individual particles. This is because of hydrodynamic interactions between the particles, similar to what was discussed for particle pairs. The fundamental difference is that the back flow of fluid is not hindering the motion of particles anywhere as much, seeing that the particles move as a cluster and only experience drag from the outside fluid.

The physics of a falling particle cloud can be compared to that of a fluid drop with a viscosity $\lambda\mu$ settling in a fluid with viscosity λ with velocity U. This system has been solved by Hadamard [22] and Rybcynski [23] and is also referred to as the HR solution. The drag on the drop is:

$$\mathbf{F} = -4\pi\mu a\mathbf{U}\left(\frac{1+3\lambda/2}{1+\lambda}\right). \tag{20}$$

Using this result for a spherical cloud of N particles with radius R (particles having radius a and density ρ_p), we find

$$\mathbf{U}_{\text{cloud}} = \frac{N\frac{4}{3}\pi a^3\left(\rho_p-\rho\right)\mathbf{g}}{2\pi\mu\frac{2+3\lambda}{\lambda+1}R} = N\frac{6a}{2\left(\frac{2+3\lambda}{\lambda+1}\right)R}\mathbf{U}_{\text{S}} \tag{21}$$

by balancing the net weight (gravity minus buoyancy) with the drag and substituting the Stokes velocity (6). Both in the particle cloud settling in clear fluid and the drop of heavy fluid settling in lighter fluid, a toroidal circulation is observed (Fig. 4b). Due to the particles interacting hydrodynamically (the amount of interactions depending on the number of particles), particles may exit the closed region of circulation and subsequently be carried away from the cloud with the outside fluid (Fig. 4). This leads to the appearance of a distinctive tail of particles. For stable clouds (typically those with less particles), this leakage of particles persists until it disintegrates. Clouds containing a large number of particles become unstable. First, these clouds evolve into a torus owing to the leakage of particles along the centerline of the cloud. The torus then breaks up into several droplets, and this process continues as a cascade. This intricate sequence of events can be reproduced in simulations by modeling particles as point forces according to equation (8), showing how (long-range) hydrodynamic interactions between individual particles on the microscale can produce collective behaviour and complex phenomena on larger scales. After discussing simulation techniques for suspensions, we will discuss particle clouds more in detail as well as recent advances on the topic.

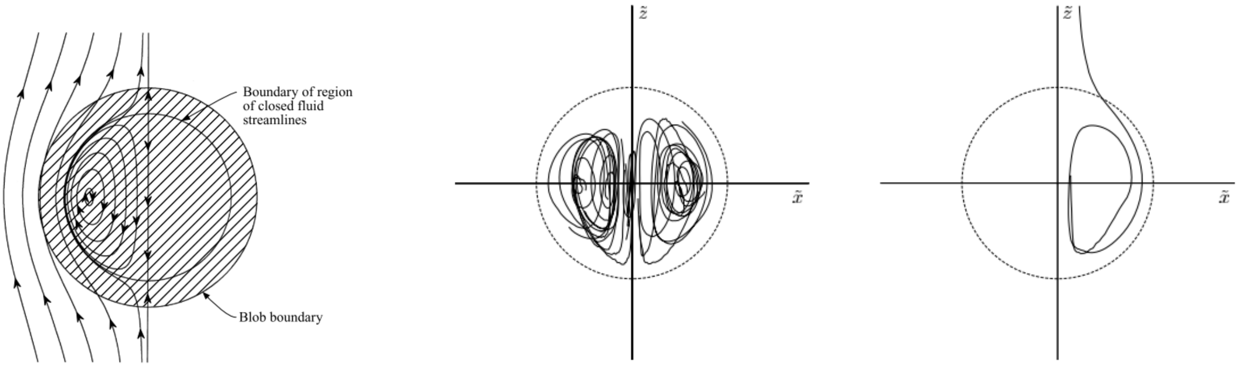

(a) (b) (c)

Figure 4: (a) Fluid streamlines in a reference frame moving downwards at the speed of the cloud. There is a spherical region inside the cloud where fluid streamlines do not leave the particle cloud. Reproduced from [24]. (b) Particle pathlines in a cloud showing the typical toroidal circulation. Reproduced from [25]. (c) One instance of a particle pathline showing the trajectory of a particle that leaks from the cloud. Reproduced from [25]. $\tilde{x}$ and $\tilde{z}$ are relative to the cloud center of mass.

2.5 Numerical techniques

2.5.1 Techniques for particle-laden flows

The dynamics of particle flows are governed by the Navier-Stokes equations for the fluid phase, and the Newton-Euler equations for the (rigid) particle phase. When we combine computational fluid dynamics methods (CFD) to solve the fluid phase with discrete element methods (DEM) to solve the particle phase, this is called CFD-DEM. The force balance for the particles include a particle-particle contact force, the hydrodynamic force (exerted by the surrounding fluid) and body forces. For the fluid, the incompressible volume averaged NS equations are used. A coupling routine is used to exchange the required information between the CFD and DEM solvers. There can be many variations in specific implementations for the fluid and particle phase models. A more fundamental difference however, is that between the resolved and unresolved method. When particles are smaller than the cell size, the flow around a particle is unresolved. When particles are large compared to the cell size, regridding of the mesh used for the CFD is necessary to resolve the flow but computationally very costly. Fictitious domain methods circumvent this problem by creating a mesh for the fluid volume as well as the particle volume. An extra body force is added so that the fictitious fluid inside the particle volume behaves as a rigid body, at the speed specified by the DEM solver. In reality it is more complicated and there exist several implementations, a popular one being the Immersed Boundary Bethod (IBM). For a popular implementation of CFD-DEM that is open source, see [26]. Finally, the Latticed Boltzman Method (LBM) is based on kinetic theory and can be used to resolve the flow surrounding particles without use of fictitious fluid regions [27].

When the Stokes number (the ratio between the particle response time and a typical time scale for the fluid) is low, the effect particles have on the flow can be captured by simpler methods. These methods include the dusty gas approach, Eulerian approach and the Lagrangian point-particle approach [28], differing mainly in the range of Stokes numbers they are valid in. A method that has been developed explicitly for the purpose of these types of flows, is Stokesian

Dynamics (SD). This method is akin to molecular dynamics, but for the simulation of particles in a viscous liquid. The focus in this method is not on detailed simulations of the flow, but on the motion of particles, due to both hydrodynamic and nonhydronamic interactions. The method has been shown to be accurate in both the qualitative and quantitative sense [16]. One of its advantages is its relatively fast computation times, compared to other methods used for similar purposes. It can be applied among other things for studying sedimentation, diffusion, flocculation, flow in porous media and polymer rheology. Essentially, by simulating the micro hydrodynamics we gain access to the behaviour of the particles as well as the macroscopic fluid properties that can be derived from that. We will now briefly discuss the details of this method.

2.5.2 Stokesian Dynamics

Stokesian Dynamics makes use of the pair hydrodynamic interactions discussed before to simulate the many-body problem. This includes both close range (lubrication) interactions, as well as long range interactions. The latter are best represented in the mobility formulation (15) whereas the lubrication interactions are best dealt with in the resistance formulation (16). The particles obey Newton's second law of motion; which for this case is called the Langevin equation:

$$m\frac{d\mathbf{U}}{dt} = \mathbf{F}_{\mathrm{h}} + \mathbf{F}_{\mathrm{e}} + \mathbf{F}_{\mathrm{b}}. \tag{22}$$

Here, $\mathbf{F}_{\mathrm{h}}$ is the hydrodynamic force, $\mathbf{F}_{\mathrm{e}}$ may include both external forces (like gravity) and interparticle forces and $\mathbf{F}_{\mathrm{b}}$ is the (random) Brownian force that may be neglected if particles are sufficiently large. Moreover, if flow is in the Stokes regime, the inertial term may also be neglected leading to $\mathbf{F}_{\mathrm{h}} + \mathbf{F}_{\mathrm{e}} = 0$. The main effort is then in calculating the hydrodynamic force, which is equal to

$$\mathbf{F}_{\mathrm{h}} = -\mathbf{R}_{\mathrm{FU}} \cdot (\mathbf{U} - \mathbf{U}^{\infty}) + \mathbf{R}_{\mathrm{FE}} : \mathbf{E}^{\infty}, \tag{23}$$

where we have used the resistance tensors to describe the linear coupling between kinematic variables and the hydrodynamic force.. For Stokes flow conditions, the particle velocities can be computed from this equation with

$$\mathbf{U} = \mathbf{U}^{\infty} + (\mathbf{R}_{\mathrm{FU}})^{-1} \cdot (\mathbf{F}_{\mathrm{e}} + \mathbf{R}_{\mathrm{FE}} : \mathbf{E}^{\infty}), \tag{24}$$

after which the particle positions are updated using $\Delta\mathbf{x} = \mathbf{U}\Delta t$ (these equations are usually non-dimensionalized first). As mentioned earlier, the resistance functions $\mathbf{R}_{\mathrm{FU}}$ and $\mathbf{R}_{\mathrm{FE}}$ are part of the grand resistance matrix $\mathscr{R}$ (12). For two spheres, the grand mobility matrix ($\mathscr{M} = \mathscr{R}^{-1}$) is known. The grand mobility matrix is formed using the Faxén laws (13) and the multipole expansion (14). The procedure is explained in more detail by Abade and Cunha [25]. We call this $\mathcal{M}^{\infty}$ and for large r, this is a good approximation. However, for small particle separations lubrication effects will be dominant. We can add these to our formulation, by making use of the fact that these interactions are close range, i.e. we need only add them for particle neighbours that are sufficiently close. Thus we can use the precise resistance interactions for two spheres $\mathscr{R}_{2S}$, which will include lubrication as well as the long range type interactions. We subtract the latter terms by inverting a two sphere mobility matrix which is truncated to only include far-field terms (15), so as not to count these terms twice. The final equation for $\mathscr{R}$ becomes:

$$\mathscr{R} = (\mathscr{M}^{\infty})^{-1} + \mathscr{R}_{2S} - \mathscr{R}_{2S}^{\infty}. \tag{25}$$

That concludes our discussion on SD for now; the details around the implementation used in this research will be shared in later sections. This was definitely not an exhaustive list of simulation methods for particulate flows. The reader is referred to Maxey [29] who provides a more comprehensive review. Brady [16] explains the Stokesian Dynamics method in more detail, validates it against experimental data of suspensions and provides some applications of the method.

2.6 Research on particle clusters

2.6.1 Monodisperse clouds

We will now proceed with our discussion on clouds of particles. It is worth noting that clouds of fibers show similar behaviour to clouds of particles and are relevant to several applications. For research on sedimenting clouds of fibers, see [30, 31, 32, 33]. An early and significant piece of research on particle clouds is that by Nitsche and Batchelor [24]. In this study, they performed simulations of particle clouds (referred to as 'blobs') in the dilute regime ($\phi < 4\%$) with a maximum number of 320 particles. Both fluid and particle inertia were neglected. Particles were assumed to interact hydro dynamically only by the effect of the generated disturbance flows (Stokeslets). First, the blob was observed to remain a cohesive entity (without manual imposition of a boundary). Also, particle leakage and the subsequent appearance of a 'tail'was observed. In addition to setting light on the mechanism leading to this, a formula based on a scaling analysis was proposed for the rate of particle leakage as $-\frac{\mathrm{d}N_b}{\mathrm{d}t} = K\frac{V_b}{d}$. The argument is that if particle leakage is associated with random velocity fluctuations, it should scale with the velocity of the blob V_b and with the inverse of the mean particle spacing $d = (4\pi/3N_b)^{1/3}\,R$. Based on the H-R solution (21) and the analogy with falling drops of liquid, the velocity of the blob can be approximated as $V_b \approx u_o(\frac{6}{5}N_b\frac{a}{R} + 1)$, which gives an explicit formula for the rate of particle leakage $-\mathrm{d}N_b/\mathrm{d}t \approx$ const. u_0R^2a/d^4, showing that it is proportional to the surface area of the blob. Note that a and R are the particle and cloud radius, respectively, and u_0 is the single particle Stokes velocity.

Another benchmark study is that by Metzger et al. [34]. Both simulations as well as experiments were performed. The simulations used a point particle approach, similar to that of Nitsche and Batchelor, the difference being that the latter authors also included an artificial close-range repulsive force to prevent particle overlap. Instead, Metzger et al. just eliminated simulation runs where interparticle distances (and with that sedimentation velocities) became unrealistic. Experiments were performed with glass beads in silicon oil for solid fractions up to 20 % and particle numbers up to a few thousand (the uncertainty rising from the method of approximation). The typical formation into a torus and subsequent break-up was produced in the experiments as well as in the simulations (Fig. 5). Statistics (mostly of the numerical simulations) are given for the probability of cloud destabilization, as a function of the initial number of particles N_0. For $\mathrm{N}_0 > 1000$, break-up always occurs. For a lesser amount of particles, destabilization probability increases with N_0. However, the time until destabilization t_b^* (dimensionless time) is also positively correlated with N_0. Data of the cloud radius R^* and velocity V^* during torus formation show large variation but qualitative agreement between experiments and simulations, except for higher solid fractions (where the point-force assumption loses its validity). The data suggests that $R^*(t^*) - 1 \sim N_0^{-2/3}t^*$, i.e. cloud radius increases linearly in time. The data also shows that the decrease in cloud velocity is due to leakage of particles (decrease in cloud density leads to decreased fall velocity) as well as the effect of the emerging shape (a torus experiences more drag than a sphere). There is also good agreement between experimental and numerical results for the amount of particle leakage. It is shown that particle leakage decreases with increasing N_0. Moreover, Metzger et al. also adds strength

Figure 5: Images of a falling particle cloud, reproduced from [34]. Left: simulation using point-particles. Right: experiment using glass beads in silicon oil.

to the hypothesis of Nitsche and Batchelor on the cause of particle leakage, by showing that samples with greater particle leakage deviate more from the streamlines of the closed toroidal circulation. The flow and pressure fields are visualized at key time instances (Fig. 6). After the torus forms, it expands leading to decreased pressure at the leading front whereupon the incident fluid streamlines can enter the cloud, causing break-up and creating new circulation regions. Finally, a physical argument is given for the onset of destabilization. At a certain torus aspect ratio, the vertical velocity at the centre generated by the particles inside (approximated as randomly distributed point particles) is less than the fall velocity, at which point streamlines from the outside fluid penetrate the torus.

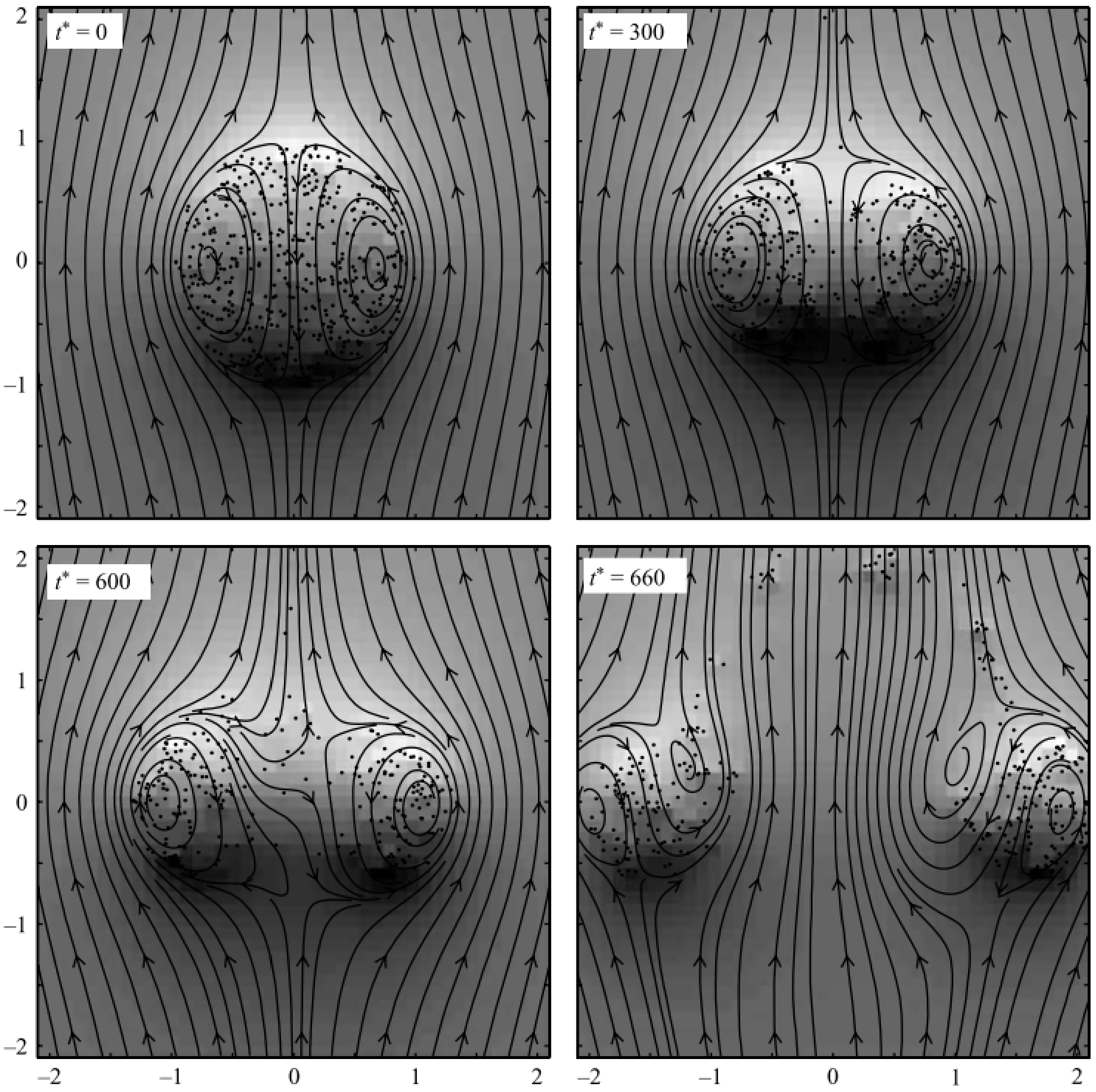

Figure 6: Flow and pressure fields in a reference frame moving downwards at the speed of the cloud. High pressure is indicated in dark. Reproduced from [34].

It can be shown that when the ratio of the distance to the particle radius $r/a = O(Re^{-1})$, inertial effects cannot be neglected. Thus, when $r/a \ll Re^{-1}$, inertial effects can be neglected but farther from the sphere they become comparable to viscous effects. In this case, the Stokes approximation is not valid anymore. Oseen [35] constructed a solution (the 'Oseenlet') that is valid in these finite Re conditions (Fig. 7). As can be seen, the fore-aft symmetry we know from the Stokeslet is broken (as well as the associated irreversibility). Close to the particle, the flow field closely resembles the Stokeslet, but resembles the flow field of a potential point source farther away. A wake is also formed, where fluid inflow compensates the outflow from the source. This leads to interesting behaviour of a pair of spheres, where they approach eachother due to decreased drag on the trailing sphere, then touch, then tumble (Drafting-Kissing-Tumbling or DKT). Subramiam and Koch [36] investigated the behaviour of particle clouds at these finite Re conditions. They found that these clouds expand outwards due to the radial outflow associated with the source term in the Oseenlet. For large concentrations, the clouds first flatten due to wake interactions (drafting) and then expand outwards in the horizontal direction.

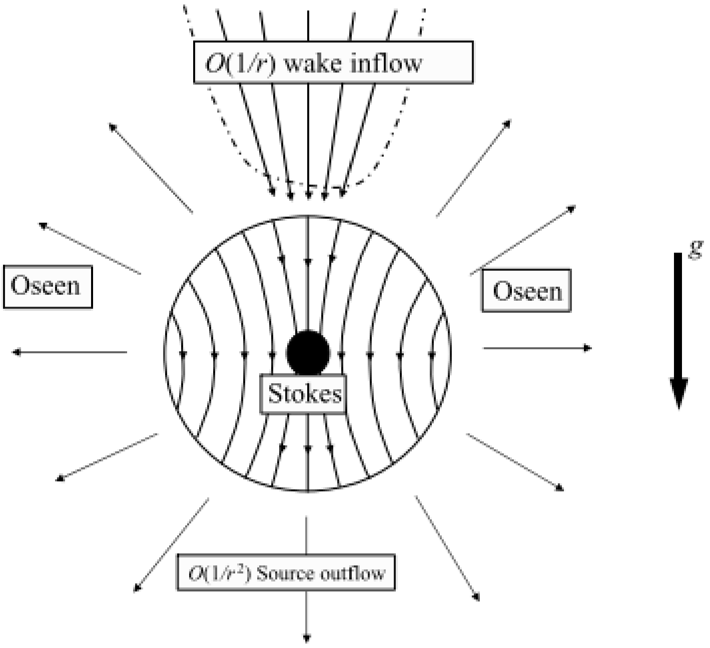

Figure 7: Schematic showing the source-sink character of Oseen flow and its relation to the Stokes solution for flow around a spherical particle. Reproduced from [36].

More research has been done on particle clouds in different types of flows, which we can not all discuss here. The behaviour of particle clouds in a shear flow was investigated experimentally by Metzger and Butler [37] and that in vortical flows by Marchetti et al. [38] and Kriaa et al. [39]. Mylyk et al. investigated experimentally the break-up of particle clouds close to a vertical wall [40]. Machu et al. performed a very elaborate (experimental and numerical) study on the interaction between two suspension droplets [41] and on the settling of suspension drops with a spherical and bell-shape. Pignatel et al. [42] continued the investigation into particle clouds at a finite Reynolds number, as well as Chen et al. [43]. Ayeni et al. [44] also investigated particle clouds at finite Re but with a CFD-DEM approach.

A related but not equivalent problem is that of turbulent particle plumes. These are very prevalent in all types of natural and industrial processes. When the Reynolds number is significantly higher compared to what was discussed prior, a particle cloud undergoes a significant acceleration due to buoyancy (the acceleration stage), after which internal circulatory regions of particles and fluid are established (the thermal stage). Then, the particles separate from the vortex ring and proceed to settle at their individual settling velocities (the dispersive stage) and the fluid vortex ring is left behind (this is all well explained in the canonized work of Morton et al. [45]). It is these particle clouds that are often encountered in practical settings. For example, in the example of sediment reintroduction during nodule harvesting (Fig. 1) it is specifically this type of particle cloud behavior that is relevant. For studies on particle plumes related to deep-sea mining, see [2, 46]. For studies on the effects of polydispersity in particle plume settling, see [47, 48, 49]. Finally, Penlou et al. [10] recently showed how particle clouds can form in turbulent gas-particle suspensions, leading to enhanced settling instead of hindered settling.

2.6.2 Polydisperse clouds

Abade and Cunha [25] were the first to investigate the effect of polydispersity on cloud sedimentation. They employed a Stokesian Dynamics simulation with an artifical lubrication force. The first part of the paper is very similar to the analysis of Nitsche and Batchelor. The mechanism for particle leakage is visualized and based on a novel scaling argument, a formula is derived for the rate expression (which agrees well with the simulation). Furthermore, it is shown that a greater degree of polydispersity (higher standard deviation of the particle size distribution) leads to a higher rate of particle leakage. It is argued that the polydispersity constitute a secondary source of velocity variations (which is associated with leakage). This is because the Stokeslet explicitly depends on the particle size through the applied force (7). It was also found that the effects of polydispersity become pronounced only at higher values of ϕ. Finally, the evolution of three clouds with varying degrees of discrete polydispersity (Fig. 8) suggests that (discrete) polydispersity leads to less ordered collective behaviour of the cloud compared to the monodisperse case. Collective motion may even be not present at all as the polydisperse cloud can disintegrate in the early stages.

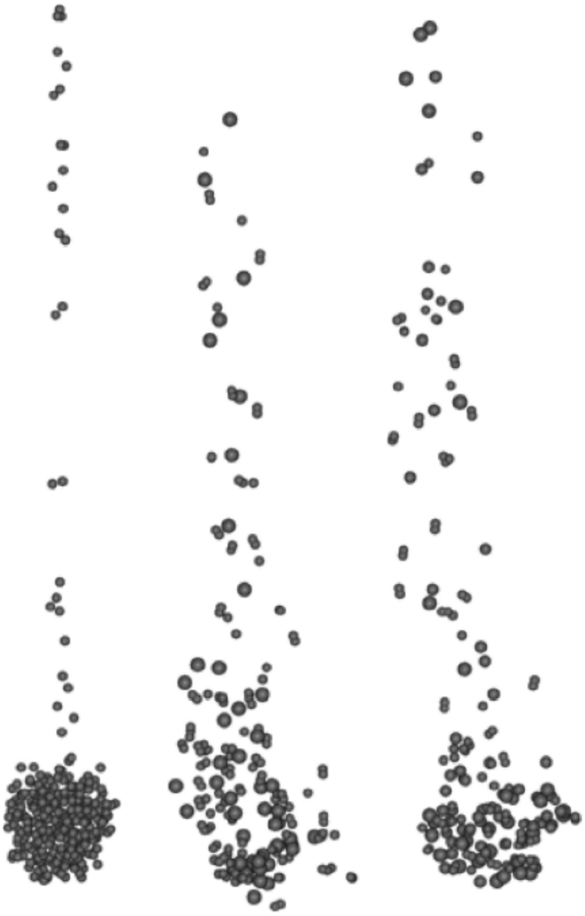

Figure 8: Snapshots of three different settling particle clouds, reproduced from [25]. Left: monodisperse cloud. Middle: Bidisperse cloud with $a_2/a_1 = 1.25$. Right: tridisperse cloud with $a_2/a_1 = 1.25$ and $a_3/a_2 = 1.5$.

Bülow et al. [50] studied numerically the behaviour of a bidisperse and polydisperse settling particle cloud. They employed a Stokesian dynamics like method. Lubrication interactions were not included to decrease computational time by orders of magnitude. For bidisperse clouds, both an unmixed and mixed initial configuration was tested. In the unmixed configuration (with large particles in the upper hemisphere of the cloud), it was observed that the large particles dive through the small particles due to gravity and take some small particles with it. For higher size ratios $\lambda = a_{small}/a_{large}$, significantly more small particles remain in the cloud. In contrast, for smaller λ more large particles are trapped by the trailing small particles and thus leave the cloud. For the mixed case, the particles of both sizes were randomly distributed in the sphere. The size ratio was 0.5 and the initial volume fraction was set to 0.05 (with 1000 total particles), and the percentage of small particles varied from 0 to 95%. A significant difference with the unmixed configuration, is that small particles are better preserved in the cloud (for the mixed case). Moreover, instead of the usual break-up into two clouds, an immediate break-up into three clouds was sometimes seen. Finally, it was shown that a fully polydisperse cloud (N=5000) also undergoes the same characteristic evolution (Fig. **??**). Unfortunately, they did not do a comprehensive analysis on the effects of particle number and solid fraction on the stability of the cloud and the evolution of the particle size distribution. Similar to what Nitsche and Batchelor [24] had done, Metzger et al. proposed a formula for the settling speed of a particle cloud based on the H-R solution, but for the polydisperse case. The formula represents the results of the simulations well, even up to $\phi = 20\%$.

Faletra et al. [51] did a more detailed study on settling bidisperse particle clouds (referred to as suspension droplets). The method used was very similar to that of Nitsche and Batchelor [24], but used the Oseenlet flow field instead of the Stokeslet. For the bidisperse case (two different densities), particle leakage was observed and the lighter particles had a much higher probability of entering the tail (Fig. 9). After waiting for large enough times, all light particles have entered the tail and the droplet consists exclusively of heavy particles (a novel segregation mechanism). Surprisingly, this was also confirmed in the qualitative sense in experiments, even though the experiments required the use of a much higher solid fraction. An increase in the amount of initial particles N_0 led to delayed separation and increased deposition of heavy particles into the tail. This latter result is in contrast to the findings by Metzger et al. [34], who found that in the monodisperse case the amount of leakage decreased with increasing N_0. Faletra et al. argue that due to bidispersity, the heavy particles experience a disturbance due to the relative motion with the lighter particles which causes the increased leakage (which increases with N_0 because smaller particles stay in the drop longer). Finally, a comparison is made with simulations using Stokeslet disturbances. The drops simulated with oseenlets fall slower, which can be explained by the increase in drop size (which leads to a decrease in drop ϕ). The expansion of the drops is associated with the potential point-source in the Oseenlet flow around a particle, causing light repulsion of particles. The segregation mechanism was very similar for the two methods.

Ho et al. [52] studied also polydisperse settling particle clouds, with a Stokeslet-based method. Instead of adding an artificial repulsive force for close particles, the velocity contribution of a particle to its neighbour was neglected if particles were overlapping (as particles were represented as points), similar to previous authors. First, it was shown that polydisperse ('Gaussian') clouds exhibit essentially the same (phenomenological) time evolution as their monodisperse counterparts. Smaller particles were more likely to leave the cloud, corroborating findings of previous studies. Similar to what was argued before, polydisperse clouds are believed to destabilize earlier due to the increased leakage. To test this hypothesis, destabilization times t_{des} and lengths L_{des} were evaluated for monodisperse and Gaussian clouds with

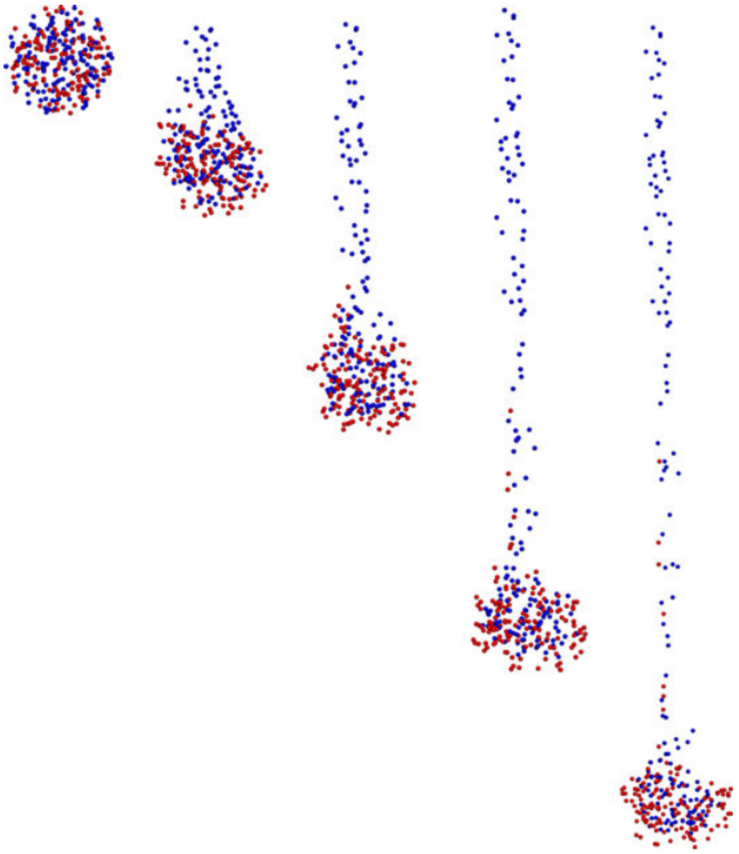

Figure 9: Time evolution of a bidisperse particle cloud consisting initially of 300 particles with a density ratio of 2. The heavy particles are shown in red and the light particles in blue. Reproduced from [51].

approximately the same solid fraction. It is shown that indeed , for Gaussian clouds, t_{des} and L_{des} are significantly smaller. The monodisperse runs also show more variation among the various realizations simulated for the same number of particles and ϕ. It is suggested that because of the increased leakage rate in Gaussian clouds, the simulation result is less dependent on the initial microstructure. It was also found that clouds with greater N_0 are more stable, which was also concluded by Metzger et al [34]. The effect of ϕ on t_{des} and L_{des} was not significant. The finding by Abade and Cunha [25] that increasing the standard deviation of the (Gaussian) particle size distribution leads to less stable clouds was also replicated, but now also in the quantitative sense. Ho et al. also used their simulation to replicate the experiments by Mylyk et al. [40] where a suspension drop with three different sizes of particles settled in glycerol. The general evolution of the experimental and numerical clouds is very similar and perhaps surprisingly, the data for t_{des} and L_{des} generally showed a match.

2.6.3 The suspension drop experiment

In the context of deep-sea mining, some researchers [7] have posited that in order to minimize the ecological impact of DSM operations, it could be interesting to let the sediment particles aggregate with the help of organic material that is present in low concentrations in the upper layer of the ocean bed. These aggregates (so called 'flocs') will have greater settling velocities (because of their larger size) and will therefore not be carried by the turbidity current over larger distances (thereby minimizing its impact). However, it is known that these flocs have a size-dependent density, which impact its settling behavior [53]. In turn, the specific parameters during flocculation (e.g. sediment and flocculant concentration, salinity) determine the size and density of flocs that are formed. For perspective, the range of floc sizes and densities encountered in experiments is between 0-1000 microns and 1010-1300 kg m^{-3}, respectively. This is while the sediment particles have sizes in the range of 5-20 microns and densities upwards of 2500 kg m^{-3}. Both size and density impact the settling behavior, therefore it is crucial to understand the size-density relation of these aggregates. Analyzing the size of flocs using a particle size analyser (PSA) is suboptimal, because the density and therefore the refractive index is size-dependent. The flocs are also not spherical. An error in the estimated size will result in an even larger error in the estimated density, if the Stokes equation is used (where the size is squared). Measuring the density of a polydisperse sample of flocs is difficult for obvious reasons. Hence, Waqas et al. [7, 8] took a different approach, obtaining video footage of flocs settling in water from which the size can be easily determined using image processing software. The effective density ($\rho_f - \rho_w$) can then be determined using equation 6, assuming that each floc is moving at its Stokes velocity. In this experiment, a suspension drop is pipetted from a sample of pre-mixed suspension and released into a water tank where it settles under its own weight as a particle cloud. A schematic is shown in Fig. 12. The particle motion is captured with a camera (a sample image is shown in Fig. 10) and by means of image processing the particle sizes and corresponding velocities are computed.

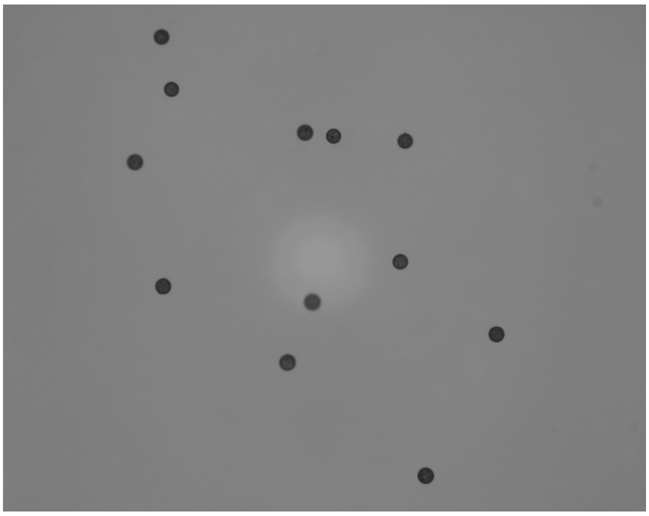

Figure 10: A snapshot obtained from a setup as in Fig. 12 at the Deltares research institute in Delft, The Netherlands.

In one study by Waqas et al., they investigated the difference between settling velocities measured for individual particles and (averaged) velocities measured for suspension drops using equal density and (approximately) monodisperse spherical particles. They found that the settling velocities measured in both scenarios can easily differ by an order of magnitude, which is (correctly) attributed to the effects of enhanced collective settling. In another study, the same type of comparison is made for settling flocs. The measured settling velocities for individual and collective settling flocs and the resulting effective densities are shown in Figure 11. It can be seen that velocities during collective settling again exceed those measured during individual settling (Fig. 11). This leads to large errors when calculating the effective density, illustrated by the huge difference in the obtained size-density curves. This is because a small particle which is settling at the cloud speed, which can be 50 times its actual Stokes velocity,

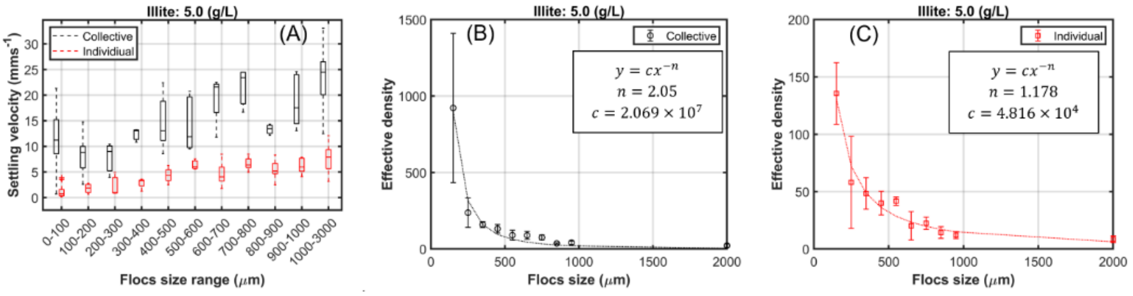

Figure 11: Settling velocities and resulting effective densities for different floc size ranges.

leads to a density that is also 50 times as high as the actual density. For individually settling particles, the settling velocities are more nonuniform and the effective density calculated from the velocity lies in a realistic range, indicating particles were moving at their respective Stokes velocity. But, to obtain such measurements of an individually moving particle (floc), repeated subsampling is necessary. This significantly slows down research efforts as it would take very long to obtain statistics for a range of floc sizes in different flocculation conditions. Hence, Waqas et al. concluded that in order to obtain accurate figures for individual particles' settling velocities, an extremely low number of particles should be used in the suspension drop experiment (SDE). They also mentioned that this would not be needed for monodisperse drops as the measured velocities are more uniform, on which we would comment that the velocities can still be much larger than individual settling velocities regardless of uniformity.

For these reason, it would be highly beneficial to study for what conditions the measured settling velocity in the SDE corresponds (within a reasonable margin) to the single particle Stokes settling velocity. In order to effectively study this problem, some simplifications are in order. First, while the relatively simple setup used (Fig. 12) probably does not guarantee spherical particle clouds without entraintment of outer fluid, the idealized case will be assumed in this study. Moreover, the assumption of rigid inertia-less spheres moving in an inertia-less quiescent fluid enables us to use Stokesian Dynamics as the numerical method. Now, we have seen that the initial velocity of a monodisperse suspension drop can be calculated with

$$\frac{V_0}{V_{\text{s, ref}}} = \frac{6}{5} N_0 \frac{a}{R} + 1, \tag{26}$$

which can be rewritten as

$$\frac{V_0}{V_{\text{s, ref}}} = \frac{6}{5} N_0^{\frac{2}{3}} \phi^{1/3} + 1. \tag{27}$$

First, it can be seen easily that the settling velocity is always above the Stokes velocity. To simplify, we will therefore set an arbitrary but necessary limit of 2 times the Stokes velocity, as the desired settling velocity of the particle cloud. As such, there will still be an error, but it is limited and does not have bounds extending to other orders of magnitude like what was reported by Waqas et al. [8]. Using equation 27, we can calculate for which starting conditions the cloud will settle with a velocity of $2V_s$, e.g. this is the case for N_0=1000 and $\phi = 0.00006$ % or for N_0=100 and $\phi = 0.006$ %. In other words, the initial velocity is only close to the Stokes velocity for (absurdly) dilute clouds and/or for very small particle numbers. However, we have seen that during the settling of a particle cloud, it decelerates due to the steady loss of particles. Moreover, at a certain point in the evolution of a cloud, it can break up into multiple clouds (if the conditions are suitable) or fully desintegrate, leading to a further decrease in the speed of particles. Because the velocity in the setup of Fig. 12 is measured at the lowest part of the vertical column, the suspension drop will have decelerated from its initial velocity, the extent of which needs to be determined. As discussed before, most suspensions are polydisperse. The particular application discussed in the section above involves the highly polydisperse flocs. From the SDE, we want to get the size and density of flocs, for which we would need to measure the particle at its Stokes settling velocity. For simplifying purposes, we will also study when the average velocity of the particles in polydisperse drops equal two times the Stokes velocity of the reference particle used for non-dimensionalisation, which is the particle with approximately the mean size. We will then need to look at to which extent this indicates that each respective size has reached a similar velocity relative to its Stokes velocity.

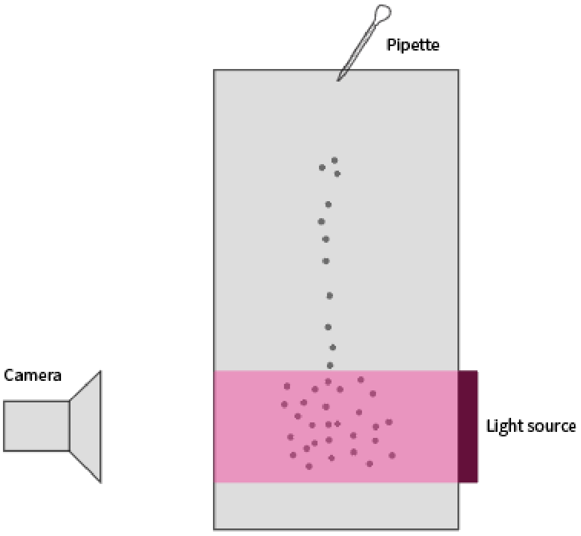

Figure 12: A schematic of an experimental setup that is used to measure the settling velocity of a suspension drop.

In conclusion, we see that the amount of research on polydispersity in settling particle clouds is limited. That is, even though most applied problems involve polydisperse samples. A lot of the present research on polydispersity involves bidisperse particle clouds [50, 51]. To our knowledge, the only research [40, 52] on fully polydisperse clouds looks mainly at the cloud's stability (break-up time and length). As for fully polydisperse clouds, there is also no research into whether these clouds behave differently when the cloud's particle size distribution is either continuous or discrete in nature. Moreover, as previously explained there is a need for applying the current knowledge of (both monodisperse and polydisperse) particle clouds to study the specific conditions for which the velocity of collectively settling particles in a setup similar to Fig. 12 is close to the Stokes velocity.

2.7 Research outline

The main objective of this thesis is to help experimental researchers in finding the conditions - i.e. the number of particles, volume fraction, mean size and polydispersity - for which measuring average particle settling velocities from settling suspension drops gives a measure sufficiently close to the single particle Stokes velocity and to see how this differs for mono- and polydisperse drops.

- **For what conditions do average velocities measured from settling monodisperse suspension drops reach two times the single particle Stokes velocity?**

  Stokesian Dynamics simulations are performed for monodisperse particle clouds settling under gravity for different N_0 *and* ϕ*. The settling speed, leakage rate and expansion rate are studied and compared to theoretical predictions.*

- **For what conditions do average velocities measured from settling polydisperse suspension drops reach two times the Stokes velocity according to the mean (reference) size?**

  Stokesian Dynamics simulations are performed for polydisperse particle clouds settling under gravity for different N_0*,* ϕ *and* σ*. The settling speed, (size-specific) leakage rate and expansion rate are studied for different polydispersity degrees.*

- **What qualitative and quantitative differences exist in the settling behaviour of polydisperse particle clouds with a discrete particle size distribution compared to clouds with a continuous particle size distribution?**

  Stokesian Dynamics simulations are performed for polydisperse particle clouds settling under gravity with discrete particle size distributions and a continuous particle size distributions. The destabilization time and length, settling speed and (size-specific) leakage rate are compared for the two types of distributions.

3 Method

3.1 Description of the numerical simulations

The numerical method that will be used in this study has been introduced earlier, see 2.5. Here, we expand on its specific implementation in this project. We consider sedimentation of a particle cloud consisting of non-Brownian, inertialess particles. The particles have equal density, but may vary in size in the polydisperse simulations. Moreover, the conditions of Stokes flow are assumed. We simulate the cloud of particles in an unbounded fluid, i.e. the influence of any boundary (e.g. container walls) is not included. Initially,the particles idealized as perfect spheres are randomly placed inside a sphere (without overlapping), such that the volume fraction is equal to the desired value. The particle positions are updated using the numerical scheme (Stokesian Dynamics), with only the force-velocity coupling. The torque and stresslet contributions are thus neglected, which is reasonable for the case of sedimentation. Also, lubrication forces are neglected, as this speeds up the simulations by several orders of magnitude [50]. Also, only dilute systems ($\phi < 5\%$) will be considered. Moreover, it has already been shown that both qualitative and quantitative aspects of the particle cloud can be reproduced using even simpler schemes [34]. The velocities of the spheres are calculated according to:

$$\mathbf{U} = \mathscr{M}^{\mathrm{FU}} \cdot \mathbf{F}_{\mathrm{e}} \tag{28}$$

which is equivalent to Eq. 24 if $\mathbf{U}^{\infty} = 0$ and the stresslet contribution is neglected. Remember that this equation was specifically derived for the case of inertialess particles. The mobility matrix $\mathscr{M}^{\mathrm{FU}}$ is computed using the method by (Ref Brady 1987) and includes self-interactions as well as two-sphere mobility interactions. The external force $\mathbf{F}_{\mathrm{e}}$ is the sum of gravity and buoyancy. Finally, the particle positions are updated using a two-step Adams-Bashforth method, with non-dimensional timestep $\Delta t^* = 0.01$.

Note that all the relevant equations are non-dimendionalized. In the literature, the most common practice in the context of particle clouds is to use the initial cloud radius R_0 and velocity V_0 and their ratio $\tau_c = R_0/V_0$ to non-dimensionalize distance, velocity and time, respectively [24, 34, 40]. Sometimes, the use of the single particle Stokes velocity U_{S} is encountered instead of V_0 [51, 52] or the use of a particle radius a_{ref} instead of R_0. In this study, we use the mean particle radius $a_{\mathrm{ref}} = \langle a \rangle$ and Stokes velocity of this reference particle $U_{\mathrm{S}} = \frac{2}{9}\frac{\langle a \rangle^2}{\mu}(\rho_p - \rho_f)g$ to non-dimensionalize distance, velocity and time. In this way, the radius of particle i is given either by 1 (monodisperse case) or by the aspect ratio $\lambda_i = \frac{a_i}{\langle a \rangle}$, and the time by $t^* = t/t_s$. The Stokes drag $6\pi\mu\langle a \rangle U_S$ is used to non-dimensionalize the force. The reason for the choice of scaling was mainly the fact that there existed in house code that used this, and to stay consistent with this made cooperation on the project easier. Moreover, a benefit of this scaling is that the cloud velocity can be immediately related to the single particle Stokes velocity, and the cloud position to the individual particle size. However, at several points in this study we will also convert the data so that it is expressed in $t_c^* = t/\tau_c$, as this makes it easier to compare particle clouds. Note that for most particle clouds considered here, the ratio of the time scales $\frac{R_0}{V_0} / \frac{\langle a \rangle}{U_S}$ is close to one and it has little influence on the size of the time steps. Only when considering extremely dilute particle clouds (large R_0 and small V_0) the ratio becomes large and using the current scaling severely slows down the simulation. For these cases, the timesteps were adjusted accordingly. Finally, the calculated particle position and velocity vector components are written to a file every 10 time steps for later analysis.

3.1.1 Generation of particle clouds

As previously mentioned, particles are randomly positioned inside a sphere, of radius $R_0 = \sqrt[3]{\frac{\Sigma a_i}{\phi}}$, and any overlapping particles are removed until the desired amount of non-overlapping particles has been achieved. In monodisperse clouds, all particles have non-dimensional size 1. Particles in polydisperse clouds have non-dimensional size ranging from 0.1 to 2.0, with an interval of 0.1. The degree of polydispersity is expressed with the parameter $\sigma = \sigma_a/\langle a \rangle$, where σ_a is the standard deviation of all particle radii about the mean $\langle a \rangle$. The sizes are sampled from a log-normal distribution with mean 1 and a standard deviation ranging from 0.1 to 0.5 for the different simulations. When the standard deviation is between 0.1 and 0.3, a limit of 4 is set on the maximum size ratio of two particles to filter any particle outliers that have unrealistically small or large size. Practically, this means that only particles with an aspect ratio between 0.4 and 1.6 are present in the particle cloud. For higher standard deviation, this restriction was lifted, otherwise it was not possible to get clouds with higher standard deviations that are log-normally distributed. In this case, the sizes were between 0.1 and 2.0. As for the clouds with only discrete particle sizes, instead of sampling N sizes from a distribution, we need the frequencies of sizes 0.1 ... 2.0 according to the log-normal distribution. These frequencies are calculated using

$$f_i = (\Phi(a_{i+1}) - \Phi(a_i)) \cdot N, \tag{29}$$

where $\Phi(x)$ is the cumulative distribution function of the log-normal distribution and $\Phi(a_i)$ is the cumulative probability corresponding to size a_i. These frequencies are then rounded, giving the discrete particle size distribution. Finally, for the higher standard deviations (0.3-0.5), the actual standard deviation of the particles will be lower than the distribution from which the sizes are sampled, due to the bounds on particle size. The mean will also be lower, as mostly larger sizes will be eliminated (because of the log-normal distribution). The generated size distributions as well as the actual values of the particle number N_0, the mean size $\overline{a}$ and the polydispersity parameter σ are shown in Appendix A.

3.1.2 Overlapping particles during simulation

The initial state of non-overlapping particles obviously does not guarantee that particles will not overlap during the simulation. To deal with this, several approaches are used. Two of these were already mentioned in the review of literature, namely the inclusion of an 'artificial' repulsive force and the filtering of simulation runs where particles get so close that their sedimentation velocity exceeds that of the cloud. In the current study, we do not include an artificial lubrication force. Rather, for any overlapping pair of particles i and j, when considering the contribution to the velocity of particle i due to the force on particle j (which depends on their interparticle distance), the distance is taken as approximately the sum of the particle radii. This prevents the unrealistic velocity increase due to the singularity at r = 0. This approach is similar to that of Ho et al. [52], except that they totally neglect the velocity contribution of overlapping particles. Note that overlap of particles will not be prevented, and as such this simulation method does not account for excluded-volume effects. Still, the use of this method is justified as point-particle simulations have been effectively used to study the behaviour of particle clouds and we only consider small volume fractions. Moreover, the use of artificial repulsive forces has been shown to arbitrarily influence the dynamics of the simulation [54]. It has not been investigated if the approach used in this study has a similar effect or not.

3.1.3 Post-processing methods

As mentioned before, the data available from the simulations are the components of the position and velocity vectors of all particles, corresponding to times $t_i^* = 0.1 \cdot i$. From this data, we wish to compute the position and velocity of the particle cloud, the amount of particles still present in the cloud, and the (approximate) horizontal and vertical radii of the cloud. To this end, we used the same conventions as Metzger et al. [34] for defining which particles belong to the cloud and how to compute its horizontal and vertical radii. As has been mentioned before, the evolution of a suspension (drop) is very much dependant on the initial configuration. It is therefore customary to run multiple simulations for each particle cloud, each having a different (random) initial configuration of particles, and from this ensemble of data the macroscopic quantities of the cloud can be obtained by averaging. In the current study, there was unfortunately not plentiful time to perform multiple simulations per cloud.

3.2 Validation of the numerical method

For validation purposes, we considered the standard sedimenting pair and the case of a sedimenting particle cloud. The goal of this section is to show the validity of the numerical scheme and its effectiveness in reproducing well studied phenomena.

3.2.1 The two particle test case

The interaction between a pair of hydro-dynamically interacting particles has been thoroughly studied. The accepted benchmark solution for two identical spheres settling in an unbounded fluid at small Re is that given by Goldman et al. [55]. In Fig. 13, this solution is compared to the velocities resulting from our method, at different separations and both for the horizontal and vertical pair (relative to gravity). It can be seen that the mobility scheme is more accurate than the point force model, which is expected as the mobility scheme includes higher-order terms. The mobility scheme is fairly identical to the solution at $r/a \gtrsim 4$, and deviates from it as the interparticle distance is further decreased. The error generated by the mobility scheme reaches a maximum of approximately 5 % at the closest separation, as was reported in similar accounts [50]. Also note that the error for vertically oriented particles is greater, as the lubrication force arising from squeeze flow is greater than that arising from shear flow.

3.2.2 The initial cloud velocity

Next, we consider a particle cloud. In order to validate the numerical scheme for both the monodisperse as well as the polydisperse case, we considered a monodisperse as well as a bidisperse particle cloud of varying composition (see Fig. 14. The size ratio of the two particle species is set to 0.25, and their relative number is varied, but the total number of particles and the volume fraction is kept constant. The data compared against are obtained from the analytical formula derived by Bülow et al. [50], which was validated against results from their simulations, in the study that was described in Section 2. The results show good agreement, which increases for a larger proportion of the small species, which is expected as the existing mass becomes more finely distributed.

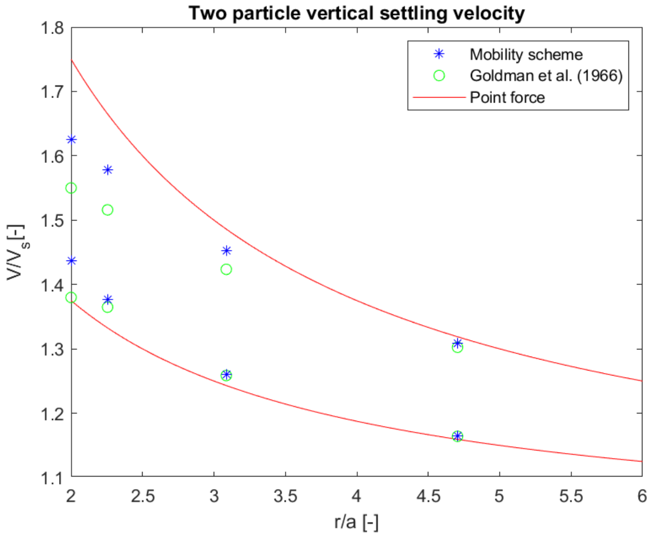

Figure 13: Various estimates of the settling velocity of a pair of identical spheres as a function of the non-dimensional interparticle distance.

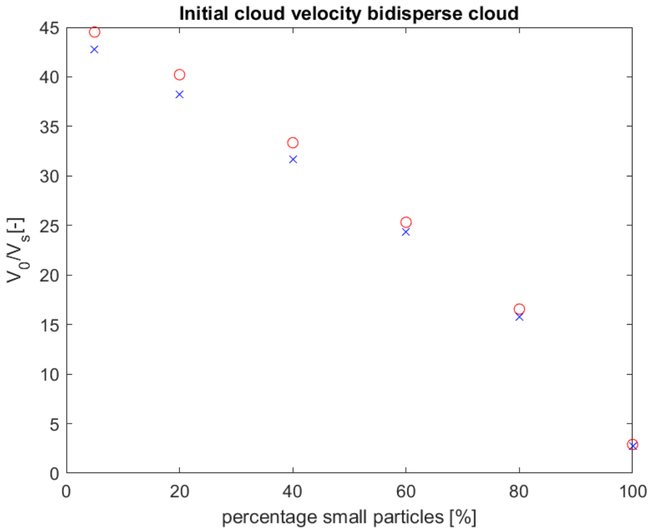

Figure 14: The initial non-dimensional velocity of a bidisperse cloud as a function of the ratio of particle numbers. The red circles are the values from simulations and the blue crosses are the computed values from the formula of Bülow et al. 38

4 The monodisperse particle cloud

In order to make a good prediction on which suspension drops will decelerate enough to reach at least twice the single particle settling velocity $2U_s$, we need to know the initial cloud velocity, as well as the deceleration profile as a function of time and how these depend on the cloud variables, i.e. the number of particles N_0 and the volume fraction ϕ. These last two variables can be interchanged with N_0 and R_0 (the initial cloud radius) or R_0 and ϕ.

4.1 Evolution of a monodisperse cloud

4.1.1 Cloud expansion, deceleration and particle leakage

The analysis that will be presented here is very much inspired by the work of Metzger et al. [34], that was already discussed at an earlier stage. In this work, they found approximate correlations for the evolution of the cloud relative radius $R^*=R/R_0$ and relative particle number $N^*=N/N_0$ as a function of non-dimensional time t_c^* and the initial number of particles N_0. They found that the decrease in the relative velocity of the cloud $V^*=V/V_0$ can be explained entirely by the decrease in the particle number and increase of the horizontal radius of the cloud, as the data from all simulations collapses onto a single straight line when plotting V^* against N^*/R^* (the greatest contributor to deceleration being the decrease in particle number). Note that Metzger et al. ran point particle simulations, where the volume fraction is a meaningless quantity. In our simulations, we do not non-dimensionalize by the initial cloud velocity but by the single particle Stokes velocity, and thus a cloud with the same number of particles but a higher (lower) volume fraction will have a higher (lower) velocity. The dynamics will also be different from the point-particle case. For a higher volume fraction, there is a greater probability that two particles' surfaces will cross paths and if they do, there will neither be a repulsion nor an nonphysical increase in velocity caused by the singularity in the mobility interactions. But considering that Metzger et al. carefully filtered out cases where the latter occurs, it was anticipated that the results from our simulations closely align with theirs.

Figure **??** how the plots of R^*, N^* and V^* for different values of the initial number of particles N_0. The dashed lines are plotted using the approximate correlations derived from [34]:

$$N^* = 1 - 0.52 N_0^{-2/3} t_c^{*0.636} \tag{30a}$$

$$R^* = 1 + 0.0811 N_0^{-0.65} t_c^*. \tag{30b}$$

Overall, there is agreement between the data. More importantly, we found the same result for particle leakage, that it grows proportional to $t_c^{*2/3}$ (see Fig. 26). Metzger et al. mentioned that the correlation for N^* is only valid for large N_0. It can be seen here too, that the agreement is poor at low N_0. Note that the precise mechanisms involved in the expansion of the particle cloud are unclear [34]. However, the difference in rate of expansion for different N_0 only accounts for small differences (a torus experiences more drag than a sphere) in the velocity V^*. Hence, we are not too concerned with minor differences in the rate of expansion. The dashed lines in the plot for V^* originate from the same expressions for N^* and R^*, combined with the linear relation

$$V^* = 0.108 + 0.908\ N^*/R^*. \tag{31}$$

found in the study of Metzger et al. and corroborated in our simulations.

Using the resulting formula for the velocity, the relative velocity V^* is now a function of the non-dimensional time time t_c^*. Using this expression, we have a theoretical basis for estimating which particle clouds (defined by N_0 and ϕ) decelerate to at least twice the single particle Stokes velocity, within a pre-chosen distance (1 meter). Note that the correlation for N^* will cross zero and become negative (with V^* still decreasing), which is of course nonphysical. Moreover, we now that the velocity of particles will not be smaller than U_s (unless $\lambda_i<1$ which occurs only in polydisperse clouds). These are the bounds within which the formula holds any significance, also noting that because of considerations mentioned previously the velocity of a spherical cloud of particles will only approach the Stokes velocity in the case of extremely

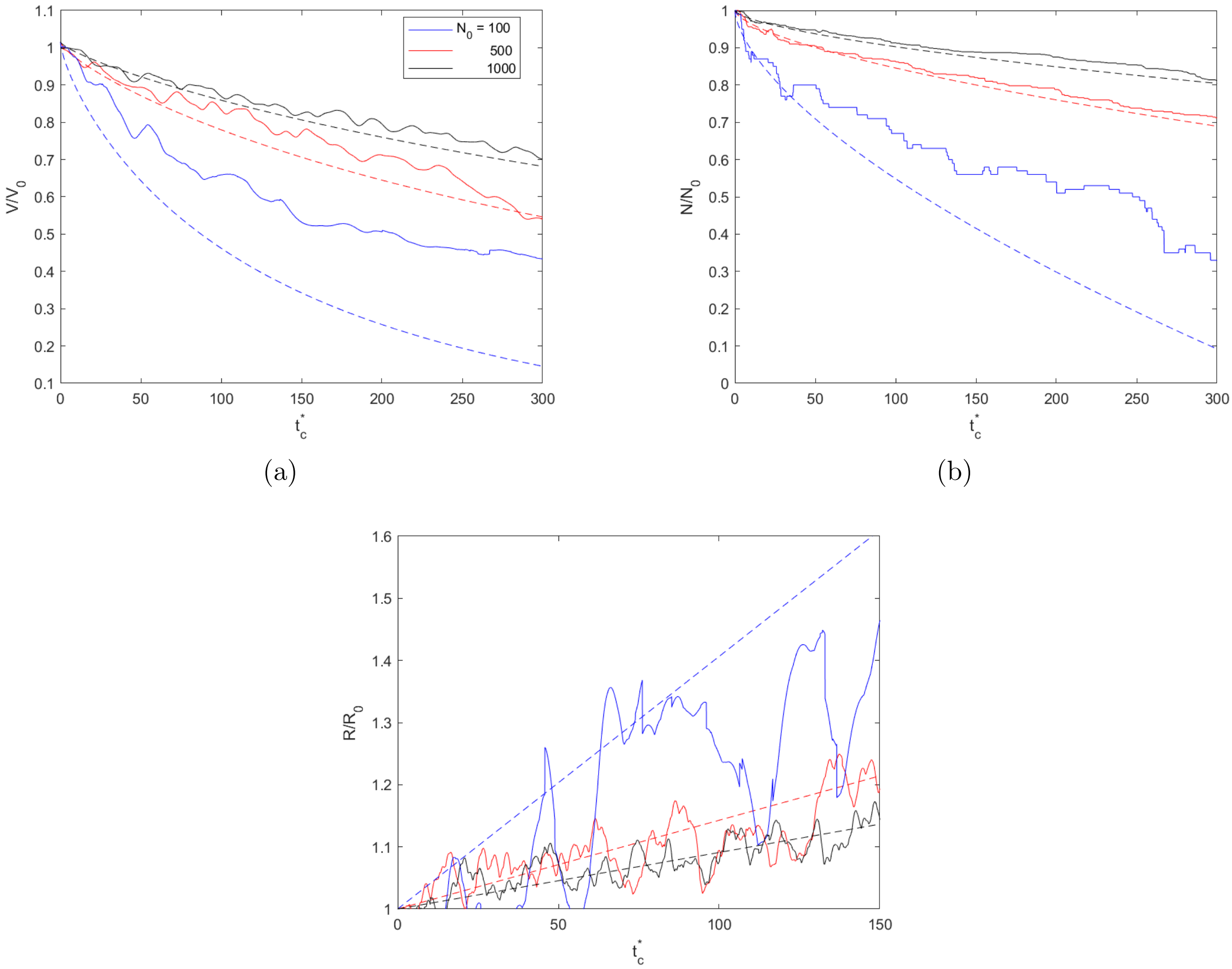

(a)

(b)

(c)

Figure 15: The (a) relative velocity, (b) particle number and (c) radius of a settling monodisperse cloud for different particle numbers compared against the prediction (dashed lines) from the simulations of Metzger et al. [34].

diluted particle clouds with only a dozen to a couple dozen particles. Moreover, we are not interested necessarily in quantitative results here as these can be obtained by simulation, but more in a qualitative trend so that we can make predictions about the effect of N_0 and ϕ that can be validated in the simulations.

We want to solve $\mathrm{V}/\mathrm{V}_s = 2$, where the left-hand side can be written as

$$\frac{V}{V_s} = V^*(t_c^*)\,\frac{V_0}{V_s} = \left(0.108 + 0.908\frac{N^*}{R^*}\right)\left(\frac{6}{5}N_0^{2/3}\phi^{1/3} + 1\right). \qquad (32)$$

This equation was solved numerically for $100 \le N_0 \le 1000$ and $0.001\% \le \phi \le 5\%$. This gives an approximation of the time, $t^*_{c,crit}$, at which $\mathrm{V}=2\mathrm{V}_s$. The approximate distance the particle cloud has travelled between $0 \le t \le t^*_{c,crit}$ is computed using integration. Of course, this distance is non-dimensional and the actual distance will depend on the reference size used, which in our case corresponds to the mean size. The formula for this distance is

$$d = \int_0^{t^*_{c,crit}} V^*(t_c^*)\frac{V_0}{V_s}\,dt_c^*\,(\tau_c\langle a\rangle) = \int_0^{t^*_{c,crit}} V^*(t_c^*)\,dt_c^*\,(R_0\langle a\rangle), \qquad (33)$$

where τ_c is merely a factor to account for the different non-dimensionalizations and $\langle a \rangle$ is the mean size of the particles. Based on this, an upper limit in the mean particle size$\langle a \rangle_{crit}$ is calculated, for which it can be theorized that those particle clouds will have decelerated to $2V_s$ at the cut-off distance of 1 meter. Table 1 shows values of $\langle a \rangle_{crit}$ for different values of N_0 and ϕ. Note that rounding to two significant figures does not imply this degree of accuracy but rather allows for interpolation. Note that there is a trend of increasing size with increasing volume fraction, for $0.1\% \leq \phi \leq 5\%$. This may seem counter-intuitive, as an increased volume fraction leads to a higher initial velocity. The reason for this is that when the volume fraction is increased, the average inter-particle distance is decreased, causing a larger leakage rate because of the increased probability for random velocity fluctuations. In turn, particle leakage is the primary cause for deceleration of the particle cloud. This is illustrated in figure 16 by comparing the velocity for the same N_0 but different volume fraction, but now against $t^*=t/t_s$. Remember that the volume fraction did not explicitly appear in the equation for $V^*(t_c^*)$, because time is non-dimensionalized by the cloud time constant τ_c. For example, compare the same cloud velocities in figure 16, but now against t_c^*. For smaller volume fractions, depending on the particle number, the maximum size may also increase because the initial velocity is sufficiently close to $2V_s$. Note that because the distance from the simulation is non-dimensional, if a tank with a smaller height was used for the suspension drop experiment, the upper limit on the mean size can be calculated simply by multiplying the given $\langle a \rangle_{crit}$ with the height of the tank in meters. E.g. if the tank was 25 centimeters high and we read $\langle a \rangle_{crit} = 40\,\mu m$ from the table, then in fact $\langle a \rangle_{crit} = 10\,\mu m$.

N_0	0.001 %	0.01 %	0.1 %	1 %	5 %
100	$V_0 = 1.6V_s$	1000	419 (31 mL)	500 (5.2 mL)	700 (2.9 mL)
250	1000	78 (5 mL)	81 (0.56 mL)	**120 (0.18 mL)**	**190 (0.14 mL)**
500	28 (4.6 mL)	20 (0.17 mL)	27 (0.04 mL)	**45 (0.019 mL)**	**70 (0.014 mL)**
750	10 (0.31 mL)	10 (0.03 mL)	**15 (0.011 mL)**	**25 (0.0049 mL)**	**39 (0.0037 mL)**
1000	6 (0.09 mL)	6 (0.009 mL)	**10 (0.004 mL)**	**16 (0.0017 mL)**	**25 (0.0013 mL)**

Table 1: The predictions of the critical value (upper bound) a_{crit} of the particle size for which the monodisperse cloud decelerates to double the single particle Stokes velocity within 1 meter of settling distance. Bold values indicate that $V=2V_s$ is only reached once $N^*<0$.

The volume of a spherical drop of certain volume fraction containing N_0 particles of size $\langle a \rangle_{crit}$ is also given in the table, though its calculation is straightforward. Note that this is the maximum drop volume, because for smaller particle sizes $a < \langle a \rangle_{crit}$ but equal N_0 and ϕ the volume must decrease. From the values of $\langle a \rangle_{crit}$ and the maximum drop volumes, we can conclude that the success of the suspension drop experiment is very sensitive to the mean particle size in the drop, the volume fraction and especially the number of particles N_0. For example, if the mean size in the drop is $100\,\mu m$, the initial number of particles has to be equal to or less than 250. As for the drop volumes, the two experimental studies on the settling of suspension drops [34, 40] visualize drops with a size as low as 0.005 mL and as high as 0.2 mL, thus spanning approximately three orders of magnitude. Most of the drops derived from table 1 have the same orders of magnitude. At N_0=100, the maximum volumes are on the orders of O(1) and O(10) milliliters, meaning that the actual size limit is probably lower as it would be difficult to generate a suspension drop this large. The converse can be true for some very small drops containing small particles. Finally, bold text indicates that the formula predicts that the cloud velocity will only reach $2V_s$ once $N < 0$. This is of course unphysical, but while the formula assumes that the only mechanisms of deceleration are particle leakage in and expansion of the particle cloud, in reality the cloud will break up or desintegrate at some point and the particles' velocities will continue to decrease due to weaker hydrodynamic interactions. Note that for $500 < N \leq 1000$, there is a large probability that the particle cloud will break up into two clouds. Ho et al. [52] found that this occurs at a time t_{des} when the average velocity in the interval $0 \leq t \leq t_{des}$ is equal to approximately 0.82 times the initial velocity of the cloud. Hence, for most clouds with N between 500 and 1000, and volume fractions greater than 0.01 %, break-up will occur before the particle cloud decelerates to $2V_s$. This is obviously not included in the model, but will be discussed later.

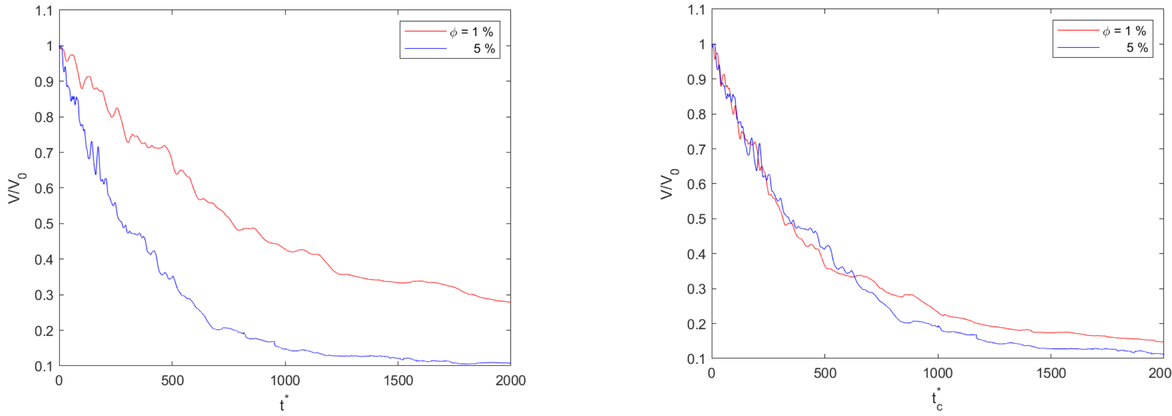

(a)

(b)

Figure 16: A comparison of the relative velocity of two particle clouds, with same N_0 but different ϕ, showing that the curves overlap when scaling time with τ_c instead of t_s.

4.2 Comparing the predictions with simulations

Here we will compare the theoretical prediction against simulations. The simulation runs include N_0=100, 250, 500, 750, 1000 and ϕ = 0.001, 0.01, 0.1, 1, 5 %. The results are shown in Fig. 17. For N_0=500 and 1000, we show cases with low volume fractions because otherwise cloud break-up will have occured long before $V=2V_s$. Even in the case of N0=1000 and ϕ=0.001%, break-up occurs at t_c^*=550 when $V=2.3V_s$. Overall, there is qualitative agreement in the shape of the curve, but the velocity decrease is consistently overestimated. This is especially the case for low N_0. Nonetheless, equation 32 still captures the effects of N_0 and ϕ on particle leakage, which is the main mechanism for the velocity decrease. Note that the data in Fig. 17 is plotted against t_c^*. If plotted against t^*, it would become more apparent that leakage is much slower for lower volume fractions, e.g. for the two lower plots in figure 17 t^* is equal to 22560 and 73840 at the latest time considered, respectively. The trend observed from table 1 is also confirmed. At low volume fractions - if the initial velocity V_0 is not already sufficiently low - the velocity decrease is so slow that a higher a_{crit} can be achieved by increasing the volume fraction. This is a good finding for the experiments, as sufficiently high volume fractions allow for better visualization of the particles. If we were to determine new values of the time at which $V=2V_s$ using the cloud velocity from simulations, the resulting values $t^*_{c,crit}$ would be higher resulting in lower values of a_{crit} than those in Table 1. However, note that it would be arbitrary to take the point at which the curve in Fig. 17 crosses 2 to determine values for a_{crit}. While this would ensure that the measured velocity is smaller than 2, the 'cloud' by this point usually consists of a very small amount of particles, especially at higher volume fractions. The remaining particles' velocities (which are lower) will also be measured. As a result, the mean velocity of all measured particles will equal to 2V$_s$ at an earlier time. This will be investigated in the next section.

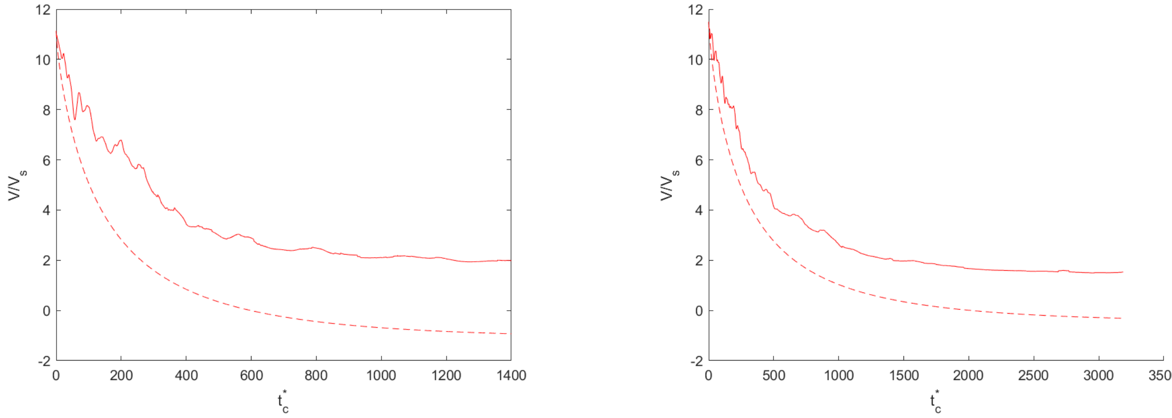

(a) N$_0$=100, ϕ=5%

(b) N$_0$=250, ϕ=1%

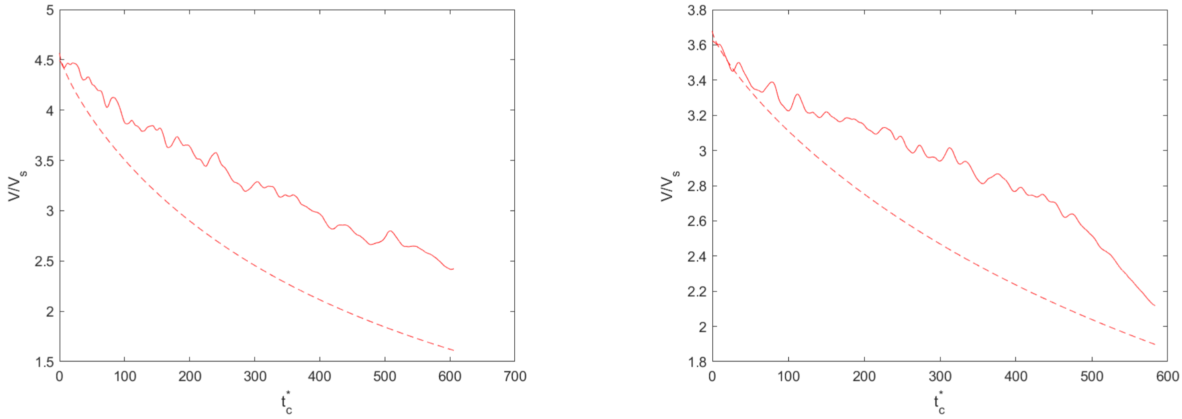

(c) N$_0$=500, ϕ=0.01%

(d) N$_0$=1000, ϕ=0.001%

Figure 17: A comparison of the cloud velocity from simulation as well as the modelled velocity (dashed lines).

4.3 Taking into account the velocity deviation due to tail particles

Once particles leak from the cloud (at the velocity of the cloud), they start rapidly decelerating. As an example, the velocity of an arbitrary particle was plotted in Fig. 18. At the moment of leaving the cloud (marked in the figure), it is moving approximately at the velocity of the cloud, after which the velocity drops to 2V$_s$ within 200 t$_s$ (and keeps dropping after). Some particles can reach their Stokes velocity, but other particles will remain settling at slightly higher velocities due to hydrodynamic interactions with neighbouring particles, with the amount of neighbouring particles depending on N$_0$ and ϕ. In the suspension drop settling experiment as explained here, the velocity of these particles referred to as 'tail particles' will also be measured by the camera, since it is at a fixed position. Therefore, the average velocity of all particles will be lower than the velocity of the cloud, due to these slower moving particles. We will apply a simplified analysis to quantify the effect of these particles on the measured velocity. Here, we call the average velocity of all measured particles V$_{avg}$. If at the position of measurement the cloud contains N$_{cloud}$ particles and sediments at speed V$_{cloud}$, there will be N$_0$−N$_{cloud}$ tail

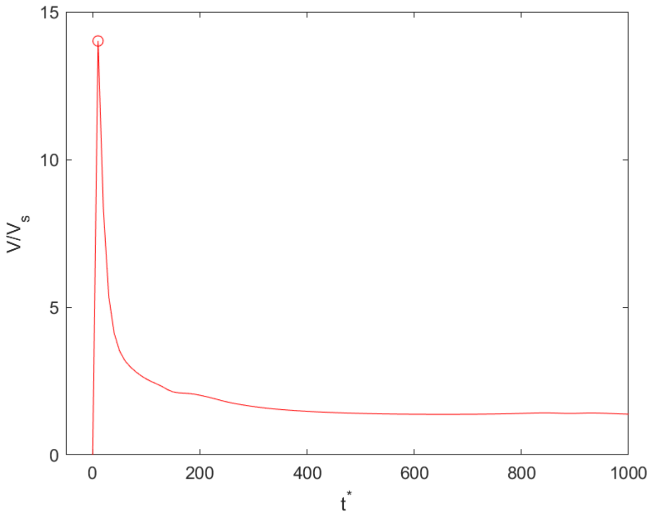

Figure 18: The velocity of a particle after leakage from the particle cloud (N_0=1000, ϕ=0.25%) at t^*=0.

particles trailing the cloud that will be measured at a lower speed, approximated by an average speed $V_{tail,avg}$. The average speed of all the measured particles will be:

$$V_{avg} = \frac{N_{cloud}V_{cloud} + N_{tail}V_{tail,avg}}{N_0} = \tag{34}$$

$$= \frac{N(t_c^*)V(t_c^*) + (N_0 - N(t_c^*))\, V_{tail,avg}}{N_0} = \tag{35}$$

$$= \frac{N(t_c^*)}{N_0}V(t_c^*) + \frac{N_0 - N(t_c^*)}{N_0}V_{tail,avg} = \tag{36}$$

$$= V_0\, V^*(t_c^*)\, N^*(t_c^*) - V_{tail,avg}\, N^*(t_c^*) + V_{tail,avg}. \tag{37}$$

Where we can use the correlations found for N* and V* and the equation for V_0 (Eq. 27). The choice for $\langle V\rangle_{tail}$ is not straight forward as it is difficult to quantify what will be the average velocity of tail particles. It goes without saying that $\langle V\rangle_{tail,min} = 1$. For simulations of clouds with N $<$ 1000 particles and $\phi < 0.05$, we see that it takes on values between 1 and 3. If it is greater than 2, it clearly will not effect when the average velocity of all particles becomes equal to 2. Therefore, let us consider values between 1 and 2. Using equation 34 we can calculate (in a similar way as before) that changing the value of $\langle V\rangle_{tail}$ from 2 to 1 causes a 30-40% difference in the predicted value of $\langle a\rangle_{crit}$, which does not depend much on the choice of N_0 or ϕ.

4.4 The mean velocity

Figures 19 shows the mean velocity of all particles against time. Now, the cloud is the only uniformly moving entity (the remaining 'tail' particles being scattered), so the mean of all tail particles at one time t* does not represent the mean $\langle V\rangle_{tail}$ which is measured at one position. Yet, figure 20 shows there is actually little difference in the velocity of tail particles, except for particles that have just exited the particle cloud. Hence, it is expected that the mean velocity of all particles at one time instance t* can be used as an estimate of the average velocity of all particles passing the position d*, where d* is the position of the cloud at time t*. This was validated by comparing the mean velocity of all particles with the mean velocity computed in a similar manner as in equation 34, but now instead of using the correlations to define N_{cloud}, V_{cloud} and N_{tail}, we use the data from the simulations. Curves with different values for $\langle V\rangle_{tail}$ are shown. The lower value was derived by taking the mean velocity of tail particles at a time instance where the velocity of most tail particles exhibited little variation (similar to Fig. 20). The higher value is simply incremented by 1, to illustrate what the difference would be. The particle cloud velocity is also shown. It can be seen that there is good agreement between the mean velocity in time and the model of measured average velocity per position. It can also be seen that the exact value for V_{tail} does not make a large difference, except at low velocities and for determining the large time limit of the mean velocity. Hence, we expect that the mean velocity from the simulation gives a good indication of the average velocity of all particles measured at a certain position. In any case, this estimate will be conservative because the particles not at the cloud position at any time will decelerate even further until they reach that position. We use the mean velocity to define new values for $\langle a\rangle_{crit}$. These values are given in

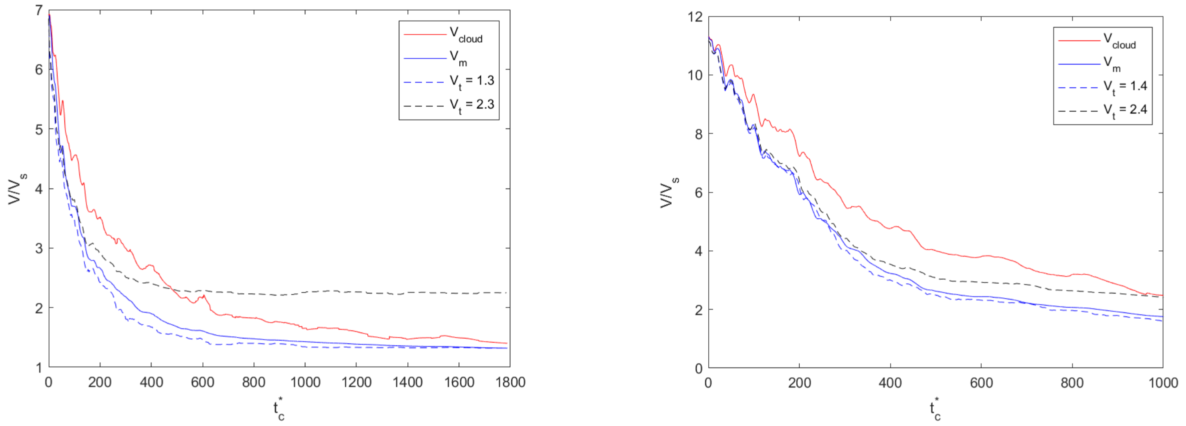

(a) N_0=100 (b) N_0=250

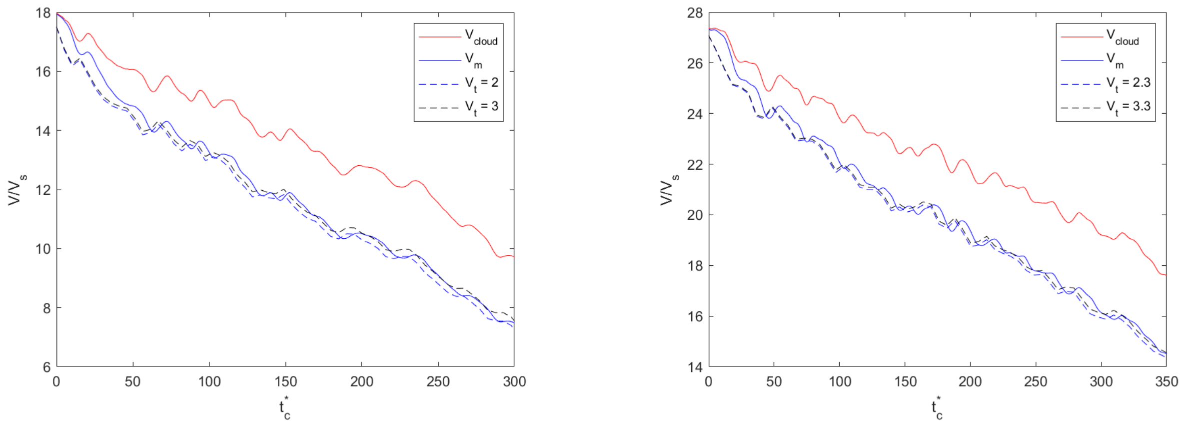

(c) N_0=500 (d) N_0=1000

Figure 19: A comparison of the velocity of the cloud, with the mean velocity of all particles. The mean velocity is significantly lower, due to the slower moving tail particles. The dashed lines represent a modelled average velocity of all particles that pass the position of the cloud at t_c^*. There is good agreement, indicating that the mean velocity at a certain position is a good measure of the average velocity that would be measured at that position. It can also be seen that the chosen value for the (average) velocity of tail particles, when chosen between 1-3 V_s, does not impact the average velocity much except for the asymptote value of the mean velocity of all particles.

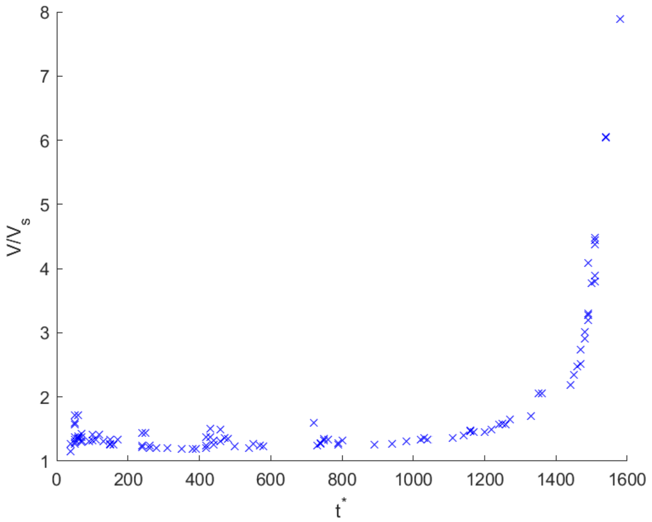

Figure 20: The crosses are the velocities of tail particles at time t*=1600. The horizontal coordinate t* is the time at which the respective particle leaked from the cloud. It can be seen that there is little variation in the velocity of tail particles, except for particles that exited the cloud recently.

Table 2. We can see qualitative agreement with Table 1. The expectation of increasing a_{crit} with increasing volume fraction is also confirmed. However, when going from a volume fraction of 1% to 5%, the increase is less or there may even be a decrease. There is probably a point of diminishing returns, where even though the cloud breaks up faster, the remaining particles settle closer together due to the higher initial volume fraction. As a result, the particles settle a similar distance until the average velocity is equal to $2V_s$. Furthermore, note that the difference between the velocity and mean velocity will be less for less dense clouds, where the velocity of particles in the cloud is already quite low.

N_0	0.001 %	0.01 %	0.1 %	1 %	5 %
100	$V_0 = 1.6V_s$	230	210	260	310
250	210	36	50	80	130
500	17	14	23	70	68
750	6	8	21	39	46
1000	5	9	18	30	29

Table 2: The predictions of the critical value (upper bound) a_{crit} of the particle size for which the monodisperse cloud decelerates to double the single particle Stokes velocity within 1 meter of settling distance, estimated using the mean velocity of all particles. If the mean velocity becomes equal to $2V_s$, the position of the particle that has travelled the farthest is used for calculation (as a conservative estimate, the other particles will still decelerate until reaching this position).

4.5 Cloud break-up

For clouds that break up into multiple clouds and not by steady desintegration, the moment where the mean velocity of all particles reaches $2V_s$ is also dependent on the time of break-up. There is an increased fall in velocity after break up of the cloud (Fig. 21), hence is break-up occurs earlier the resulting a_{crit} will also be lower. However, considering that break-up times in the vicinity of a wall are up to 50 % lower than in the theoretical unbounded fluid [40], it might be justified to neglect the variation in break-up times when computing a_{crit}. Moreover, for the particle numbers considered the variation of break-up time is contained within a bandwidth of approximately 200 (units of non-dimensional time t_c^*) . The maximum error in the settled distance (used to compute a_{crit}) then equal to $0.64V_0$ (the average velocity before break-up according to [52]) multiplied by 200. For a typical case of V_0=15 and d^*_{crit}=10000 (which would correspond with a_{crit}=10 µm), this gives an error of 15 %, which is very limited. For lower values of a_{crit} (i.e. the particles settle a large distance until V_{avg}=$2V_s$, the error is even smaller. Figure 21 shows the mean velocity of particles, pre and post break-up. It can be seen that there is a steady decrease in the velocity of all particles. If we define a_{crit} based on when the mean velocity of all particles becomes smaller than $2V_s$, we get the values shown in Table 2. Note that in this context, the break-up of the cloud is beneficial as it promotes deceleration of the particles.

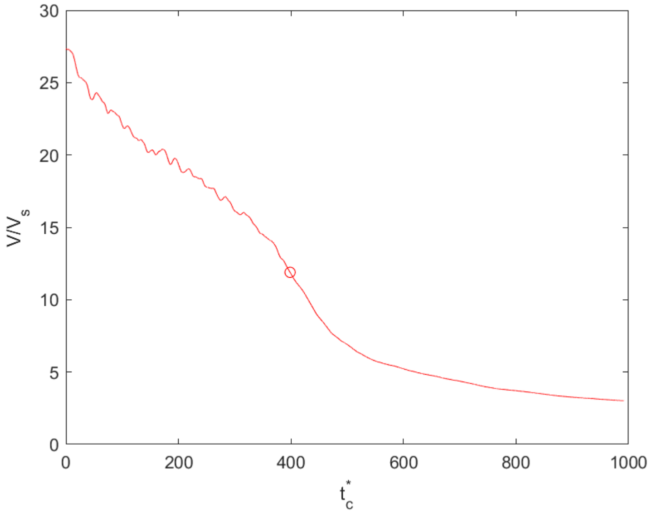

Figure 21: The mean velocity for N_0=1000 and ϕ=0.01. The circle indicates the time of break-up. It can be seen that the velocity of particles falls rapidly during and after break-up. This is due to weakening of the effects of enhanced collective settling, as the cloud breaks up into two particle clouds.

4.6 The velocity distribution

Because the velocity of all particles passing by the camera is measured in the experiment, the velocity distribution is known. From the simulations, it was found (see Fig. 21) that the standard deviation of the non-dimensional particle velocities (plotted in time) follows a predictable trend. It peaks initially, due to leakage of particles that rapidly decelerate, then stays constant for a short time interval, due to simultaneous deceleration of cloud as well as tail particles, and once the cloud velocity drops sufficiently due to sustained leakage of particles or break-up into two clouds, the standard deviation starts dropping and the curve becomes increasingly flatter as particle velocities tend to become more uniformly distributed. Moreover, at the point at which the mean velocity becomes equal to $2V_s$ (marked with a circle), the standard deviation is always close to 0.5 (Fig. 24). This is expected, given that the the minimum velocity of monodisperse particles is equal to $1V_s$ and if the mean is equal to $2V_s$, it follows that the standard deviation (assuming a Gaussian distribution for simplicity) has to be approximately $0.5V_s$. For polydisperse clouds, there will be particles (smaller than the mean) with velocities lower than $1V_s$ - which is also the reason we can not simply take the smallest measured velocity of a single particle and assume that is the representative Stokes velocity of the sample - so the standard deviation will most likely be somewhere in the interval $0.5V_s < S < 1V_s$ when the average velocity is $2V_s$. In reality, the velocities are not always normally distributed around the mean, see figure 22 where the velocity distribution is shown for multiple cases at equally spaced instances with regards to the velocity trajectory, from $V=V_0$ to $V = 2V_s$. Appendix C contains the same plots for multiple simulated clouds, covering a sufficient range of initial cloud velocities. Note that the velocity distribution at t^* is in any case approximately normally distributed around V_0. Then particles leak from the cloud and decelerate to a velocity closer to the Stokes velocity. This can clearly be seen in the first two images.

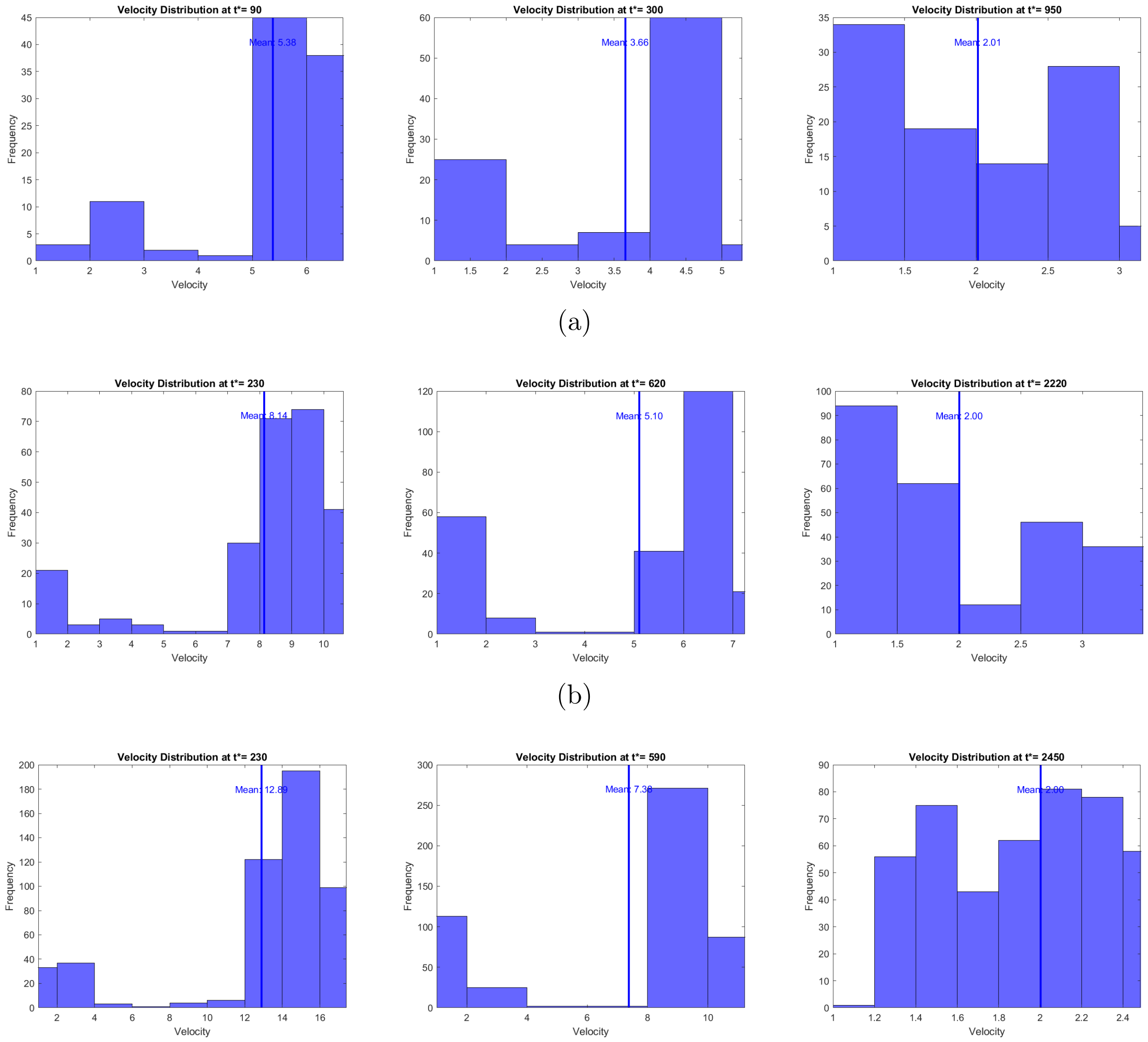

(a)

(b)

(c)

Figure 22: The velocity distribution plotted at several times for (a) N_0=100, $\phi = 1$ % (V_0=6.91), (b) N_0=250, $\phi = 1$ % (V_0=11.32), (c) N_0=500, $\phi = 1$ % (V_0=17.98).The distribution is initially skewed to the right, where most of the particles are in the cloud and moving at enhanced speeds. Because of particle leakage, the amount of particles with velocities close to V_s increases. The final distribution depends on the initial velocity (i.e. on N_0 and ϕ).

As for the distribution at the final time, it seems to be mainly dependent on V_0. If the initial velocity is low, e.g. $2V_s<V_0<4V_s$, the final distribution is qualitatively not very distinct from the distribution at times before it (values of V_0 are given in the figure). There are relatively few tail particles, noticeable from the relatively small frequencies for small velocities. There is somewhat of a gap between the tail particles' velocities and those of the cloud. Then, for higher initial velocities ($4V_s<V_0<12V_s$), the final distribution has a U-shape, where there are is now a significant number of tail particles that have low velocities. Again, there are few particles in between, creating the U shape. Lastly, for higher velocities, $V_0>12V_s$, the final distribution is clearly more evenly distributed around the mean $2V_s$. In some cases, it is left-skewed (right-skewedness being less common) but there are no significant gaps in the distribution. Based on this discussion, it is evident how the velocity distribution can be used - in combination with V_0 (which can be estimated using the approximated N_0 and known ϕ using equation 27) - as a post-hoc measure to evaluate whether the measured settling velocity in the experiment was likely enhanced ($V \gg V_s$) or close to the Stokes velocity. Also, in the case of higher initial velocities, a very clear sign of enhanced settling velocities is a distribution with a clear gap separating the tail particles settling with a speed close to the Stokes velocity from the cloud particles settling at enhanced speeds. Needless to say, it is important that the camera does not measure the initial velocity of particles. Of course, the shape of the distribution will also influence the standard deviation. The discussion above explains why in Fig. 24, S^* at the critical point is equal to 0.5 for N = 500, but for N = 250 the value of S^* at the critical point is 0.7 (the U-shape having a higher standard deviation). Note that the standard deviation plotted is $S^* = S/V_{s,ref}$, where S is the standard deviation of dimensional velocity. This is a quantity not available in experiments, as V_s is unknown. A quantity that can be measured is S/V_{mean}, i.e. the standard deviation divided by the mean velocity (both dimensional). In the simulations, this quantity is equivalent to S^*/V^*_{mean}, as both are divided by the same reference velocity. A plot of this quantity (Fig. 24) reveals that it follows a similar evolution. Following a similar argument, we can say that S^*/V^*_{mean} must be equal to a value between 0.5-1 (depending σ) divided by $V^*_{mean}=2$, hence it must fall somewhere between 0.25-0.50. Looking at the marked points, it can be seen that this is indeed the case. However, because of division by the mean velocity, the range of this value is considerably reduced and the same values are encountered where the settling is highly enhanced.

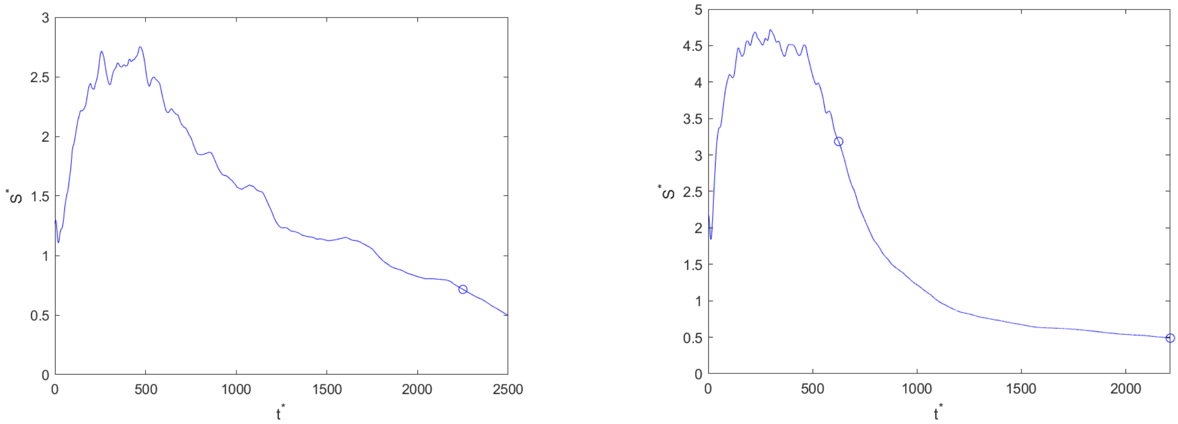

(a) N_0=250

(b) N_0=500

Figure 23: The non-dimensional standard deviation of particle velocities. The circle indicates the moment where the mean velocity becomes equal to $2V_s$. There is a similar trend of S^* for all clouds. In figure b), the moment of cloud break-up is also indicated at t^*=625.

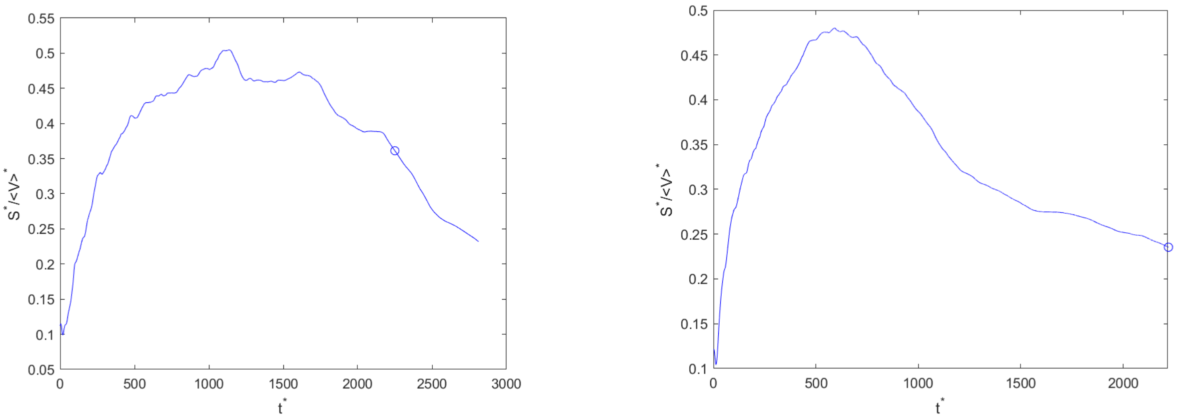

(a) N_0=250

(b) N_0=500

Figure 24: The standard deviation divided by the mean velocity. This would be equal to the dimensional standard deviation divided by the dimensional mean velocity in the experiments. There is a similar trend as with the non-dimensional standard deviation, but due to normalization by the mean velocity the range is much lower.

5 The effect of polydispersity on the settling of the particle cloud

In the current section, we will investigate the effect of polydispersity on the evolution and break-up of a particle cloud. To start, we will only look at polydisperse cloud with a continuous size distribution, after which we will investigate the differences with clouds with a discrete size distribution. Appendix B shows images of settling particle clouds with polydispersity up to σ=0.3 at time of breakup $t_{breakup}$ and half the time of break-up. The polydisperse clouds (with both continuous and discrete PSD) behave very similarly to the monodisperse cloud. There is little qualitative difference, though the break-up event appears more chaotic. Indeed, it was already known from previous studies that the evolution of polydisperse clouds is very similar to that of monodisperse clouds.

5.1 Evolution of a polydisperse cloud

5.1.1 The initial velocity

In the literature, we find two formulas that can be used to calculate the initial velocity of a polydisperse cloud. Bülow et al. derives, based on the H-R formula, the formula (written in non-dimensional form)

$$\frac{V_0}{V_{s,\mathrm{ref}}} = \frac{6}{5}\sum_i \frac{a_i}{a_c}\left(\frac{a_i}{a_{\mathrm{ref}}}\right)^2 \tag{38}$$

and does not include a slip term, whereas Ho et al. proposed

$$\frac{V_0}{V_{\mathrm{s,ref}}} = \frac{1}{N_0}\sum_i \left(\frac{a_i}{a_{\mathrm{ref}}}\right)^2 + \frac{6}{5}\sum_i \frac{a_i}{a_c}\left(\frac{a_i}{a_{\mathrm{ref}}}\right)^2 . \tag{39}$$

Here, the usual slip term (1 in non-dimensional form or V_s in dimensional form) for a monodisperse cloud has been replaced by a term which averages the Stokes velocities of the different sizes particles. Now, these equations require full knowledge of the sizes present in the distribution.

Suppose this is not known, but it is known that the sizes follow a certain type of distribution (e.g. a Gaussian or log-normal distribution) and the standard deviation is also known. Then using the expected value according to the distribution, it is possible to approximate the initial velocity using one of the equations above where the terms involving the sizes, i.e. α_i^2 and α_i^3, are estimated with the expected value. In mathematical terms, $\sum_i \alpha_i^2 = N_0 \cdot \mathbb{E}[\alpha^2]$ and similarly for the third power. Note that the initial cloud radius is calculated using $R_0 = \frac{1}{\phi} \sum_i \alpha_i^3$. Table 3 shows the initial velocities V_0 for the polydisperse clouds that were simulated and the values computed using equations 38 and 39 and the known sizes, or an approximation using the expected value. First, the agreement is best using the slip term (Eq. 39). The approximation of the equation gives surprisingly good results, both for the continuous and the discrete size distributions. Note that to compute $\mathbb{E}[\alpha^n]$, we used the mean and standard deviation after filtering sizes according to the maximum size ratio. The use of the formula for monodisperse clouds (Eq. 27) as an approximation for the polydisperse cloud would result in an error of up to 10 % for the particle numbers considered.

5.1.2 Cloud expansion, deceleration and particle leakage

Figure 25 show plots of R^*, N^* and V^* for different N_0 and polydispersity parameter σ, including the monodisperse case $\sigma = 0$. It is clear that deceleration of the cloud increases with increasing polydispersity. A comparison of all σ from 0 to 0.5 is given in Appendix E (for both continuous and discrete PSD), where this is even more clear. The more rapid fall in velocity is due to increased leakage of particles from the polydisperse cloud.. Moreover, during $t_c^* \lesssim 10$ there is a much stronger phase of initial leakage for polydisperse drops where the cloud can lose up to 20 % of its particles. This may occur because with increasing polydispersity, the difference in individual particles' Stokes velocities becomes larger. Thus, before the toroidal circulation inside the drop (which keeps particles in circulation regardless of difference in size) has been established, this difference in velocities is a driving force for separation. Another argument for this is that after this initial phase, the rate of leakage for different polydispersities is quite similar, up to polydispersities of 40-50 %. Also, figure 38 and Appendix D show that it is mostly small particles that leave the cloud in this initial period, so clearly size plays a role in this effect. The graph of velocity also becomes less oscillatory as σ increases, perhaps indicating the internal circulation inside the drop has a different period, but this needs more investigation. The rate of expansion of the polydisperse cloud increases with the degree of polydispersity, but remains fairly similar. When plotting the relative particle number N^* in log-log, we see that there is still approximately a power law relation between N^* and t_c^*, with a similar exponent (see Fig. 26). To determine accurately if there is a functional relation and what its dependence is on σ, we would need to run a lot of simulations, for different N_0 and σ. Instead, we can assume for simplicity that the correlations are the same as for the monodisperse case and account for the increased leakage rate by changing the coefficient in the equation for N^* (eqn. 30). This adjusted coefficient ranges from 0.65-1.3 (compared to 0.52 for the monodisperse case) when considering values of σ between 0.1-0.4, but is not constant for different particle numbers N_0. Nonetheless,using the extremes, we applied the same analysis as in the monodisperse case. As the rate of expansion is similar, and does not contribute in great terms to the deceleration, the same formula was used. Based on this, it can be predicted that a_{crit} is 1.25-2.5 times as large in the polydisperse case, depending on N_0 and the degree of polydispersity σ.

Initial volume fraction ϕ	Initial number of particles N_0	Polydispersity parameter σ	Initial velocity V_0/V_s	Prediction of V_0/V_s using 38	Prediction of V_0/V_s using 39	Approximation using $\mathbb{E}[\alpha^n]$ without slip term	Approximation using $\mathbb{E}[\alpha^n]$ with slip term	Monodisperse formula
0.01	500	0.2	18.43	17.55	18.59	17.55	18.59	17.29
		0.3	18.45	18.01	19.06	18.10	19.14	
	1000	0.2	28.16	27.01	28.05	27.06	28.10	26.85
		0.3	28.84	27.71	28.76	27.89	28.95	
discrete	1000	0.2	29.65	28.53	29.56	28.55	29.59	
		0.3	30.07	28.83	29.84	28.88	29.89	
0.05	500	0.2	30.14	29.44	30.47	29.46	30.48	28.85
		0.3	30.46	29.96	30.99	30.08	31.10	
	1000	0.2	48.93	48.14	49.18	48.11	49.15	45.21
		0.3	50.60	50.41	51.47	50.56	51.62	

Table 3: The initial velocity for various polydisperse clouds compared against formulas from the literature, and an approximation to these formulas presented in this study.

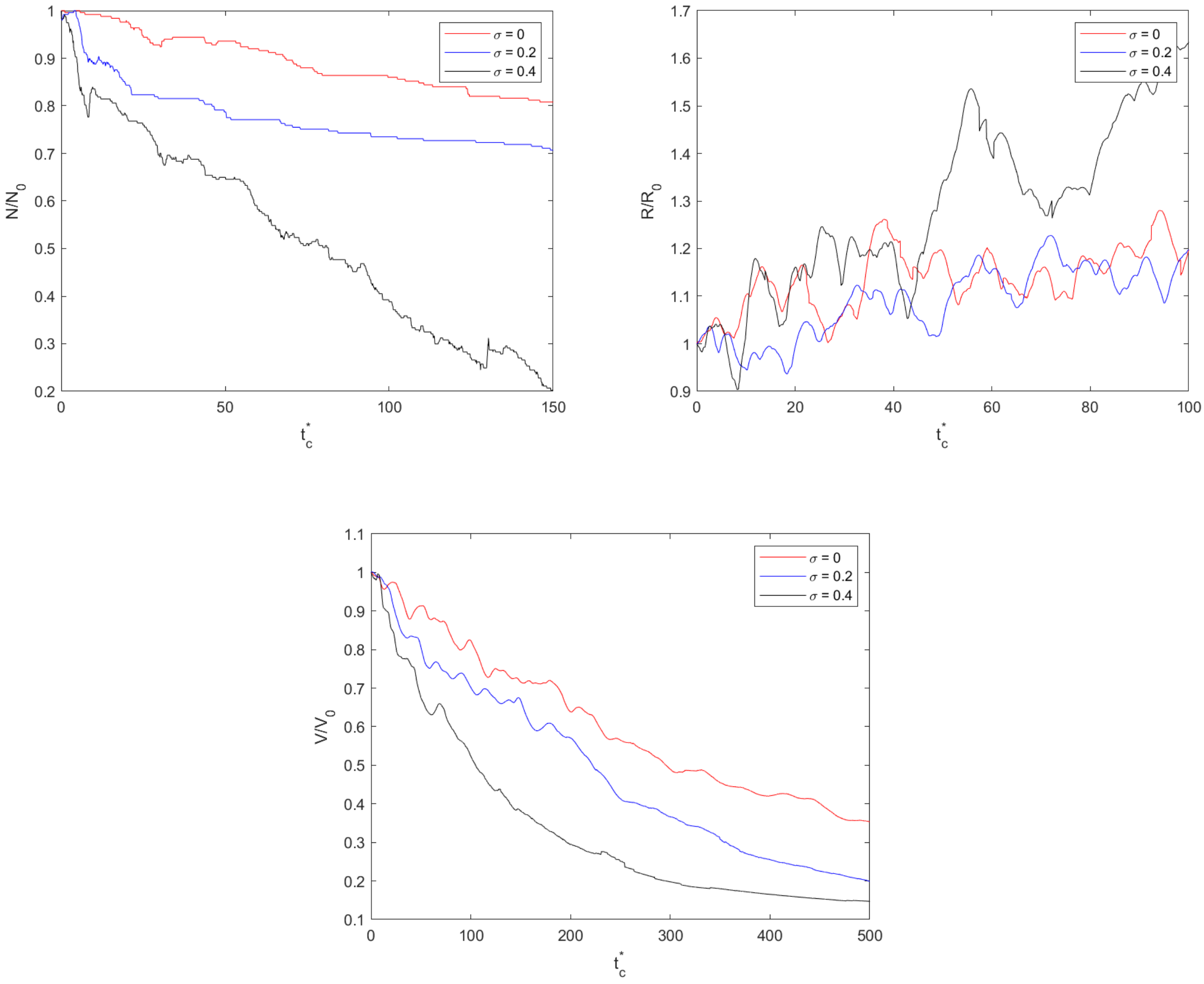

Figure 25: The relative particle number, horizontal radius and velocity of polydisperse clouds compared to the monodisperse cloud (N_0=250). There is a clear increase in leakage rate with the degree of polydispersity, leading to a faster decrease in velocity.

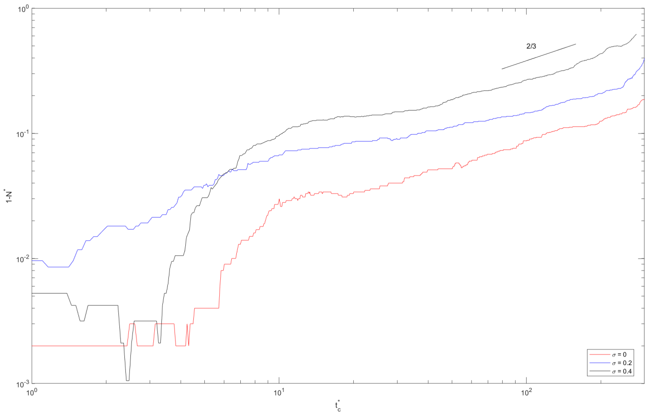

Figure 26: The relative particle number for monodisperse and particle clouds, plotted in log-log. There is only little deviation of the originally observed 2/3 slope for monodisperse clouds.

5.2 The mean velocity

In the previous section, we showed that the mean velocity can provide a good estimate of the average velocity of all particles, both in- and outside the cloud, at a certain position. Figure 27 shows that tail particles originating from a polydisperse cloud also reach some steady state, but now the velocities are contained within a band, because the different size particles are tending to their respective Stokes velocity, which is in the range of the square of the sizes, e.g. 0 to 4 for sizes between 0 and 2 but smaller for less polydisperse drops. Similar to the monodisperse case, the only particles in the tail with significantly higher velocities are ones that just exited the cloud a short time before measurement. Hence, it is expected that the mean velocity is again a good indicator of the measured average velocity. We will find values of a_{crit} for polydisperse clouds using the mean velocity. Simulations were performed for clouds comprising of 100-1000 particles and volume fractions of 0.01 and 0.05. Figure 28 shows the cloud velocity, as well as the mean velocity. Again, the mean velocity is lower, because of the slower moving tail particles. For $\sigma = 0.4$, we see that there is a larger difference between the cloud velocity and the mean velocity. This can be attributed to the larger leakage rate for higher σ, but also to the fact that the leaking particles' average size is smaller (Fig. 39). These particles will slow down until they reach a speed close to their Stokes velocity, which will be very small relative to the speed of the cloud. Values of $\langle a \rangle_{crit}$ based on the mean velocity are shown in Tables 4 - 5 for different standard deviation. The prediction that values would are up to 2.5 times as high as in the monodisperse case is confirmed. Hence, suspension drops that are polydisperse reach $2V_s$ faster and because of that, we can allow for higher (mean) particle sizes in the experiment and/or higher particle number N_0. Finally, similar to monodisperse drops, it seems to be the case that at high volume fractions ($\phi > 0.05$) in combination with higher particle number (N_0>500), the increase of a_{crit} with the volume fraction comes to a halt or may even reverse.

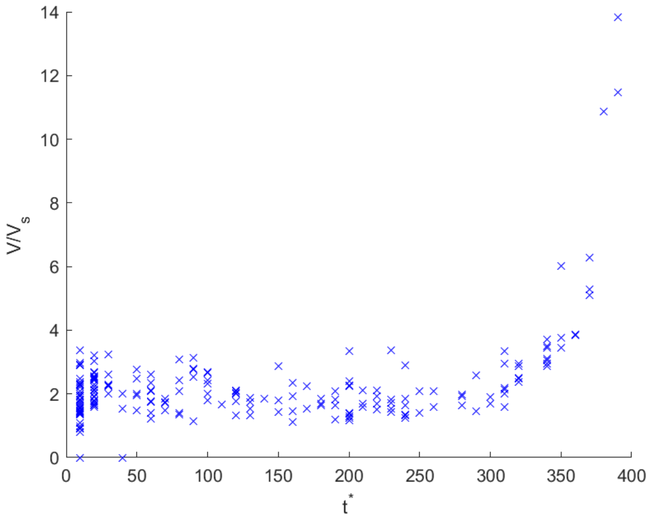

Figure 27: The crosses are the velocities of tail particles at time t^*=400. The horizontal coordinate t^* is the time at which the respective particle leaked from the cloud. The tail particles' velocities are contained within a band because of polydispersity. The simulation was of a polydisperse cloud with N_0=1000, ϕ=1% and σ=0.2.

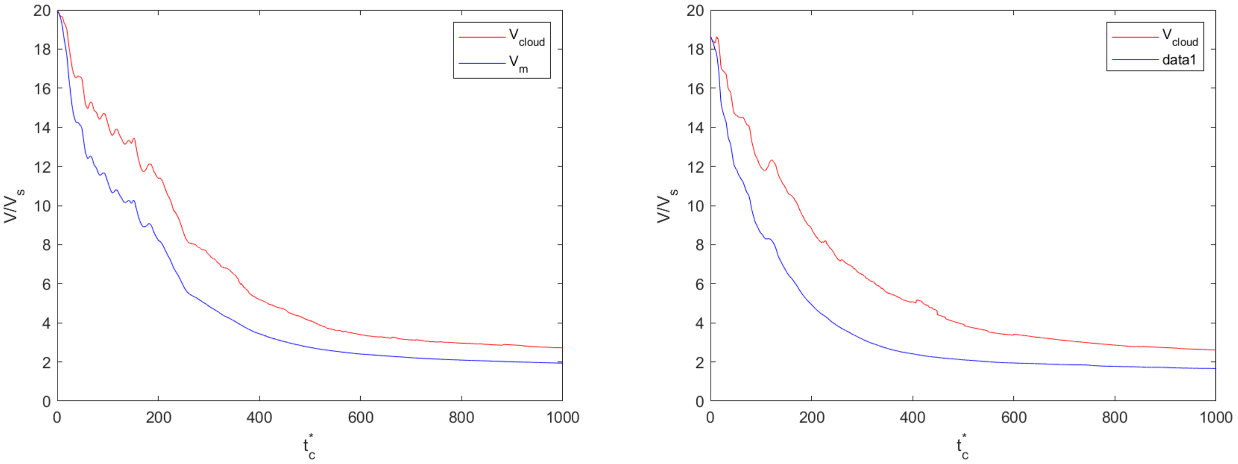

(a) N$_0$=250, σ=0.2 (b) N$_0$=250, σ=0.4

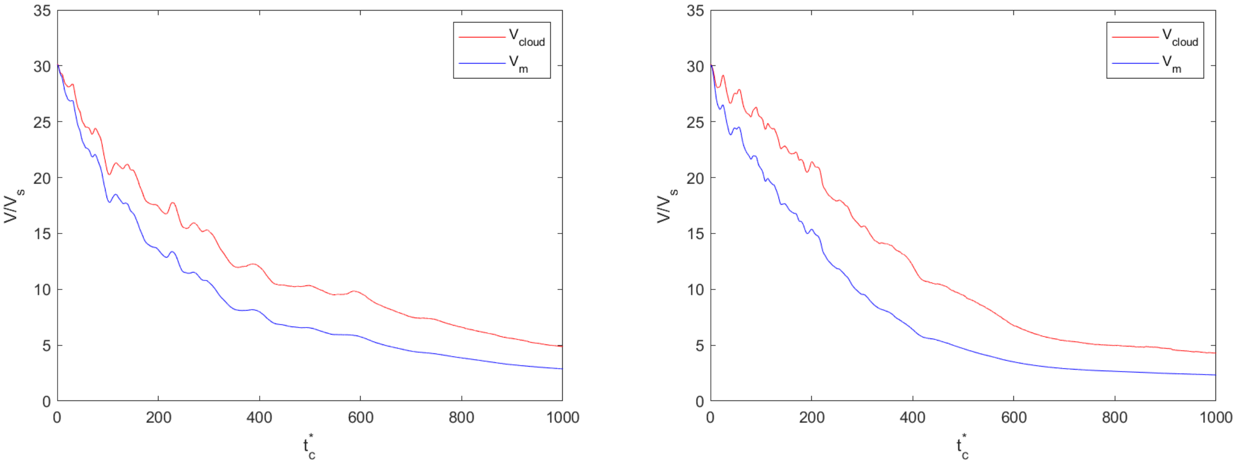

(c) N$_0$=500, σ=0.2 (d) N$_0$=500, σ=0.4

Figure 28: The mean velocity of all particles compared to the velocity of the cloud, for two different N$_0$ and σ. There is a larger difference between the curves for σ=0.4, which can be explained by considering that there is more leakage of small particles, which have lower Stokes velocities. See figure 38.

N_0	1%	5%
100	420	500
250	170	180
500	74	90
750	49	53
1000	45	40

Table 4: $\langle a \rangle_{crit}$ for $\sigma = 0.2$

N_0	1%	5%
100	640	440
250	210	240
500	130	100
750	68	64
1000	58	45

Table 5: $\langle a \rangle_{crit}$ for $\sigma = 0.4$

5.3 The size-velocity relationship

In the polydisperse case, what is desired is that each particle settles at or close to the velocity corresponding to its Stokes velocity. This is not simply guaranteed by waiting until V$_{avg}$=2V$_{s,ref}$. Therefore, we need to look at the velocity of all particles with respect to their size. Figure 29 shows the evolution of the cloud and tail particles' velocities for all sizes present.

Clearly, cloud particles move at a uniform velocity regardless of size. The velocity of tail particles is initially somewhat undifferentiated with respect to size. This may also explain why in the study of Waqas, the 'tail' particles (particles that pass by the camera some time after the first particles) have lower velocities but the velocity does not show a dependence on size [7]. Then, tail particles increasingly decelerate towards the Stokes velocity line (given by $y = x^2$) and the velocity-size relation becomes increasingly evident. The amount of tail particles also increases due to particle leakage and for the same reason, the cloud velocity decreases.

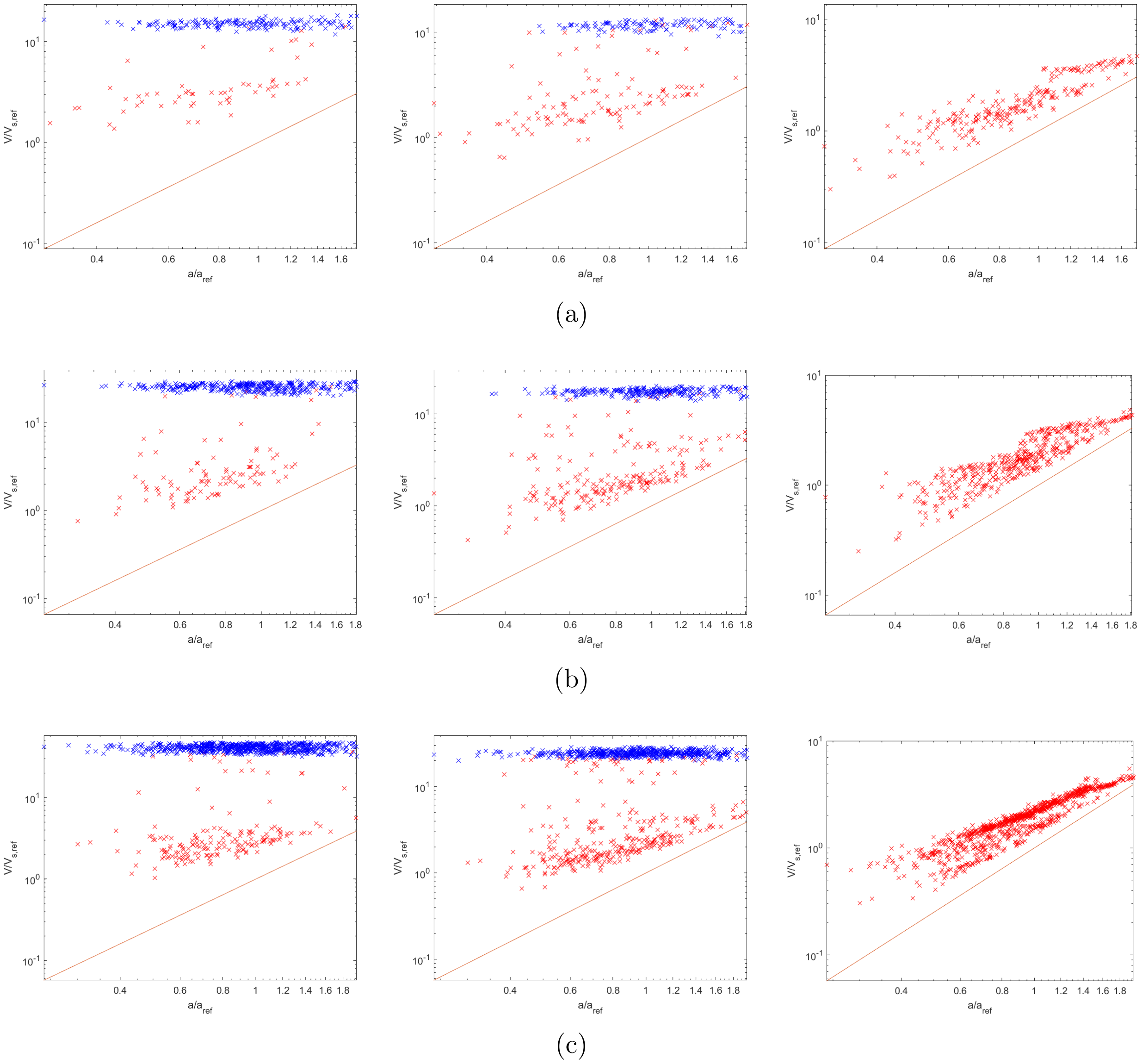

(a)

(b)

(c)

Figure 29: The velocity plotted against size at several times for (a) $N_0 = 250$, (b) 500 and (c) 1000, $\phi = 0.05$ and $\sigma = 0.4$. Blue indicates cloud particles and red indicates tail particles. The red line is the Stokes velocity. Size is relative to the mean. The plots on the right are at the time where V_{avg}=2$V_{s,ref}$. The other two plots are at times where the average velocity is equal to $\frac{2}{3}(V_0 - 2) + 2$ and $\frac{1}{3}(V_0 - 2) + 2$, respectively.

Note that at the final time, the cloud had fully desintegrated, therefore all points are plotted in red. Also note that with the convention used here for the critical size (based on the mean velocity), slower moving particles will undergo additional deceleration before the moment of measurement, so we expect the final curve to tend more to the Stokes line. Nonetheless, based

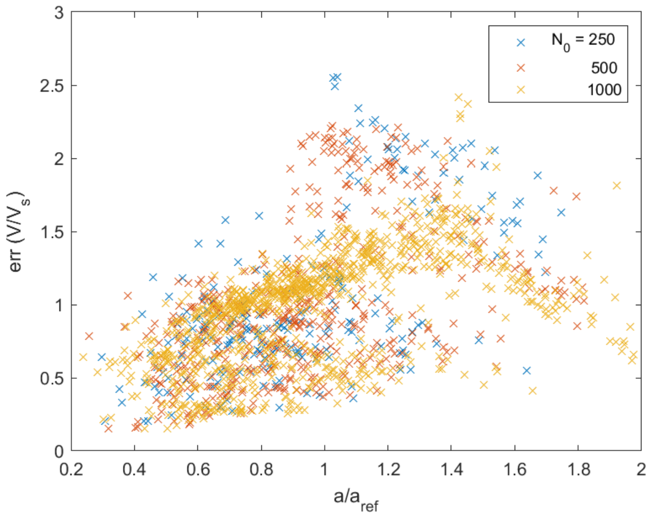

Figure 30: The difference between the actual particle velocity and the particle Stokes velocity at the time where the average velocity of particles is equal to 2 times the reference Stokes velocity. For several N_0 and $\phi = 0.05$.

.

on these results we can calculate the maximum error that will be made in determining the Stokes velocity as a function of the size, with the current convention for a_{crit} (mean particle size). See Figure 30, that shows the error for different sizes, i.e. the distance between the points and the Stokes line in Figure 29. It is evident that the error is less for sizes that are small relative to the mean. This is expected, as small particles have a greater tendency for leaking from the cloud and so have a longer time to decelerate. The spread is large, but if there are enough particles per size fraction the expected error is between 50 and 75 %, if the size is small relative to the mean. For larger sizes, the spread is larger. The expected error is upwards of 100 %. It seems that the error may actually be highest for the mean size. We expect this has to do with the size distribution and the fact that the mean size is also the (approximate) mode of the distribution, but this needs to be studied more.

5.4 Low volume fractions

Polydisperse clouds at low volume fractions deviate from the standard particle cloud behavior. The average velocity starts around the predicted V_0, whereafter particles start separating according to their size. As a result, the cloud instantly loses its shape. There is also no toroidal circulation. Note that the equivalent monodisperse cloud (same N_0 and ϕ) will undergo the standard particle cloud evolution. The polydispersity presents a disturbance large enough to cause deviation from the usual behavior. Figure 31 shows an image of a very dilute particle cloud at t_c^*=5. This type of behaviour occured for all clouds with ϕ of 0.001 and 0.01 %. For ϕ = 0.1 %, it occured for low particle numbers N_0<250, and clouds with higher N_0 showed typical cloud behavior. Thus, the transition to this different settling behavior seems to be dependent on both the particle number and the volume fraction. As a result of the particles quickly separating according to their size, the particles will settle with a velocity determined by their size and interactions with neighbouring particles and not with the 'cloud' velocity. Due to this, the average velocity will drop much faster. The resulting values of a_{crit} are therefore also higher than what is presented both in Tables 1 and 2. Moreover, a_{crit} increases with decreasing volume fraction in this regime. This is because the initial velocity is lower and since the velocity drop

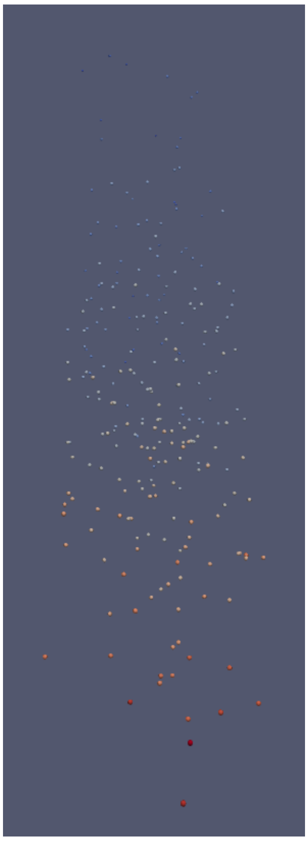

Figure 31: An image of a particle cloud with N_0=250, $\phi = 0.001$ % and σ=0.2 at t_c^*=5. Particles are enlarged by factor 10 for visualization.

is not anymore determined by leakage of particles from the cloud but by size-based separation, the average velocity reaches 2V_s faster. These results are shown in Table 7 for σ 0.2 and 0.4. We now see a significant departure from the monodisperse data, not only in magnitude but also in dependence on ϕ, due to the aforementioned phenomenon. It is very important to note that the higher a_{crit} values at these very low volume fractions are only relevant for very large drops. For example, a drop with N_0=500, ϕ=0.01 % and with 100 µm particles, has volume 21 mL (3.4 cm diameter). Finally, we also see that with increasing polydispersity and a sufficient amount of particles, the separation occurs faster. Such a result is expected. Figure 32 shows the velocity against the particle size. Here, we can see there is a clear size dependence of velocity from the start.

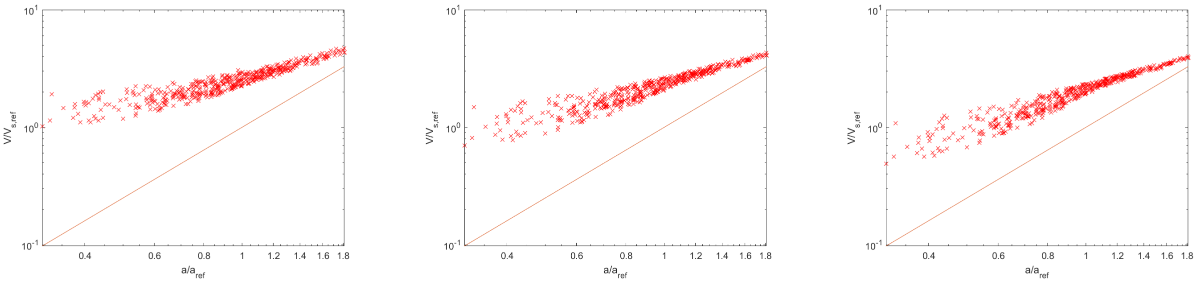

Figure 32: The velocity plotted against size at several times for $N_0 = 500$ $\phi = 0.00001$ and $\sigma = 0.4$. The red line is the Stokes velocity. Size is relative to the mean. The plot on the right are at the time where V_{avg}=2$V_{s,ref}$. The other two plots are at times where the average velocity is equal to $\frac{2}{3}(V_0 - 2) + 2$ and $\frac{1}{3}(V_0 - 2) + 2$, respectively.

N_0	0.001%	0.01%	0.1%
100	-	1100	600
250	680	230	180
500	130	100	80
750	70	65	50
1000	50	41	38

Table 6: $\langle a \rangle_{crit}$ for $\sigma = 0.2$

N_0	0.001%	0.01%	0.1%
100	-	1100	580
250	900	370	280
500	210	140	130
750	120	86	76
1000	77	75	60

Table 7: $\langle a \rangle_{crit}$ for $\sigma = 0.4$

5.5 Velocity distribution

For monodisperse clouds, we discussed the use of the velocity distribution of particles. We noted that in the polydisperse case, we expected the non-dimensional standard deviation S* to be higher at the time where V=2V$_s$, as well as increasing with σ. Figures 33 and 34 show that this is indeed the case. As for the shape of the distribution, what needs to be considered is that the individual particles' Stokes velocities are not 1V$_s$ but in a range determined by the size range. The velocity distribution will also reflect this. Nonetheless, looking at the velocity distributions at multiple times for different polydisperse drops (see Appendix C), we can draw similar conclusions, e.g. for high V$_0$ the final distribution is expected to look uniform and a clear sign of enhanced velocities is a gap separating slow tail particles from fast cloud particles.

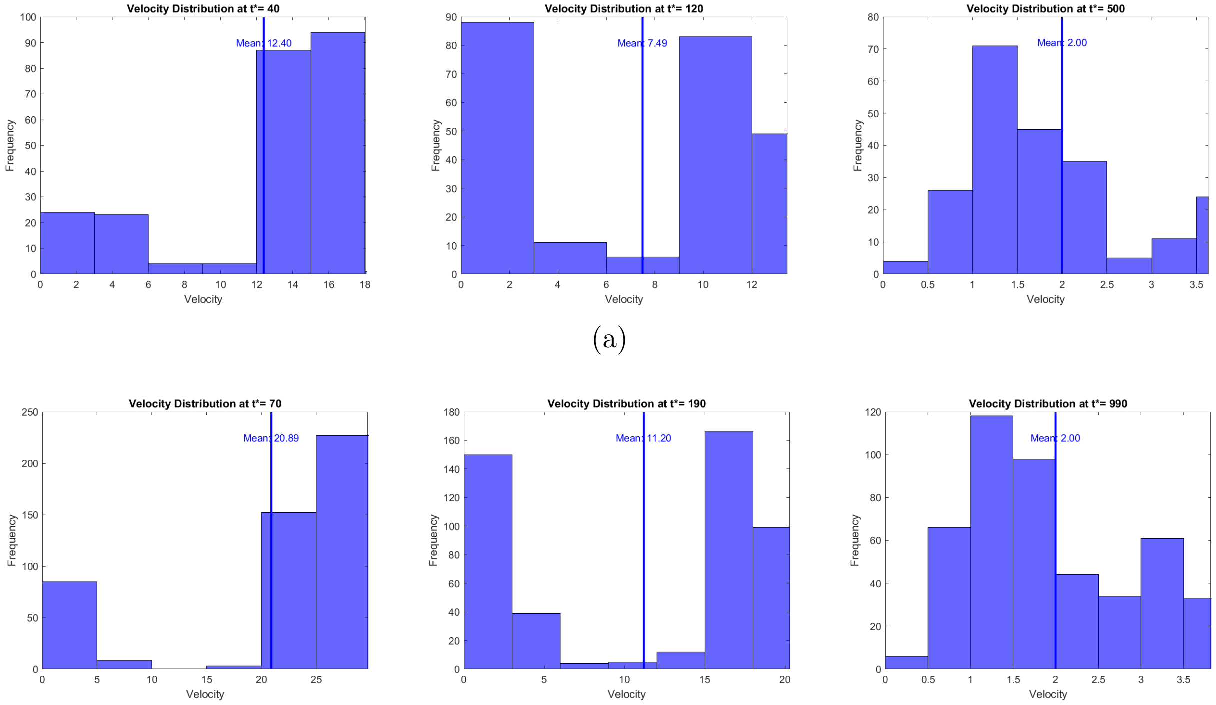

(a)

(b)

Figure 33: The velocity distribution plotted at several times for (a) N$_0$=250, ϕ = 5%, σ=0.4 (V$_0$=18.69), (b) N$_0$=500, ϕ=5%, σ=0.4 (V$_0$=30.11). Due to the presence of more sizes, the spread in the velocity is larger.

For drops with discrete size distributions, we do not expect much differences with regards to the expected distribution. Particles do not decelerate to precisely their Stokes velocity because of hydrodynamic interactions with neighbouring particles (this also leads to the distribution in the monodisperse case). Therefore, the final velocity distribution is not expected to reflect exactly the size distribution (in being discrete or continuous). The particle clouds with discrete PSD that were simulated are shown in Fig. C.19-C.20. Note that the cloud with σ=0.2 contains 11 distinct sizes and the cloud with σ=0.4 contains 18 different sizes. We know that in the limit of discrete size distributions, the behaviour of a bidisperse cloud is significantly different from monodisperse as well as fully polydisperse clouds. Therefore, it might well be the case that a cloud with less and discrete sizes - tridisperse, tetradisperse and so on - will not follow the same pattern and the velocity distributions would look different. When plotting $\mathrm{S}^*/\mathrm{V}^*_{mean}$, we see that the interval in which the value of $\mathrm{S}^*/\mathrm{V}^*_{mean}$ would result in a false positive is much smaller than the monodisperse case. This is probably due to the larger leakage rate, causing the standard deviation to climb quickly and the mean velocity to decrease quickly. However, there is no obvious a priori choice of a target value for this quantity and how that value would depend on the properties of the suspension drop. At this point, we can only speculate that it is in the range of [0.25, 0.5] for polydisperse drops and increases with the polydispersity.

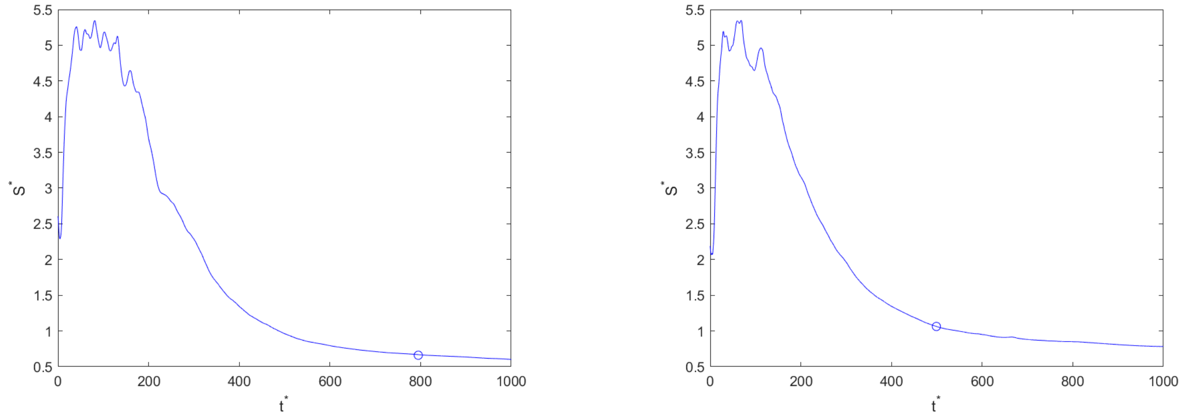

(a) σ=0.2

(b) σ=0.4

Figure 34: The non-dimensional standard deviation of velocity plotted for two different degrees of polydispersity and N_0=250. In line with our expectation, the standard deviation at the critical point is higher when the drop is more polydisperse.

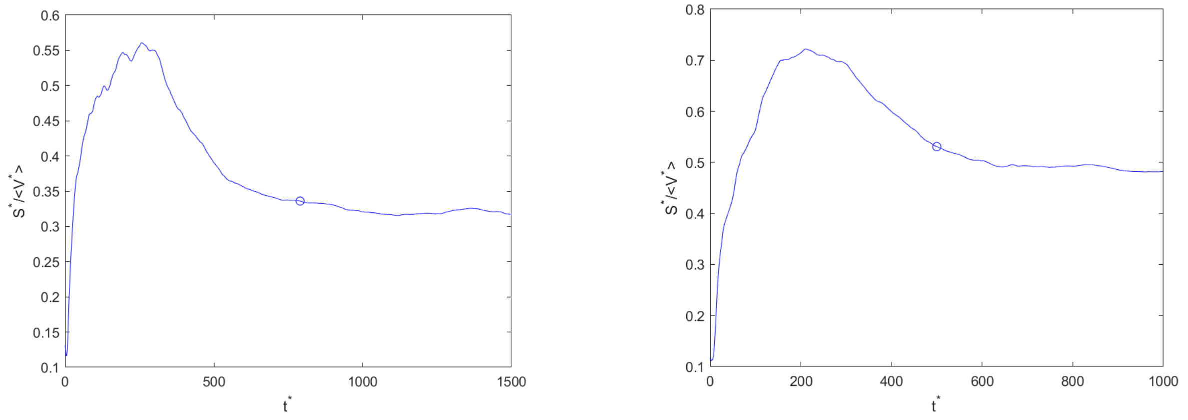

(a) σ=0.2

(b) σ=0.4

Figure 35: The dimensional standard deviation of particle velocities

5.6 Stability of the polydisperse cloud

It is known that polydisperse clouds break up earlier than monodisperse ones (assuming N_0 is sufficiently high). If we compare the times $t^*_{c,des}$ at which destabilization occurs (Fig. 36) with the results presented by Ho et al. [52], we obtain similar results, where the times where determined visually by comparing the cloud to images at break-up time in their study. As for the relation between the breakup time $t^*_{c,des}$ and length $L^*_{c,des}$ (the distance travelled until break-up), the points seem to deviate more from the line of Ho et al. as σ increases (Fig. 37), though this may simple be due to an error in the determination of the break-up times. For the cases where σ is equal to 0.4 or 0.5, the particle cloud most of the time did not break-up into distinct clouds but slowly desintegrated. Images of this are shown in Appendix B (Fig. B.1-B.2). Note that in these clouds, the largest size ratio present in the cloud is $2/0.2 = 10$, which means that the ratio of their Stokes velocities is equal to 100. It might be that this difference in size causes separation before formation of new circulatory flow regimes that can support multiple drops. This does not mean that break-up into two clouds never occurs, see e.g. B.10. Ho et al. found that the variance in $t^*_{c,des}$ and $L^*_{c,des}$ decreases with increasing polydispersity, which means the values we found of a_{crit} are less dependent on the precise time of break-up. Note that while the volume fraction does not influence the value of $t^*_{c,des}$ due to non-dimensionalization by the cloud radius and velocity [52], the actual time of break-up t_{des} is strongly dependent on the volume fraction as more dense suspension drops lose particles and destabilize more quickly. Ho et al. proposed the relation $t_{des} = C\phi^{-1}$ where the constant C depends on all other parameters (cloud radius and fluid and particle properties).

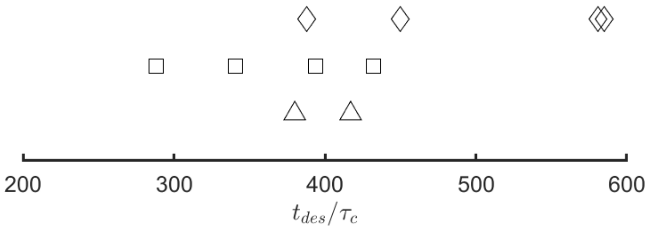

Figure 36: Destabilization time of monodisperse and polydisperse clouds. Triangle for monodisperse, square for polydisperse with continuous size distribution and diamond for discrete size distribution. The values of $t^*_{c,des}$ are 394 and 581 for σ=0.05, 432 and 585 for σ=0.1, 288 and 450 for $\sigma = 0.2$ and 341 and 388 for $\sigma = 0.3$.

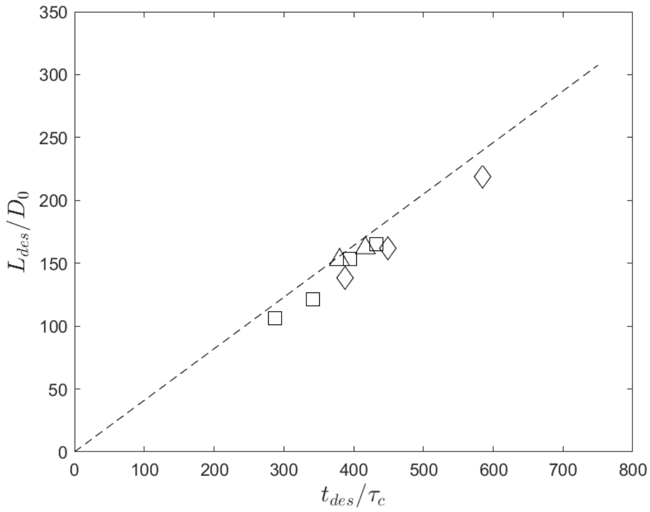

Figure 37: The destabilization lengths and times. Here, the length is non-dimensionalized by the initial cloud diameter. The values deviate slightly from the relation found by Ho et al. [52], which can probably be explained by a slight error in the destabilization times as they were determined visually.

5.7 Particle segregation

Faletra et al. [51] studied the segregation between different size particles in bidisperse particle clouds. The main finding was that small (or light) particles separate from large (or heavy) particles during sedimentation of a particle cloud, and the degree of separation is dependent on the particle number, decreasing when N_0 is increased. Bülow et al. [50] also studies separation in bidisperse clouds, concluding that as the size ratio is increased, separation of the two particle fractions increases. We found for polydisperse clouds that the rate of leakage of a particle depends on its size relative to the mean, with smaller particles leaving the cloud at a faster rate. To visualize this, the particles were divided into size classes. Figure 38 shows the percentage of particles remaining in the cloud per size class. It is evident that segregation of particles according to size becomes more prevalent as σ increases, where there seems to be a sudden jump in the rate of segregation as the polydispersity parameter is increased from 0.2 to 0.3. Appendix D contains plots of relative particle number per size class for clouds of different N_0 and σ. The results are consistent, showing that for a polydispersity degree of 10-20 %, the segregation of different size particles is not pronounced. For higher σ, there is significantly more segregation of smaller particles into the tail, the effect becoming stronger as polydispersity degree increases. In contrast to what was seen in bidisperse clouds [50, 51], there seems to be no effect of N_0 on these segregation effects in fully polydisperse clouds (see Fig. D.1-D.2). Figure 39 shows the distribution of particle sizes in the cloud and in the tail, comparing that to the initial distribution. It can be seen that as time grows, the distribution in the cloud becomes more skewed towards larger sizes and that in the tail is skewed towards smaller sizes.

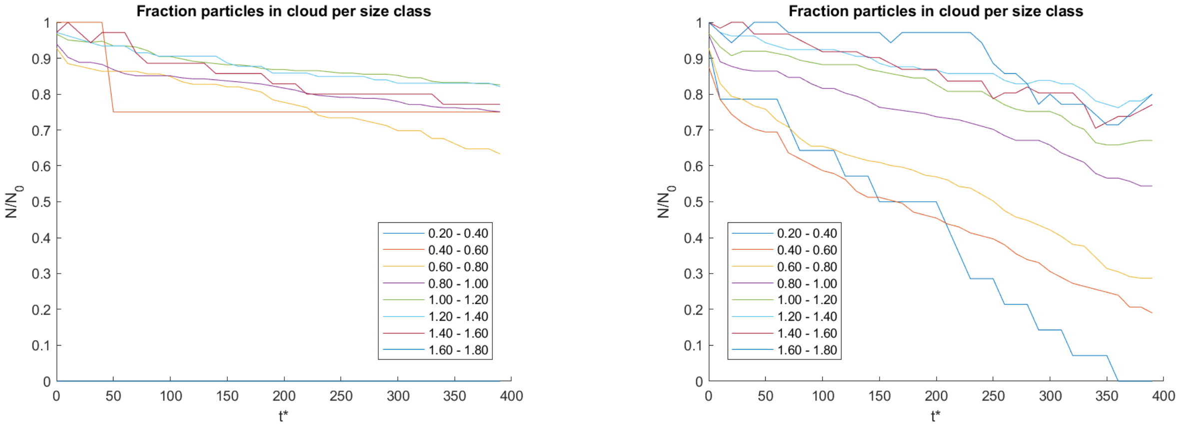

(a) σ=0.2 (b) σ=0.4

Figure 38: The percentage of particles in the cloud belonging to different size classes (size is relative to the mean). There is a preferential leakage of small particles. This effect becomes much more pronounced for larger standard deviations, and is similar for $\sigma = 0.3$ and σ=0.4.

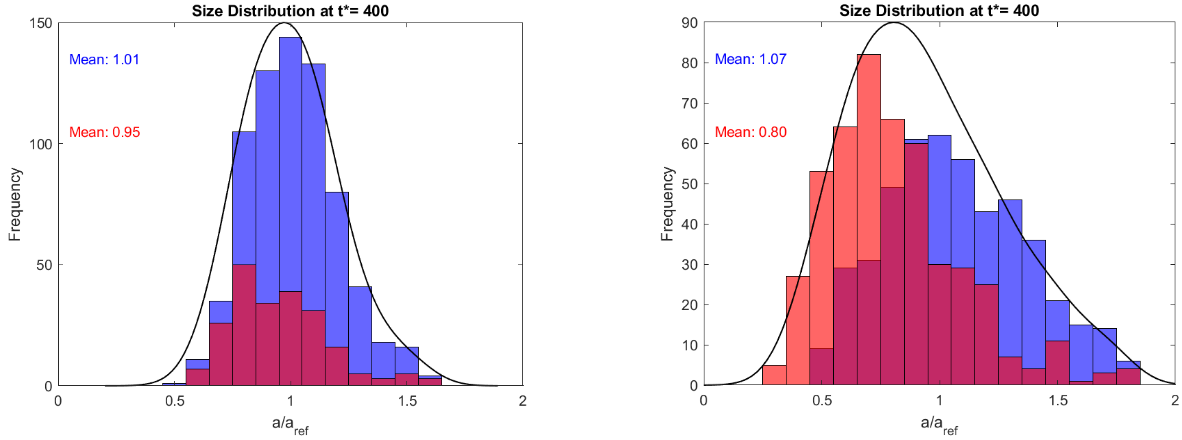

(a) $\sigma = 0.2$ (b) $\sigma = 0.4$

Figure 39: The size distribution of two polydisperse particle clouds (N$_0$=1000) a moment before break-up. The initial distribution of sizes inside the cloud is shown as a probability density function (PDF), but rescaled so that it is visible (the black curve). Sizes of particles belonging to the cloud are shown in blue and sizes of tail particles in red. Not only is there more overall particle leakage for a greater σ, the size distribution in the tail is significantly more skewed to smaller sizes.

5.8 Comparison of continuous and discrete particle size distributions

We performed all different types of analysis mentioned in this study for particle clouds with discretized size distributions, for N$_0$=1000, $\phi = 1$ %, and polydispersity parameter σ from 0.1 to 0.5. Overall, there were not any noteworthy differences. Judging from Fig. 36, one would get the impression that particle clouds with discrete particle size distributions break up at a later time. However, looking at Fig. E.6, we see that the rates of leakage are very similar for the two types of clouds. Considering that the loss of particles and the subsequent evolution into a torus are the factors leading to break-up, it would be premature to ascribe the difference in break-up time to the (continuous or discrete) size distribution. It could be that the fact that the discrete clouds contain groups of identical sizes has a stabilizing effect on the cloud, but this needs further investigation. As for preferential leakage or segregation of different particle sizes, the results from the simulation indicate no significant difference with the continuous case (see Fig. D.8-D.12). This is an important finding, as most numerical research on particle clouds involved the use of discrete particle size distributions, hereby extending the validity of those findings to particle clouds with continuous size distributions. Figures 40 - 41 show the size-dependent velocity (in time) and (mean) error. Results are similar as for the continuous case. For the discrete case, it is easier to obtain statistics. We see that the average error is relatively low for small sizes and increases with size, with a maximum at 1.4 times the size of the mean, and decreasing error as particle size increases. We expect that this has to do with the distribution, as there is a small amount of very large particles and so a smaller chance that it has neighbouring particles.

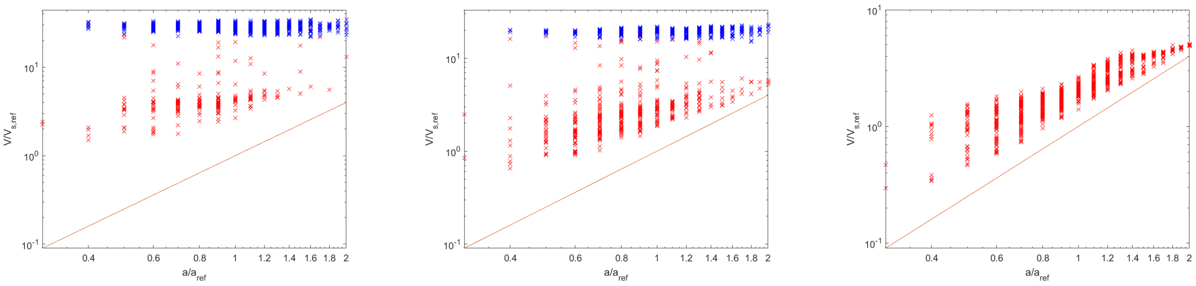

Figure 40: The velocity plotted against size at several times for $N_0 = 1000$ $\phi = 0.01$ and $\sigma = 0.4$ for the cloud with discrete PSD. Blue indicates cloud particles and red indicates tail particles. The red line is the Stokes velocity. Size is relative to the mean. The plots on the right are at the time where V_{avg}=2$V_{s,ref}$. The other two plots are at times where the average velocity is equal to $\frac{2}{3}(V_0 - 2) + 2$ and $\frac{1}{3}(V_0 - 2) + 2$, respectively.

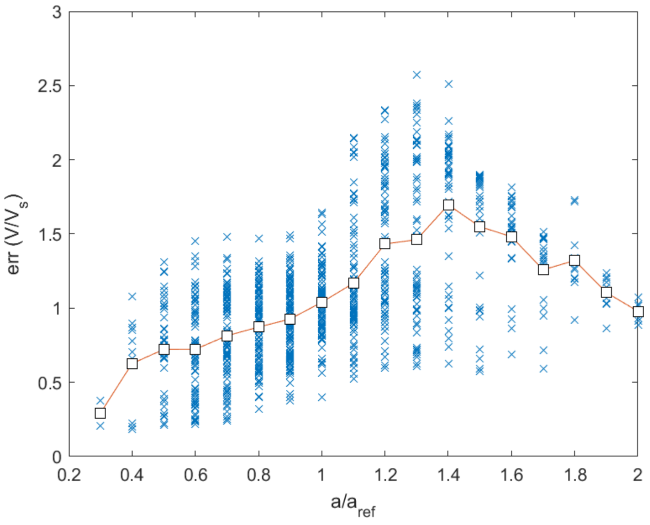

Figure 41: The difference between the actual particle velocity and the particle Stokes velocity at the time where the average velocity of particles is equal to 2 times the reference Stokes velocity. For N_0=1000 and $\phi = 0.01$ and discrete PSD. The boxes indicate the mean error.

.

6 Conclusion and recommendations

6.1 Summary and conclusions

The current thesis investigated the validity of measuring the Stokes velocity of particles by means of measuring the speed of particles in a suspension drop that is made to settle in a tank, as well as the effects of polydispersity on this. To this end, simulations were performed for suspension drops with varying number of particles, volume fraction and degrees of polydispersity. The velocity of the drop, depending on the number of particles and the volume fraction, decreases during settling due to leakage of particles from the cloud. In turn, the rate of leakage depends on the velocity of the drop as well as the distance between particles. Though increasing the volume fraction will increase the initial velocity of the cloud, it will lose particles more quickly and therefore decelerate faster than the more dilute drop. This theoretical prediction was confirmed in the simulations. Because the initial velocity of the cloud is highly dependant on the number of particles, it is important to make a rough estimation beforehand, for which we presented two approaches from the literature.

When particles leak from the cloud, they decelerate from the cloud velocity to a velocity that is close to their respective Stokes velocity. As these particles settle at a far lower speed than the cloud, it is important to consider the effect this has on the average velocity measured in the experiment. We presented a simple model that can take this deviation into account, which predicts that it leads to a 30-40 % increase in the upper limit of (mean) particle size $\langle a \rangle_{\text{crit}}$ for which the experiment leads to a measurement of 2 times the Stokes velocity. We also showed how the mean velocity of all particles (in the simulation) can give a good estimation of the mean velocity measured in experiments. Using the mean velocity, more conservative results were found but there is qualitative agreement with the theoretical prediction. Finally, we showed how the distribution of velocity of particles can aid in determining whether the settling is enhanced ($V \gg V_s$) or closer to the Stokes velocity, and that the standard deviation of non dimensional velocities follow a predictable trend during settling of the cloud. The latter was compared to a quantity than can be measured in simulations (dimensional standard deviation divided by the mean of velocity) which follows a similar trend, but its range is considerably decreased.

A polydisperse cloud usually settles (depending on the size distribution) at a higher velocity, due to the quadratic dependence of velocity on the size. We compared the initial speed of polydisperse clouds from simulations to two formulas derived from the literature, and showed that the speed can be accurately estimated using the expected value of the size distribution. Moreover, a polydisperse cloud loses particles faster and hence its speed also drops faster. Based on the increased leakage rate and using the same theoretical model as for the monodisperse clouds, we first made a theoretical prediction that $\langle a \rangle_{\text{crit}}$ could be up to 2.5 times as large for polydisperse clouds, depending on the degree of polydispersity. The values found using the mean velocity from the simulations agree with this prediction. Again, the shape of the velocity distribution was also shown to be a useful success indicator for polydisperse drops. For polydisperse clouds, the proposed quantity S/V_{mean} seems to be a more reliable indicator of whether the velocity is sufficiently close to the Stokes velocity, but comparison with experimental data is necessary.

The polydisperse cloud also breaks up significantly earlier, which is due to the increased leakage rate. For the most part, the results found for break up times and lengths fall in line with previous findings from the literature. We also found that when the polydispersity exceeds 30 %, the cloud will have a tendency not to break up into two clouds but to lose particles until it desintegrates and the collective settling behaviour disappears, similar to monodisperse clouds with low particle numbers. This is very interesting, as monodisperse clouds with the same number of particles always break up. Another finding from the literature was corroborated, namely that there is preferential leakage of smaller particles. This is consistent for all degrees of polydispersity, but there is a significant jump at 30 % where particles with small size relative to the mean will almost completely vanish from the cloud after some time. This also leads to a more rapid fall in the mean velocity (of all particles), because the small particles will decelerate from the velocity of the cloud to their Stokes velocity, which is comparatively very low. In contrast to the literature (which studies bidisperse clouds), the effects of particle segregation were not dependent on the number of particles in the drop. These findings indicate that a polydisperse suspension drop is preferable, as it will lead (all else being equal) to a velocity measurement closer to the Stokes velocity, in the case we are interested in the Stokes velocity belonging to the mean size of the sample. If we want to measure the Stokes velocity for each size in the sample (like in the floc experiments), the approach in this study (see below for details) will introduce a variable error, the velocity for smaller sizes being most accurate because of early leakage. Finally, no significant results were found with regards to the difference between polydisperse particle clouds with continuous vs. discrete size distributions.

For volume fractions between 0.01 and 1 %, the values for the maximum allowable size a_{crit} for the monodisperse cloud approximately follow a power law (w.r.t. volume fraction and particle number) and are well represented by the following equations with a_{crit} in micrometers and h_{tank} in meters:

$$a_{crit} = h_{\text{tank}} \exp(7.059\phi^{-0.05}) N_0^{-0.4753\phi^{-0.1247}}, \tag{40}$$

with separate equations for $\phi = 0.001$ % and $\phi = 5$ %:

$$a_{crit} = h_{\text{tank}} e^{20.59} N_0^{-2.8023} \quad (\varphi = 0.001\%) \tag{41}$$

$$a_{crit} = h_{\text{tank}} e^{9.9410} N_0^{-0.9170} \quad (\varphi = 5\%) \tag{42}$$

The same is true for the values of maximum mean size $\langle a \rangle_{crit}$ of polydisperse clouds, the data for σ=0.2 being well represented by

$$\langle a \rangle_{crit} = h_{\text{tank}} \exp(8.612\phi^{-0.0471}) N_0^{-0.746\phi^{-0.0682}} \tag{43}$$

for volume fractions between 0.01 and 1 %, and

$$\langle a \rangle_{crit} = h_{\text{tank}} e^{16.94} N_0^{-1.908} \quad (\varphi = 0.001\%) \tag{44}$$

$$\langle a \rangle_{crit} = h_{\text{tank}} e^{11.27} N_0^{-1.098} \quad (\varphi = 5\%) \tag{45}$$

for lower and higher volume fractions. Finally, for $\sigma = 0.4$, the data is closely approximated using

$$\langle a \rangle_{crit} = h_{\text{tank}} \exp(5.97\phi^{-0.0862}) N_0^{-0.422\phi^{-0.1218}} \tag{46}$$

for volume fractions between 0.001 and 0.1 %. For higher volume fractions:

$$\langle a \rangle_{crit} = h_{\text{tank}} e^{11.22} N_0^{-1.0424} \quad (\varphi = 1\%) \tag{47}$$

$$\langle a \rangle_{crit} = h_{\text{tank}} e^{10.86} N_0^{-1.0094} \quad (\varphi = 5\%) \tag{48}$$

The workflow we suggest for the suspension drop settling experiments is:

- Measure or estimate the mean particle size and degree of polydispersity. Here, a conservative estimate would be to choose a higher mean size as this will be used as the critical size a_{crit} to estimate the maximum N_0. For the polydispersity degree σ, the converse is true.

- The values $\langle a \rangle$ and σ, together with a value of the volume fraction, determine the maximum particle number. In turn, N_0, σ and ϕ determine the volume of the suspension drop. Based on the experimental setup and available equipment (e.g. the drop generator from Mylyk et al. [40] can generate microliter suspension drops), a certain drop size may be preferred (i.e. a different combination of N_0 and ϕ), which can be achieved by adjusting ϕ and recalculating N_0 and the drop volume.

- We have written a basic MATLAB script that achieves this by calculating the volume fraction of a drop, given a certain value of $\langle a \rangle$, σ and drop volume. Linear interpolation is used w.r.t. values of σ and power-law interpolation for interpolating with respect to ϕ. Based on a preliminary analysis, we found that for a fixed drop size, the volume fraction calculated for a certain $\langle a \rangle$ follows a parabolic curve. These curves allow for simply selecting the volume fraction of the drop, based on the known mean size. This preliminary analysis is presented in more detail in Appendix F.

- The experiment can now be performed by preparing the suspension with the given volume fraction and extracting a drop with the specified volume and releasing that into the settling tank.

- During post-processing, we have access to the velocity distribution of particles. The final values of N_0 and ϕ can be used to calculate the (approximate) initial velocity of the drop relative to the Stokes velocity $\mathrm{V}_0/\mathrm{V}_\mathrm{s}$ with equation 27. The measured distribution together with V_0 can be used to assess whether the measured settling velocity is enhanced or close to the Stokes velocity. This analysis was already presented in the relevant sections in this study and Appendix C gives specific distributions to compare with.

In summary, the most important achievements of this study are:

- Present a theoretical basis for the measuring of particle Stokes velocities by measuring the average settling speed of a suspension drop, including the effects of drop properties like drop size, volume fraction and polydispersity. The end result is approximate formulas that can be used by experimentalists as well as an example workflow that can be tested. A preliminary analysis on the final data indicate that it is sufficient to choose the volume fraction directly based on the size of the drop and the mean size of the particles.

- Perform a comprehensive investigation into the velocity drop and particle leakage observed in particle clouds, as well as the velocity of leaked particles and the evolution of the velocity distribution of all particles. The analysis includes the effect of the number of particles, volume fraction and polydispersity degree.

- Produce novel findings in the context of polydisperse particle clouds, such as the use of prior knowledge about the size distribution to calculate the initial velocity, the similarity between particle clouds with a continuous or discrete size distribution and the preferential leakage of smaller particles from a fully polydisperse cloud and its dependence on the polydispersity degree and independence on the particle number.

6.2 Recommendations for further research

- **Experimentally validate the findings of this study**
  Considering the fact that the simulations are somewhat of a simplifaction from the experimental setting in the lab, it would be very interesting to test the findings of this study experimentally. Specifically, this would involve measuring the velocity of particles at a certain position along a tank where a suspension drop is made to settle. The sizes of the particles in the drop have to be approximately known, so that the Stokes velocity is known. Also, similar to what was done by Metzger et al. and others [34, 40, 51], the suspension drop needs to be generated carefully to prevent entrainment of outside fluid. These experiments could be done for monodisperse, as well as polydisperse drops. In addition, it would be interesting to see if the velocity distribution can also be used in the experiments in a similar way as was presented in this study. If it is found that the results match with the present study, a follow-up study could investigate whether the same conclusions hold for the case where suspension drops are pipetted and there is less regard for ensuring a spherical particle cloud. For example, it could turn out that higher volume fractions in this case are actually counterproductive. Then, not only can conclusions be made with regards to the validity of this study, but also on which of the two types of experiments should actually be the preferred choice for measuring the Stokes settling velocity of particles.

- **Numerical study specific to DSM suspension drop experiment**
  The application we discussed in the introduction had some distinct features compared to this study. First, we used equal density particles while the flocs in the relevant experiments have a size dependent density. It might be interesting to perform the simulations using a size dependent density similar to plot B and C in Figure 11. Moreover, as can be seen from the size range, the samples can be highly polydisperse. The corresponding value of σ (though the distribution is left-skewed) would be higher than what was studied here. It would also be useful to simulate this considering the effect polydispersity has on particle leakage (Fig. E.3). Finally, the method we used for including polydispersity implies that the error will be higher for larger particle sizes (Fig. 30). Considering this, it may be more interesting to base the size limit a_{crit} on a velocity that must be reached by larger particles, considering that the error for smaller particles will already be relatively low.

- **Numerical study into the destabilization of polydisperse clouds**
  In this study, we presented the finding that polydisperse clouds with discrete size distributions break-up at a larger time and distance. However, the amount of clouds simulated was limited and only for one particle number. Therefore, a more thorough numerical study should compare continuous with discrete clouds for more particle numbers. Also, it would be interesting to obtain more statistics for the probability of break-up into two clouds vs. break-up by steady desintegration (or break-up into more than two clouds) for highly polydisperse clouds. As the literature confirms that monodisperse particle clouds always break up into two clouds if they contain more than a thousand particles, a significant departure from this behaviour for polydisperse clouds is definitely worth investigating more.

- **Study different discrete polydispersities**
  Sometimes, the size distribution is neither continuous nor discrete along a continuous interval. A sample may contain several types of matter that each have their respective size distributions. This may be modelled by a bi-, tri- or tetradisperse suspension. We

know how approximately how particles in bidisperse clouds will segregate depending on the size ratio and fraction particle numbers, but what has not been studied is what the influence will be on the drop velocity and what happens when the drop has more sizes in which case there is also not one size ratio.

- **Clouds with higher particle numbers**
  The current study was limited to suspension drops with between 100 and 1000 particles. Power-law relations were found, hence it may be the case that the results can be extrapolated for higher particle numbers. This would also suggest that the difference between N_0=2000 and N_0=1000 is similar to the difference between the latter and N_0=500. Also, if this is indeed the case, we can theoretically predict that maximum drop volumes will keep decreasing for increasing N_0. E.g. if the particle number doubles, the critical size will likely be halved, leading to a drop volume that is $1/2^3{\cdot}2 = 1/4$ as large. Continuing this line of reasoning, there will be a point where the maximum volume is unrealistically small. If we set this limit at 0.5 L and assume the growth factor to be 2 and use volume fraction 0.01, this volume would be reached at a particle number of approximately 2300. Note that this is in the monodisperse case, for the polydisperse case the prediction would be higher. It would be interesting to test this prediction as it would extend the findings and their practical usability.

- **Dilute limit polydisperse particle clouds**
  We saw that at very low volume fractions, the typical formation of an internally circulating spherical particle cloud is disturbed by the presence of polydispersity. This occurs starting at volume fractions of 0.1 %, but is also dependent on the particle number N_0. Similar to settling suspensions, these particle clouds do not maintain their structure but the particles separate according to their sizes. This causes a very fast transition from enhanced settling to lower settling velocities. The dynamics concerning this are complex, and it is not exactly known which conditions are necessary to cause this deviation. Thus, this would be an interesting avenue for further study. This would also give more insight into what causes the cloud formation and the associated collective settling behavior. We expect that at lower polydispersities, e.g. $\sigma < 0.1$, cloud formation may be possible but this needs to be investigated along with the effects of ϕ and N_0. Finally, it would also be interesting to see whether a cloud with discretized particle size distribution has a similar transition from collective settling to individual settling, or if the groups of similar sizes have a stabilizing effect, and if the transition is similar, whether the resulting separation leads to a continuous distribution of sizes (similar to Fig. 31) or if there is a difference between the continuous and discrete case similar to what is seen in hindered settling.

References

[1] Morris J. Guazzelli, E. *A Physical Introduction to Suspension Dynamics.* Cambridge University Press, 2012.

[2] Nicola Mingotti and Andrew W. Woods. Stokes settling and particle-laden plumes: Implications for deep-sea mining and volcanic eruption plumes: Particle laden plumes and intrusions. *Philosophical Transactions of the Royal Society A: Mathematical, Physical and Engineering Sciences*, 378, 9 2020.

[3] Nicola Mingotti and Andrew W. Woods. Dynamics of sediment-laden plumes in the ocean. *Flow*, 2, 2022.

[4] Thomas Peacock and Raphael Ouillon. The fluid mechanics of deep-sea mining. *Annual Review of Fluid Mechanics Annu. Rev. Fluid Mech. 2023*, 55:2022, 2023.

[5] Dong Wang, Dao Ho-Minh, and Danielle S. Tan. Discrete element modelling of sediment falling in water. *European Physical Journal E*, 39, 11 2016.

[6] Dong Wang and Danielle S. Tan. An investigation of the effect of aspect and compression ratios on sediment dispersion using discrete element modelling. *AIP Advances*, 7, 12 2017.

[7] W Ali. Flocculation and deep-sea mining plumes.

[8] W. Ali, A. Kirichek, and C. Chassagne. Collective effects on the settling of clay flocs. *Applied Clay Science*, 254, 6 2024.

[9] H. S. Viswanathan, J. Ajo-Franklin, J. T. Birkholzer, J. W. Carey, Y. Guglielmi, J. D. Hyman, S. Karra, L. J. Pyrak-Nolte, H. Rajaram, G. Srinivasan, and D. M. Tartakovsky. From fluid flow to coupled processes in fractured rock: Recent advances and new frontiers, 3 2022.

[10] Baptiste Penlou, Olivier Roche, Michael Manga, and Siet van den Wildenberg. Experimental measurement of enhanced and hindered particle settling in turbulent gas-particle suspensions, and geophysical implications. *Journal of Geophysical Research: Solid Earth*, 128, 3 2023.

[11] Ian L. Molnar, Erica Pensini, Md Abdullah Asad, Chven A. Mitchell, Ludwig C. Nitsche, Laura J. Pyrak-Nolte, Gastón L. Miño, and Magdalena M. Krol. Colloid transport in porous media: A review of classical mechanisms and emerging topics. *Transport in Porous Media*, 130:129–156, 10 2019.

[12] David M. Broday and Risa Robinson. Application of cloud dynamics to dosimetry of cigarette smoke particles in the lungs. *Aerosol Science and Technology*, 37:510–527, 6 2003.

[13] Paola Leon Plata, Ying Liu, and Ludwig C. Nitsche. Interaction of multiple drops and formation of toroidal-spiral particles. *Physical Review Fluids*, 3, 9 2018.

[14] G. K. Batchelor. *An Introduction to Fluid Dynamics.* Springer, 1967.

[15] Sangtae Kim and Seppo J Karrila. *Microhydrodynamics: principles and selected applications.* Butterworth-Heinemann, 2013.

[16] John F Brady and Georges Bossis. Stokesian dynamics, 1988.

[17] John Garside and Maan R Al-Dibouni. Velocity-voidage relationships for fluidization and sedimentation in solid-liquid systems. *Industrial & engineering chemistry process design and development*, 16(2):206–214, 1977.

[18] JF Richardson and WN Zaki. Sedimentation and fluidisation: Part i. *Chemical Engineering Research and Design*, 75:S82–S100, 1997.

[19] Robert H Davis and Andreas Acrivos. Sedimentation of noncolloidal particles at low reynolds numbers, 1985.

[20] GK Batchelor. Sedimentation in a dilute polydisperse system of interacting spheres. part 1. general theory. *Journal of Fluid Mechanics*, 119:379–408, 1982.

[21] George J Kynch. A theory of sedimentation. *Transactions of the Faraday society*, 48:166–176, 1952.

[22] JSCR Hadamard. Mouvement permanent lent d'une sphere liquid et visqueuse dans un liquid visqueux. *(No Title)*, 152:1735, 1911.

[23] Witold Rybczynski. Uber die fortschreitende bewegung einer flussigen kugel in einem zahen medium. *Bull. Acad. Sci. Cracovie A*, 1:40–46, 1911.

[24] J. M. Nitsche and G. K. Batchelor. Break-up of a falling drop containing dispersed particles. *Journal of Fluid Mechanics*, 340:161–175, 6 1997.

[25] Gustavo Coelho Abade and Francisco Ricardo Cunha. Computer simulation of particle aggregates during sedimentation. *Computer Methods in Applied Mechanics and Engineering*, 196:4597–4612, 9 2007.

[26] Christoph Kloss, Christoph Goniva, Alice Hager, Stefan Amberger, and Stefan Pirker. Models, algorithms and validation for opensource dem and cfd-dem. *Progress in Computational Fluid Dynamics*, 12:140–152, 2012.

[27] Cyrus K. Aidun and Jonathan R. Clausen. Lattice-boltzmann method for complex flows, 1 2010.

[28] S. Balachandar and John K. Eaton. Turbulent dispersed multiphase flow, 1 2010.

[29] Martin Maxey. Simulation methods for particulate flows and concentrated suspensions, 1 2017.

[30] Joontaek Park, Bloen Metzger, Elisabeth Guazzelli, and Jason E. Butler. A cloud of rigid fibres sedimenting in a viscous fluid. *Journal of Fluid Mechanics*, 648:351–362, 4 2010.

[31] Zhifeng Bai, Mingzhong Li, Feng Li, and Qiuying Du. Study on particle cluster dynamics behavior in settling and the influence by fiber barrier. *Frontiers in Materials*, 9, 12 2022.

[32] Élisabeth Guazzelli and John Hinch. Fluctuations and instability in sedimentation. *Annual Review of Fluid Mechanics*, 43:97–116, 1 2011.

[33] Ehssan Nazockdast, Abtin Rahimian, Denis Zorin, and Michael Shelley. A fast platform for simulating semi-flexible fiber suspensions applied to cell mechanics. *Journal of Computational Physics*, 329:173–209, 1 2017.

[34] Bloen Metzger, Maxime Nicolas, and Élisabeth Guazzelli. Falling clouds of particles in viscous fluids. *Journal of Fluid Mechanics*, 580:283–301, 6 2007.

[35] Carl Wilhelm Oseen. Uber die stokes' sche formel und uber eine verwandte aufgabe in der hydrodynamik. *Arkiv Mat., Astron. och Fysik*, 6:1, 1910.

[36] G. Subramanian and Donald L. Koch. Evolution of clusters of sedimenting low-reynolds-number particles with oseen interactions. *Journal of Fluid Mechanics*, 603:63–100, 2008.

[37] Bloen Metzger and Jason E. Butler. Clouds of particles in a periodic shear flow. *Physics of Fluids*, 24, 2 2012.

[38] Benjamin Marchetti, Laurence Bergougnoux, and Elisabeth Guazzelli. Falling clouds of particles in vortical flows. *Journal of Fluid Mechanics*, 908, 2020.

[39] Quentin Kriaa, Eliot Subra, Benjamin Favier, and Michael Le Bars. Effects of particle size and background rotation on the settling of particle clouds. *Physical Review Fluids*, 7, 12 2022.

[40] Anna Myłyk, Walter Meile, Günter Brenn, and Maria L. Ekiel-Jezewska. Break-up of suspension drops settling under gravity in a viscous fluid close to a vertical wall. *Physics of Fluids*, 23, 2011.

[41] Gunther Machu, Walter Meile, Ludwig C. Nitsche, and U. W.E. Schaflinger. Coalescence, torus formation and breakup of sedimenting drops: Experiments and computer simulations. *Journal of Fluid Mechanics*, 447:299–336, 11 2001.

[42] Florent Pignatel, Maxime Nicolas, and Élisabeth Guazzelli. A falling cloud of particles at a small but finite reynolds number. *Journal of Fluid Mechanics*, 671:34–51, 3 2011.

[43] Pinzhuo Chen, Sheng Chen, Mengmeng Yang, and Shuiqing Li. Falling clouds of particles with finite inertia in viscous flows. *Physics of Fluids*, 33, 3 2021.

[44] Oladapo Ayeni, Shashank S. Tiwari, Chunliang Wu, Jyeshtharaj B. Joshi, and Krishnaswamy Nandakumar. Behavior of particle swarms at low and moderate reynolds numbers using computational fluid dynamics - discrete element model. *Physics of Fluids*, 32, 7 2020.

[45] B R Morton, Geoffrey Taylor, and J S Turner. Turbulent gravitational convection from maintained and instantaneous sources, 1956.

[46] Cara B.G. James, Nicola Mingotti, and Andrew W. Woods. On particle separation from turbulent particle plumes in a cross-flow. *Journal of Fluid Mechanics*, 932, 2 2022.

[47] Adrian C.H. Lai, Ruo Qian Wang, Adrian Wing Keung Law, and E. Eric Adams. Modeling and experiments of polydisperse particle clouds. *Environmental Fluid Mechanics*, 16:875–898, 8 2016.

[48] Thien Tran-Duc, Nhan Phan-Thien, and Boo Cheong Khoo. A smoothed particle hydrodynamics (sph) study on polydisperse sediment from technical activities on seabed. *Physics of Fluids*, 30, 2 2018.

[49] Thien Tran-Duc, Nhan Phan-Thien, and Boo Cheong Khoo. A three-dimensional smoothed particle hydrodynamics dispersion simulation of polydispersed sediment on the seafloor using a message passing interface algorithm. *Physics of Fluids*, 31, 4 2019.

[50] F. Bülow, H. Nirschl, and W. Dörfler. On the settling behaviour of polydisperse particle clouds in viscous fluids. *European Journal of Mechanics, B/Fluids*, 50:19–26, 2015.

[51] Melissa Faletra, Jeffrey S. Marshall, Mengmeng Yang, and Shuiqing Li. Particle segregation in falling polydisperse suspension droplets. *Journal of Fluid Mechanics*, 769:79–102, 2015.

[52] Thinh X. Ho, Nhan Phan-Thien, and Boo Cheong Khoo. Destabilization of clouds of monodisperse and polydisperse particles falling in a quiescent and viscous fluid. *Physics of Fluids*, 28, 6 2016.

[53] K R Dyer and A J Manning. Observation of the size, settling velocity and effective density of flocs, and their fractal dimensions, 1999.

[54] M. L. Ekiel-Jezewska, B. Metzger, and É Guazzelli. Spherical cloud of point particles falling in a viscous fluid. *Physics of Fluids*, 18, 2006.

[55] A J Goldman?, R G Cox, *andH Brenner.Theslowmotionoftwoidenticalarbitrarilyorientedspheresth*

Appendices

A Particle size distributions

This section contains the particle size distributions that were used in the simulation of the particle clouds for the comparison between particle clouds with continuous and those with discrete size distributions.

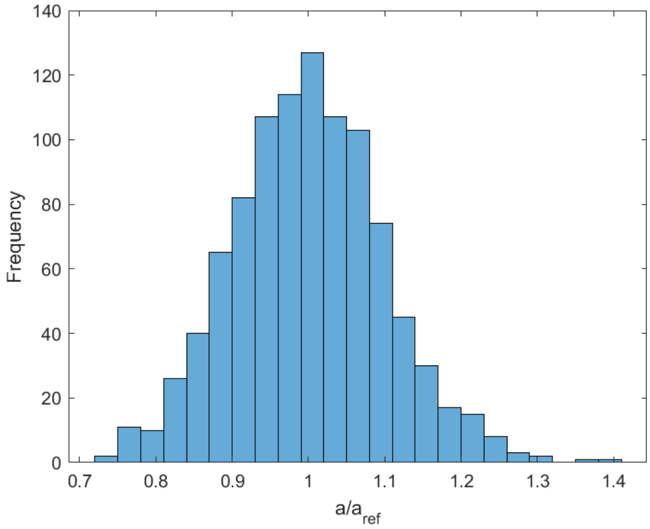

Figure A.1: The continuous particle size distribution generated using N_0=1000 and σ=0.1. After removal of sizes outside the interval [0.4 1.6], N_0=990, $\overline{a}$=1.00 and σ=0.0992.

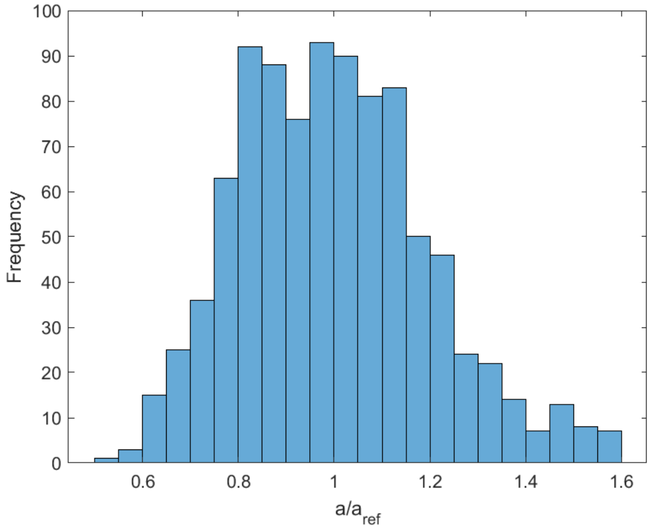

Figure A.2: The continuous particle size distribution generated using N_0=1000 and σ=0.2. After removal of sizes outside the interval [0.4 1.6], N_0=937, $\overline{a}$=0.9994 and σ=0.1966.

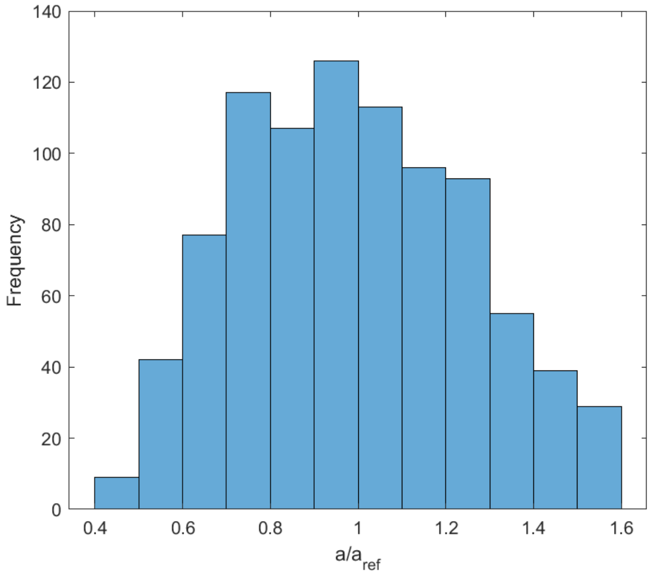

Figure A.3: The continuous particle size distribution generated using N_0=1000 and σ=0.3. After removal of sizes outside the interval [0.4 1.6], N_0=903, $\overline{a}$=0.9937 and σ=0.2616.

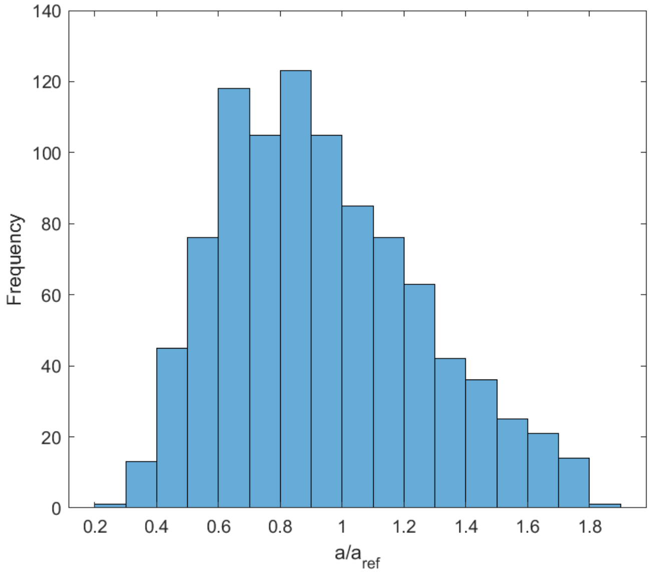

Figure A.4: The continuous particle size distribution generated using N_0=1000 and σ=0.4. After removal of sizes greater than 2, N_0=949, $\overline{a}$=0.9387 and σ=0.3211.

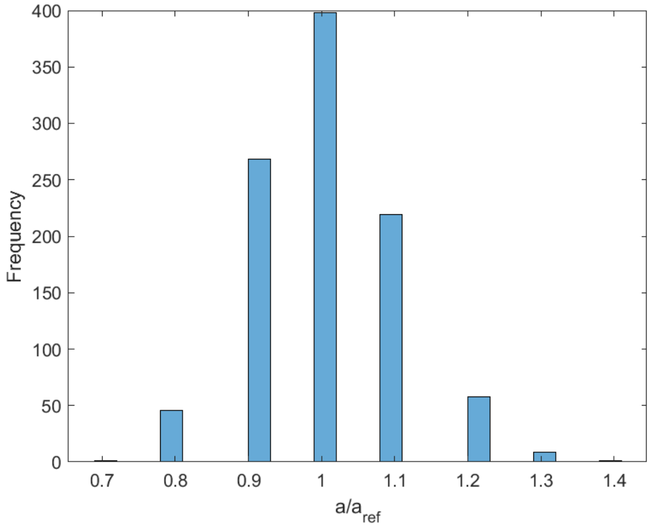

Figure A.5: The discrete particle size distribution generated using N_0=1000 and σ=0.1. The final properties of the distribution are $\overline{a}$=1.0003 and σ=0.1005.

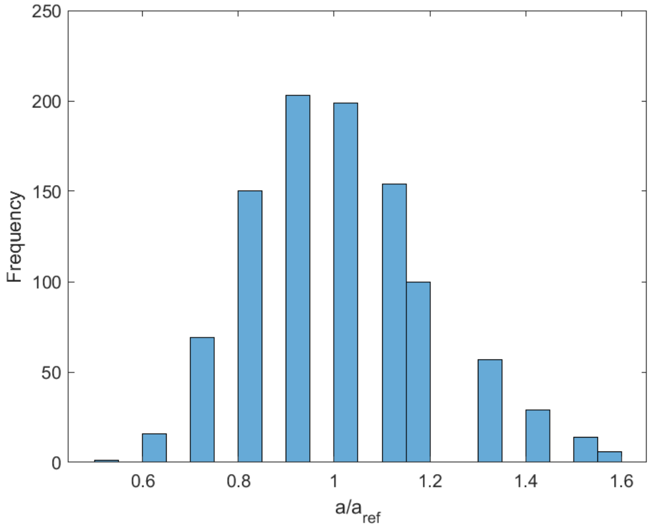

Figure A.6: The discrete particle size distribution generated using N_0=1000 and σ=0.2. The final properties of the distribution are $\overline{a}$=0.9968 and σ=0.1953.

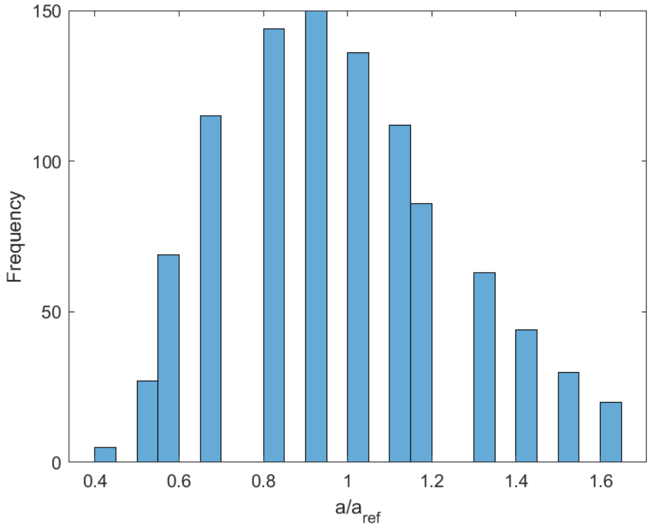

Figure A.7: The discrete particle size distribution generated using N_0=1000 and σ=0.3. The final properties of the distribution are $\overline{a}$=0.9695 and σ=0.2612.

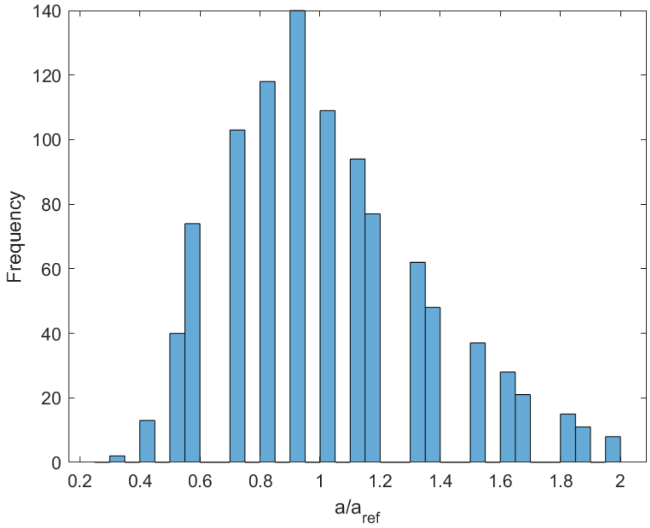

Figure A.8: The discrete particle size distribution generated using N_0=1000 and σ=0.4. The final properties of the distribution are $\overline{a}$=1.0152 and σ=0.3409.

B Images from the settling of particle clouds

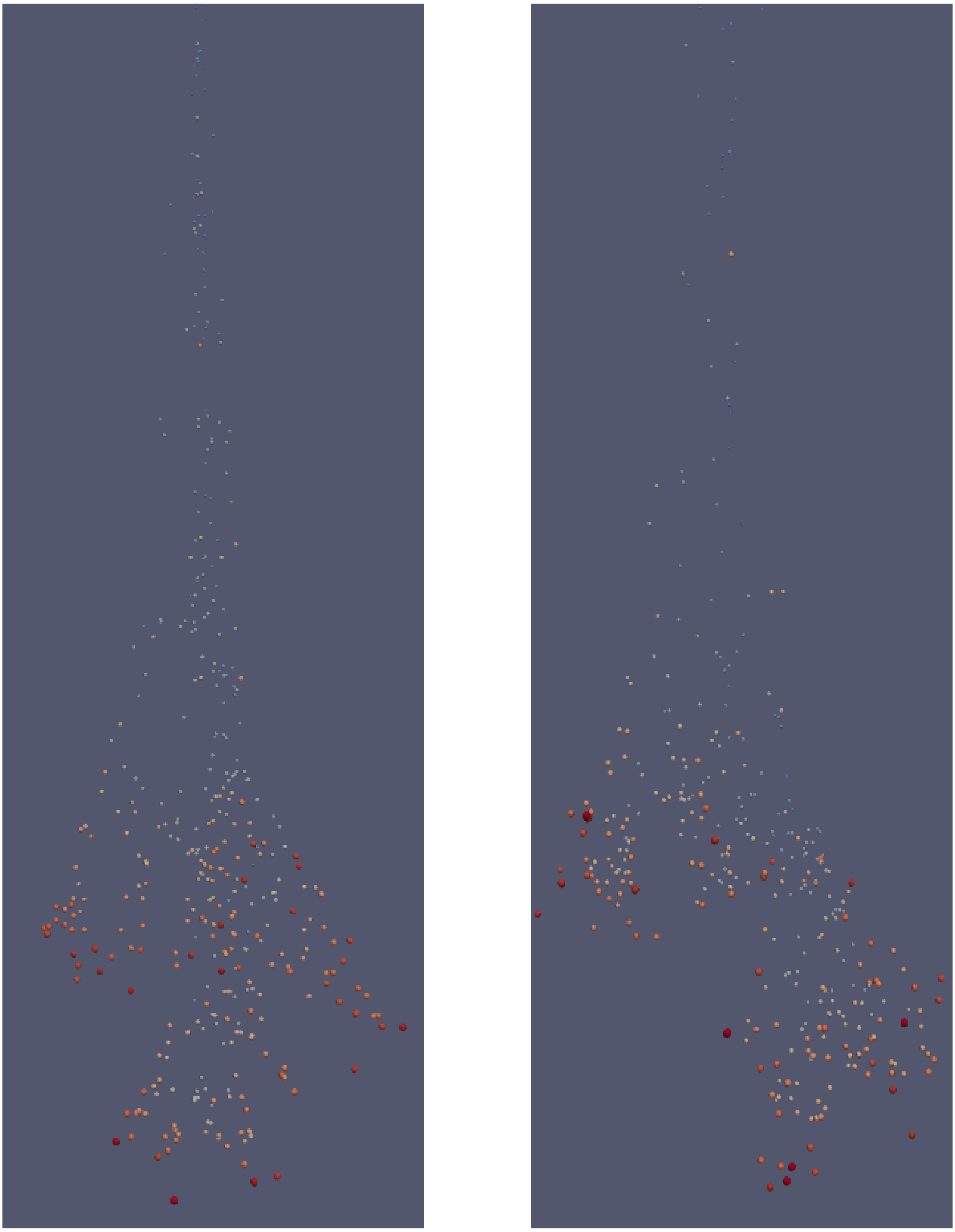

(a) t*=795, scale factor 5

(b) t*=800, scale factor 3

Figure B.1: A snapshot of the two particle clouds with N_0=1000 and σ=0.4. The image on the left shows the cloud with the continuous PSD and the right image shows the cloud with the discrete PSD. The particles are enlarged by a certain factor for visibility.

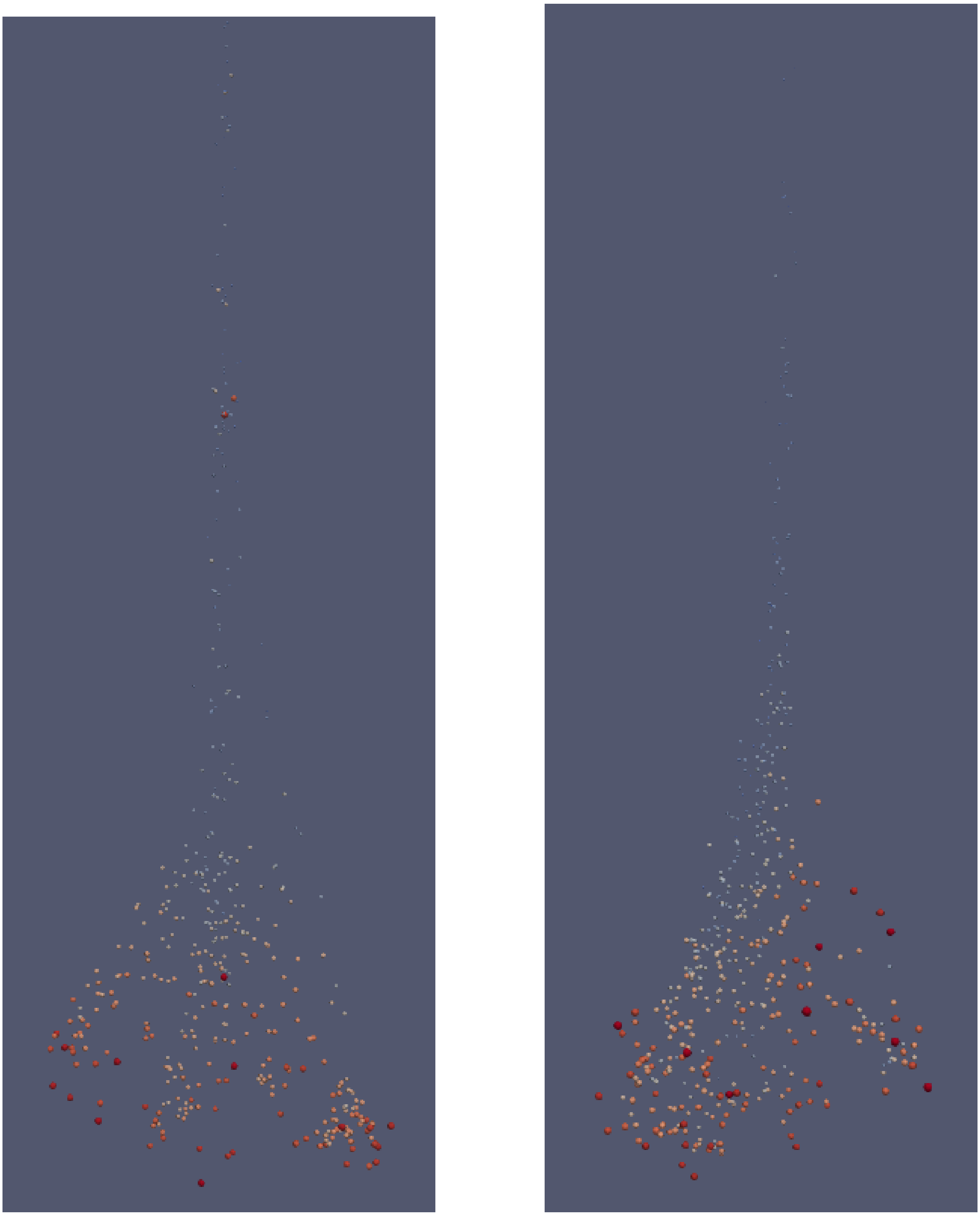

(a) t*=554, scale factor 5

(b) t*=416, scale factor 5

Figure B.2: A snapshot of the two particle clouds with N_0=1000 and σ=0.5. The image on the left shows the cloud with the continuous PSD and the right image shows the cloud with the discrete PSD. It can be seen clearly that the particle cloud does not break up into two distinct cloud, but rather breaks up by gravitational separation of particles due to their velocity difference.

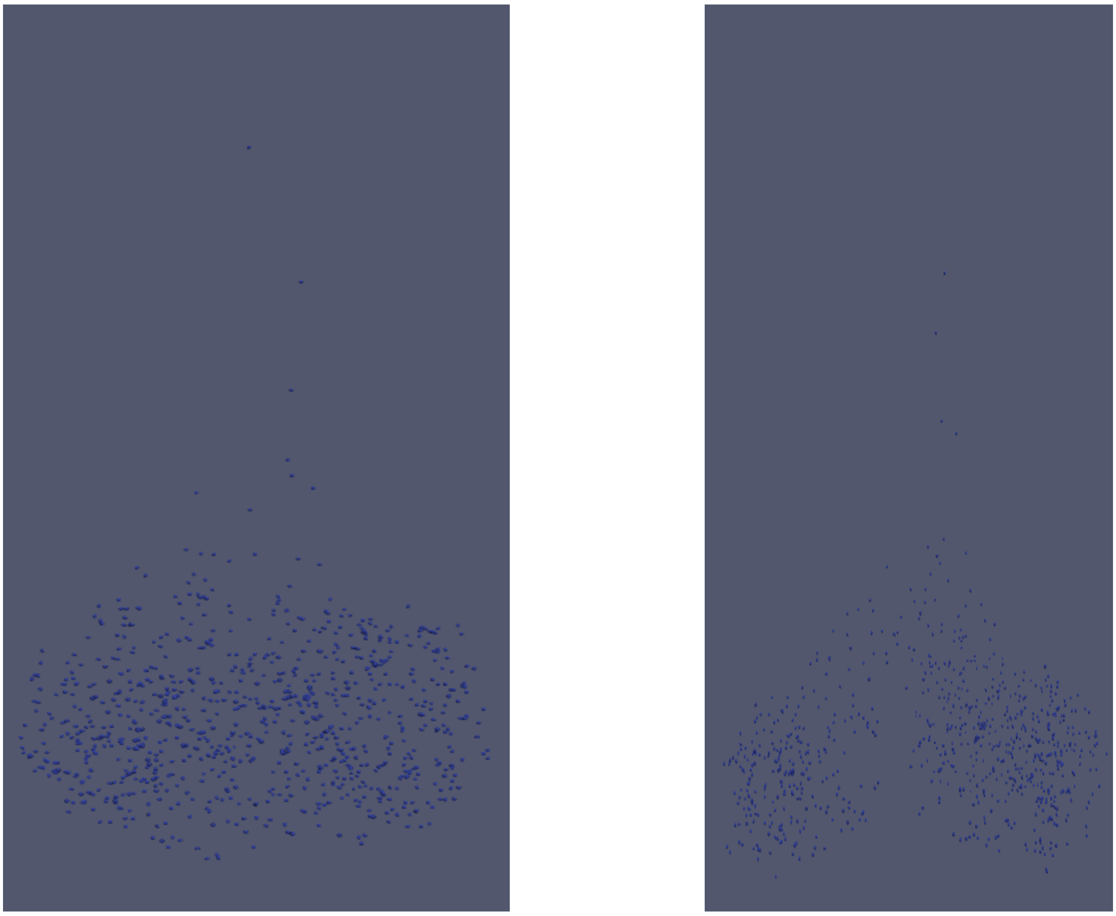

(a) (b)

Figure B.3: Two snapshots of the particle cloud with N_0=1000, ϕ=1% and σ=0, one at half the break-up time and at time of break-up.

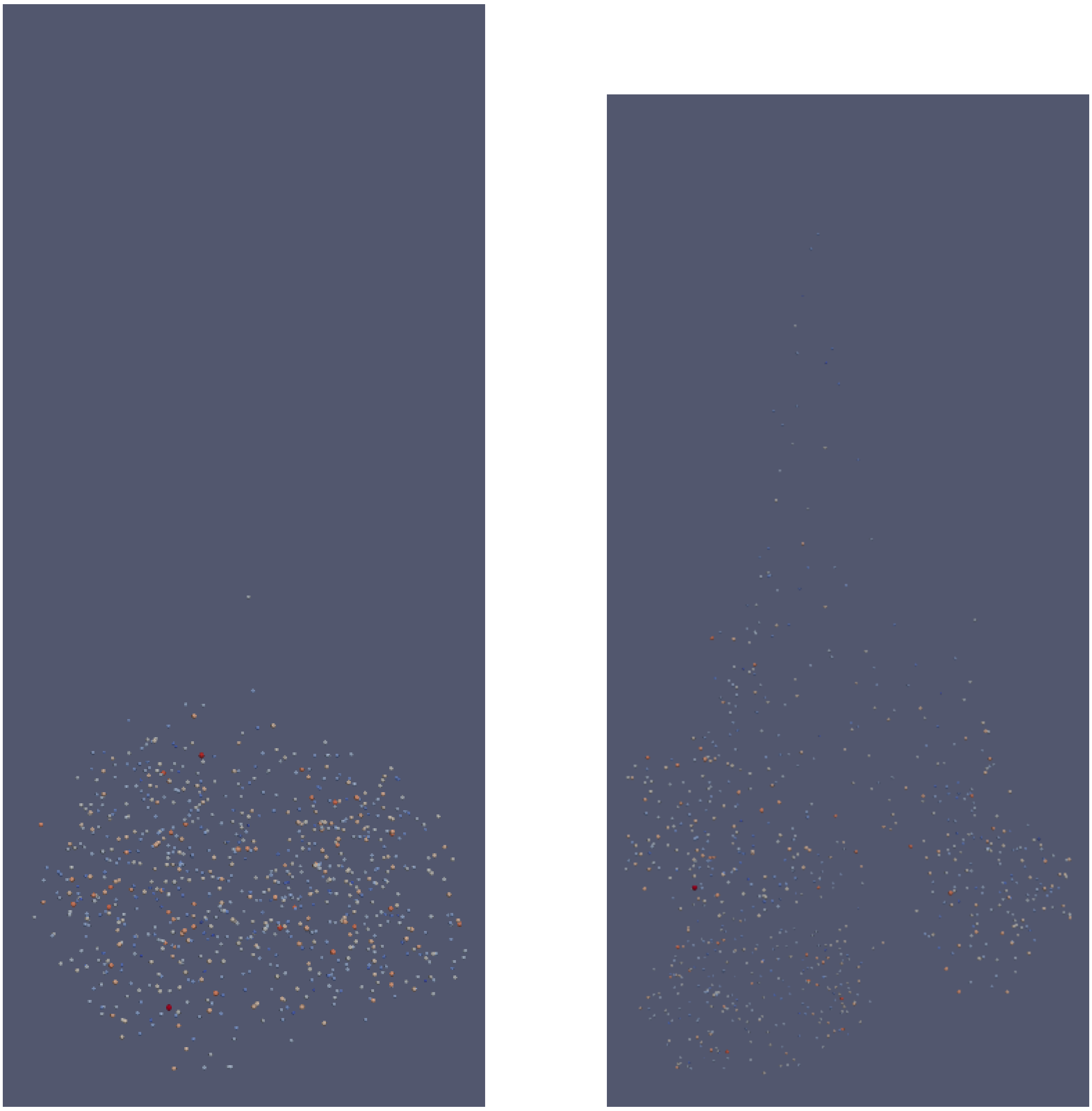
(a) (b)

Figure B.4: Two snapshots of the particle cloud with continuous PSD and with N_0=1000, ϕ=1% and σ=0.1, one at half the break-up time and at time of break-up.

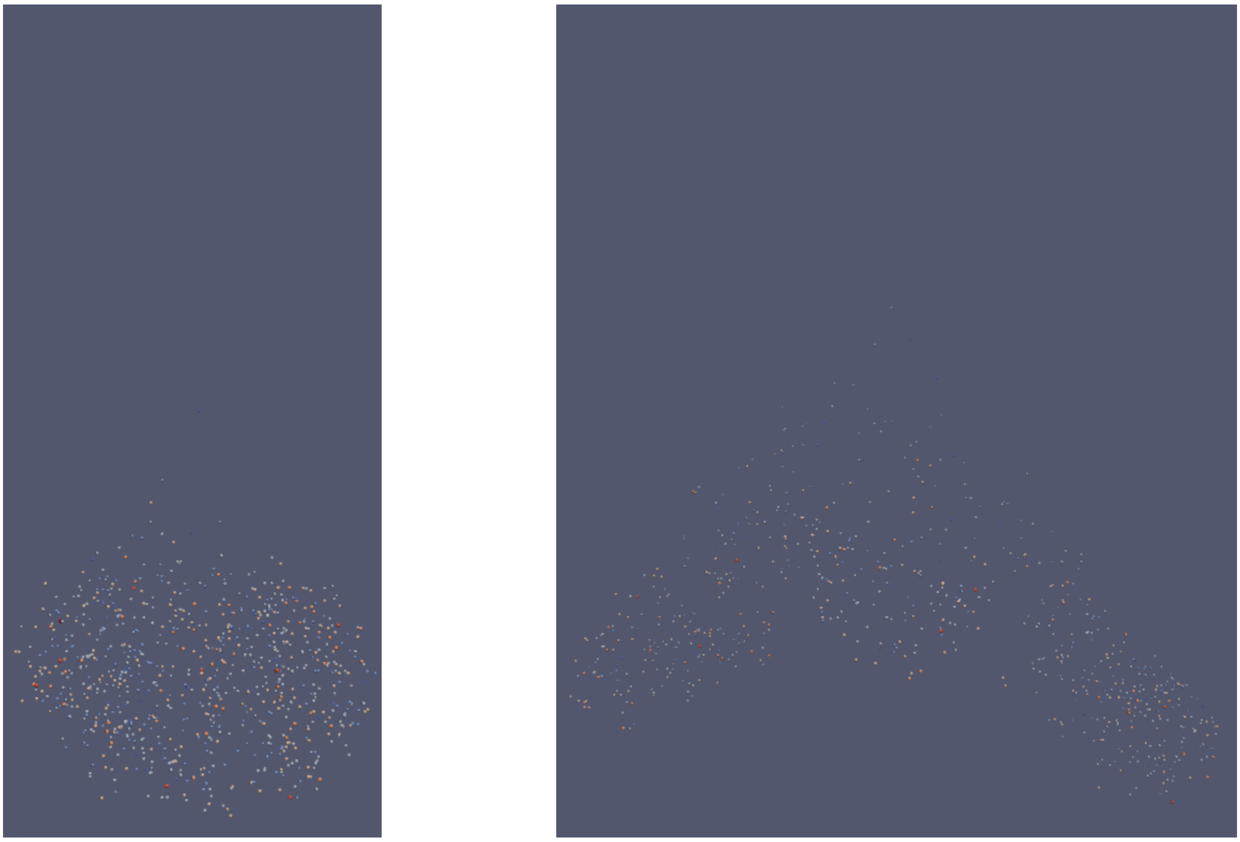
(a) (b)

Figure B.5: Two snapshots of the particle cloud with discrete PSD and with N_0=1000, ϕ=1% and σ=0.1, one at half the break-up time and at time of break-up.

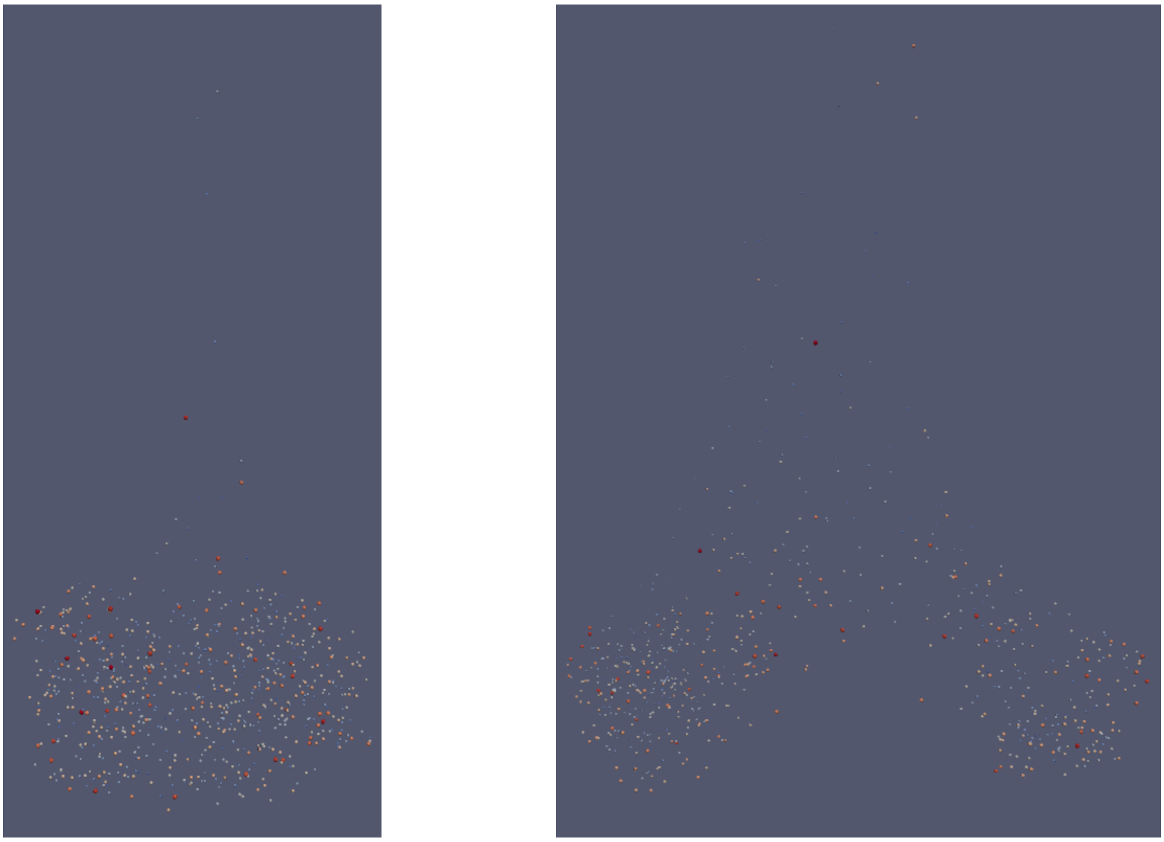

(a)

(b)

Figure B.6: Two snapshots of the particle cloud with continuous PSD and with N_0=1000, ϕ=1% and σ=0.2, one at half the break-up time and at time of break-up.

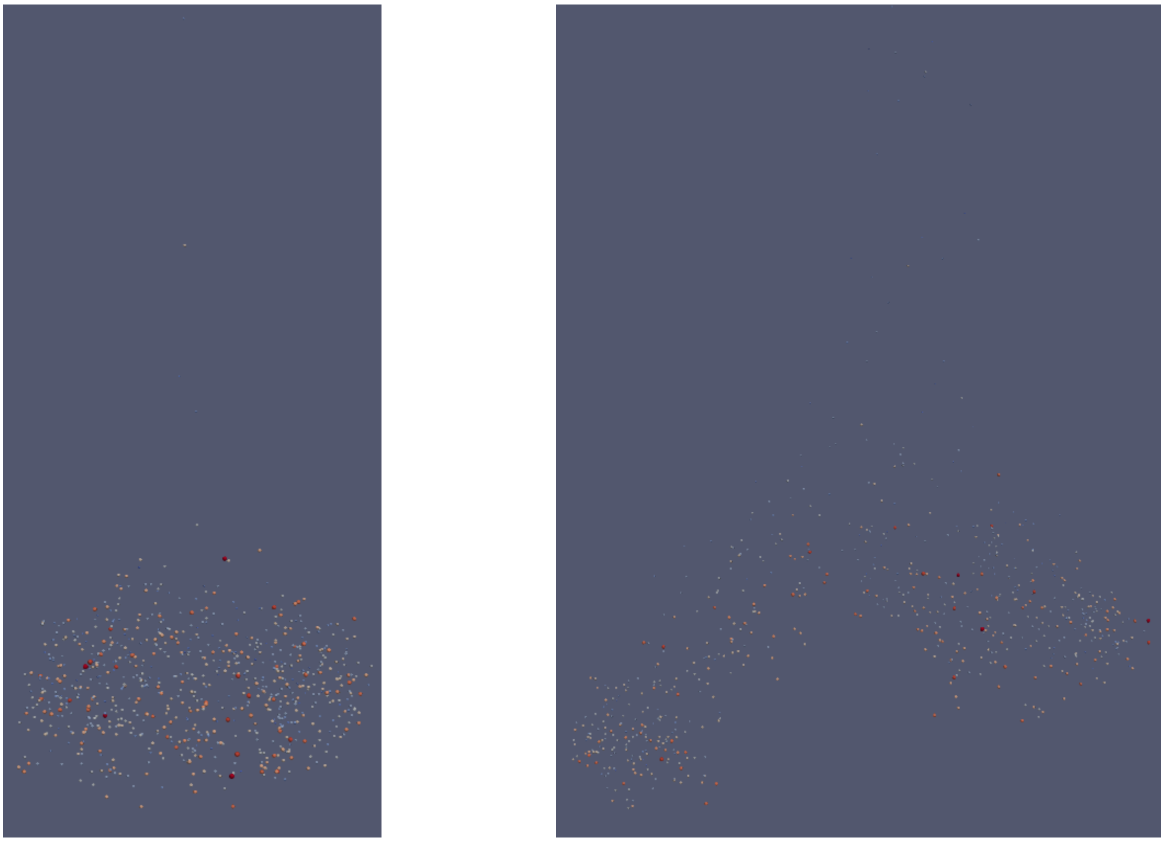

(a) (b)

Figure B.7: Two snapshots of the particle cloud with discrete PSD and with N_0=1000, ϕ=1% and σ=0.2, one at half the break-up time and at time of break-up.

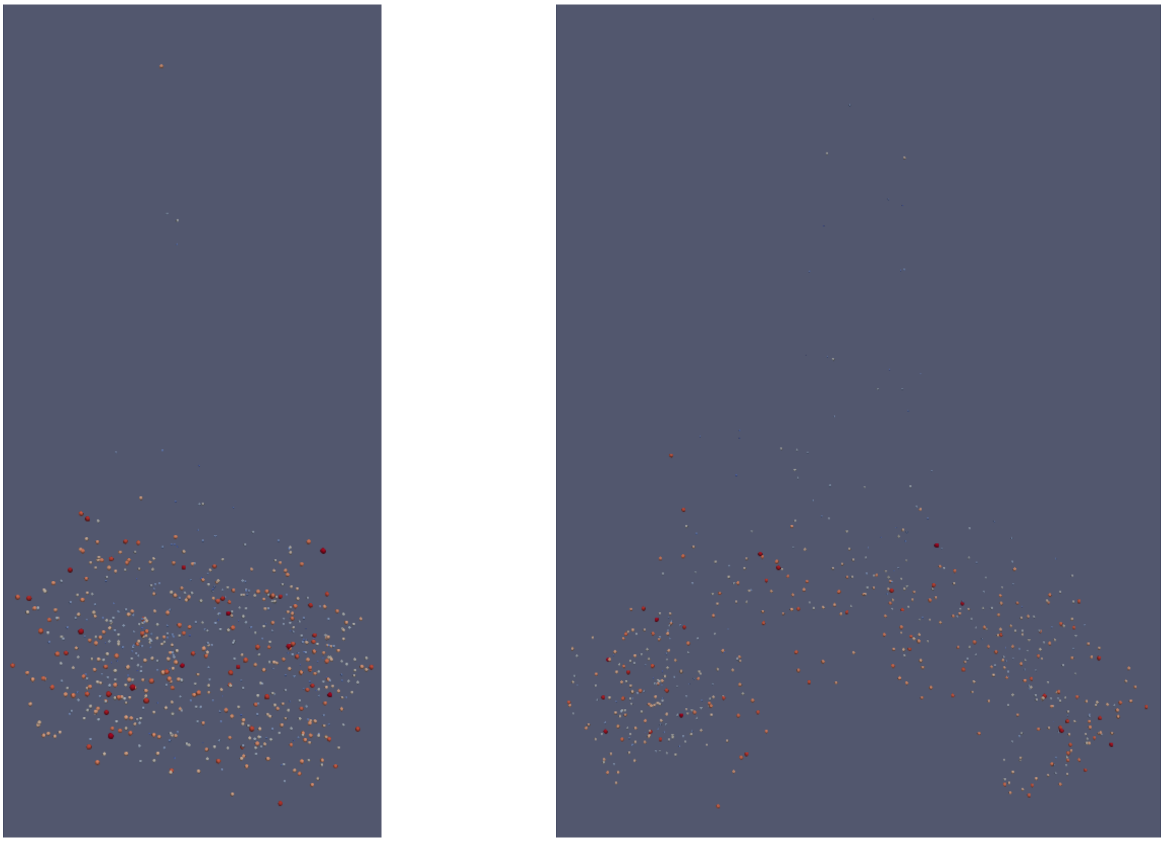

(a) (b)

Figure B.8: Two snapshots of the particle cloud with continuous PSD and with N_0=1000, ϕ=1% and σ=0.3, one at half the break-up time and at time of break-up.

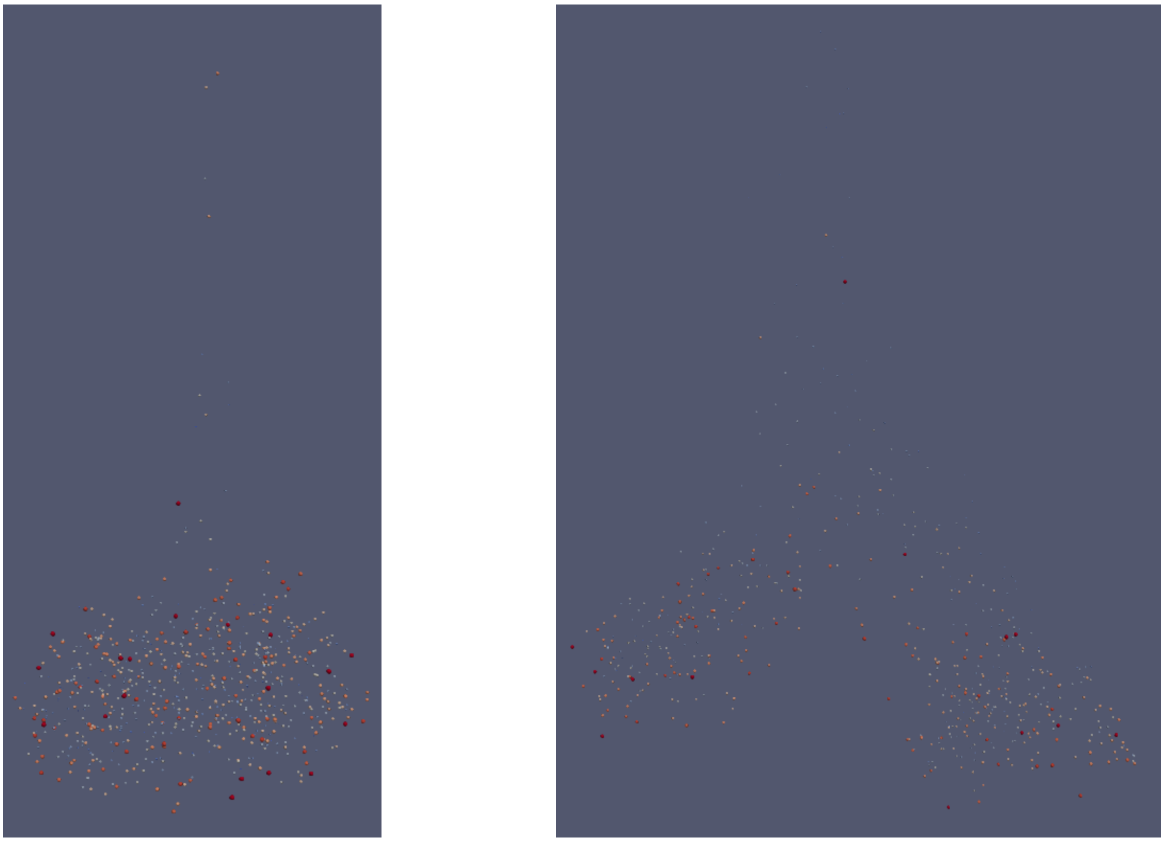

(a) (b)

Figure B.9: Two snapshots of the particle cloud with discrete PSD and with N_0=1000, ϕ=1% and σ=0.3, one at half the break-up time and at time of break-up.

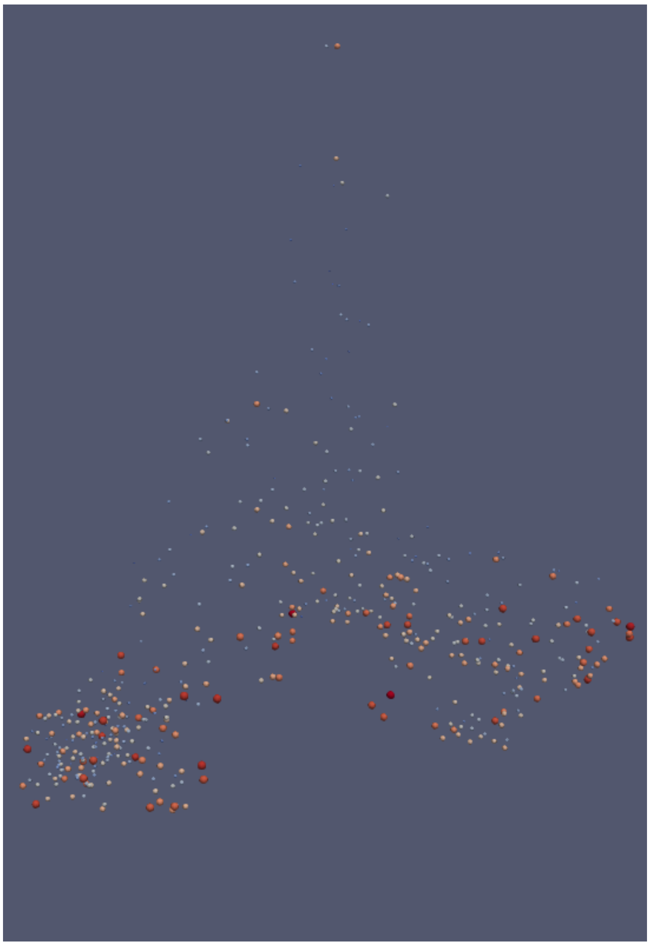

Figure B.10: A snapshot of the particle cloud with N_0=750 and σ=0.4 (ϕ=5%) at the time of break-up into two clouds.

C Velocity distributions at selected times

This section contains plots for a range of simulated clouds. They are ordered in terms of initial cloud velocity, to show that the expected final distribution depends mainly on V_0.

C.1 Monodisperse clouds

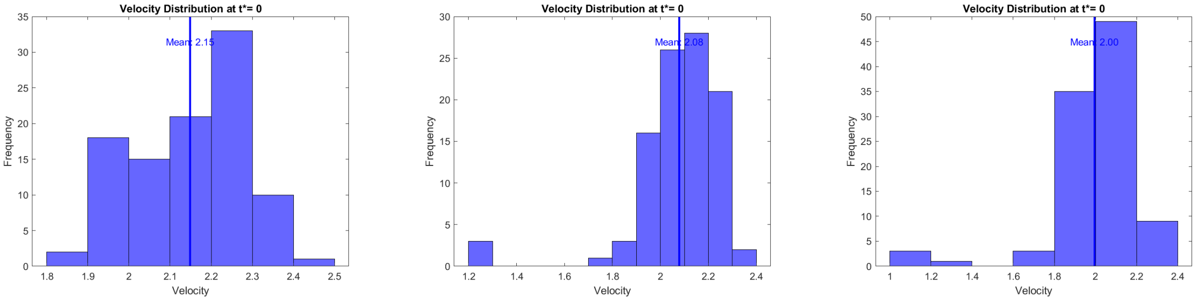

Figure C.1: The velocity distribution at several times for N_0=100 and ϕ=0.01% (V_0=2.22).

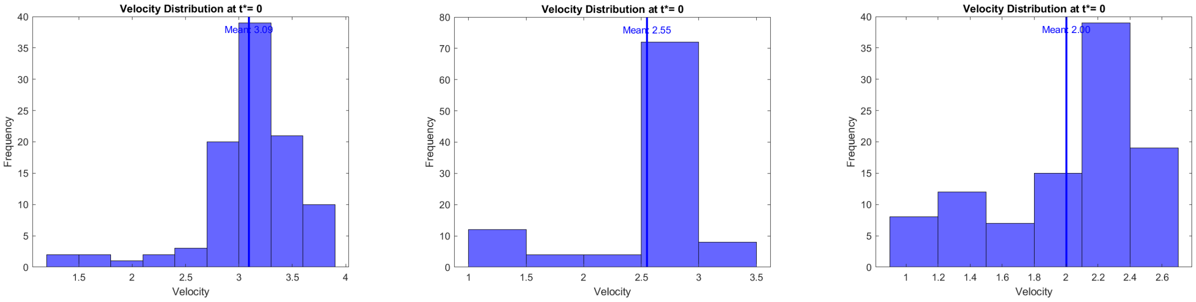

Figure C.2: The velocity distribution at several times for N_0=100 and ϕ=0.1% (V_0=3.60).

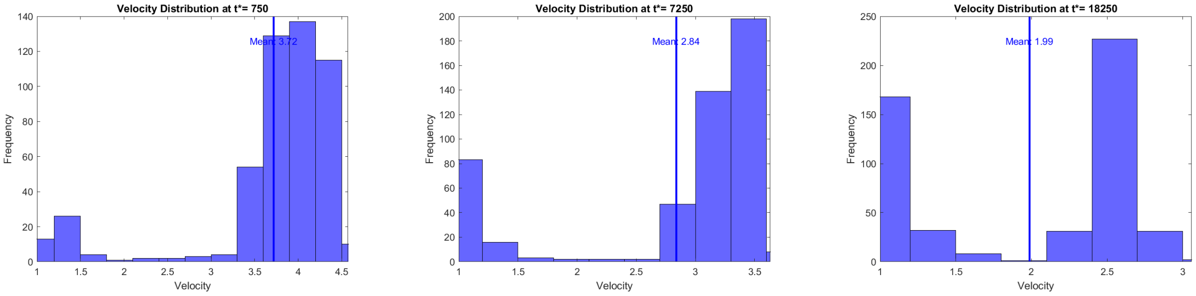

Figure C.3: The velocity distribution at several times for N_0=500 and ϕ=0.01% (V_0=4.50).

C.2 Polydisperse clouds

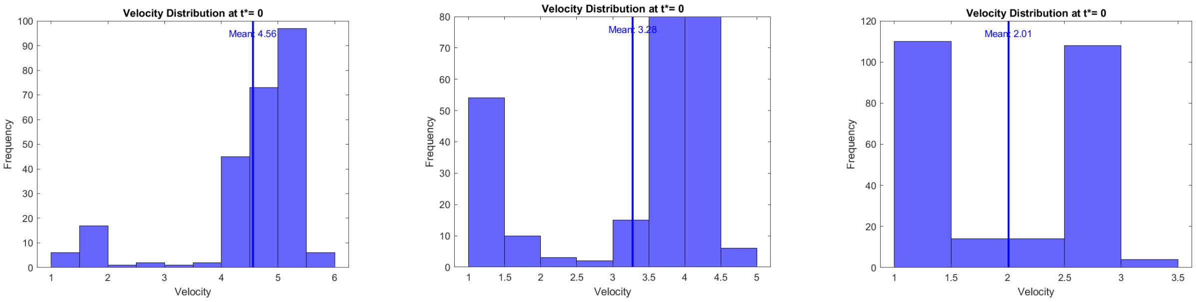

Figure C.4: The velocity distribution at several times for N_0=250 and ϕ=0.1% (V_0=5.85).

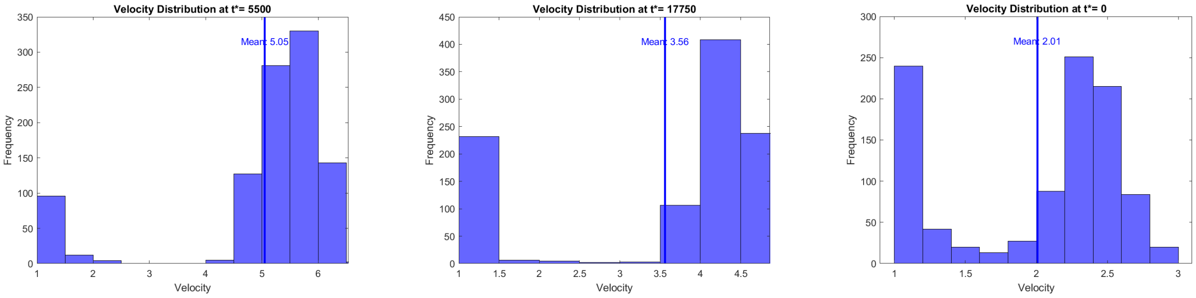

Figure C.5: The velocity distribution at several times for N_0=1000 and ϕ=0.01% (V_0=6.56).

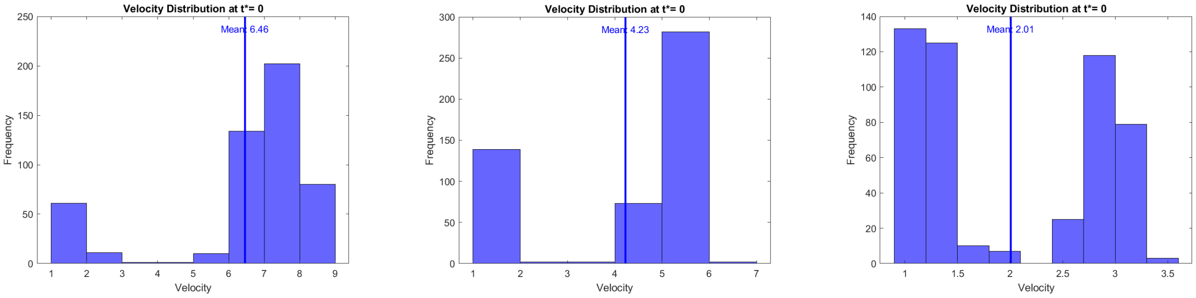

Figure C.6: The velocity distribution at several times for N_0=500 and ϕ=0.1% (V_0=8.72).

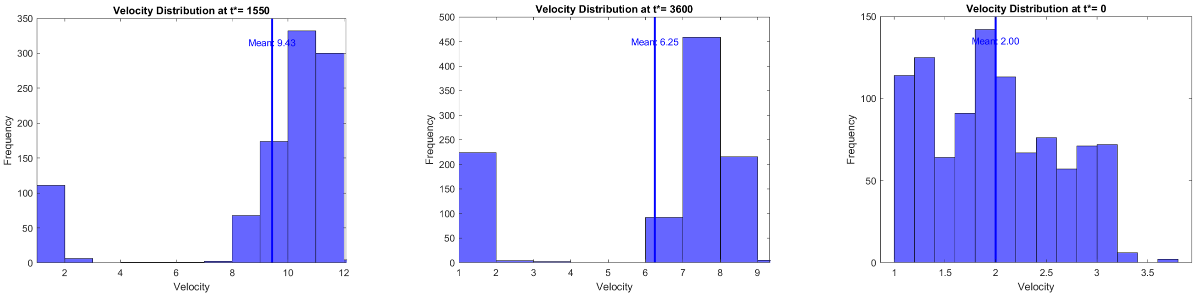

Figure C.7: The velocity distribution at several times for N_0=1000 and ϕ=0.1% (V_0=13.06).

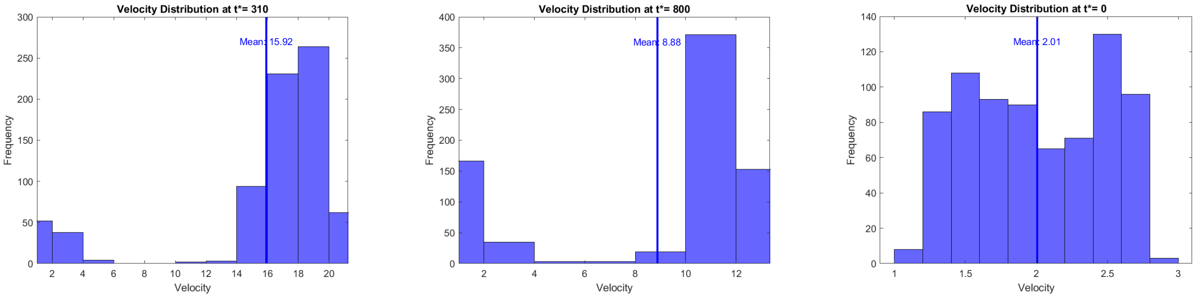

Figure C.8: The velocity distribution at several times for N_0=750 and ϕ=1% (V_0=22.56).

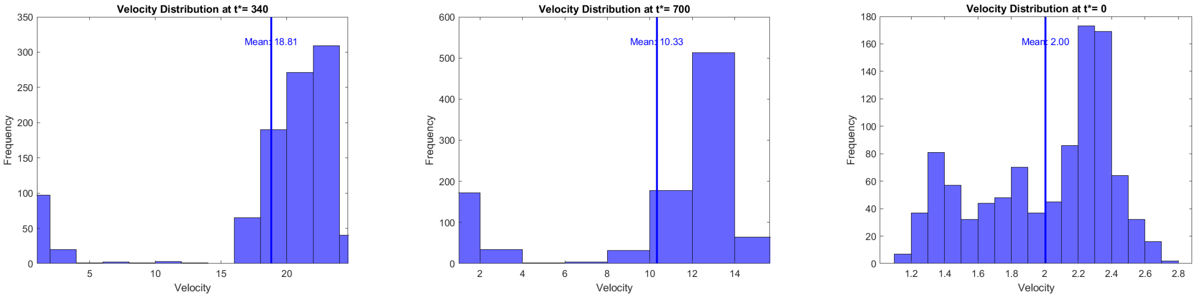

Figure C.9: The velocity distribution at several times for N_0=1000 and ϕ=1% (V_0=27.39).

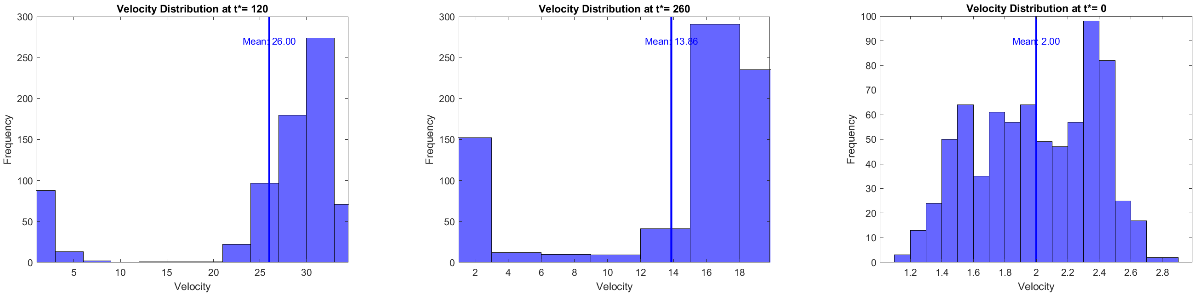

Figure C.10: The velocity distribution at several times for N_0=750 and ϕ=5% (V_0=38.55).

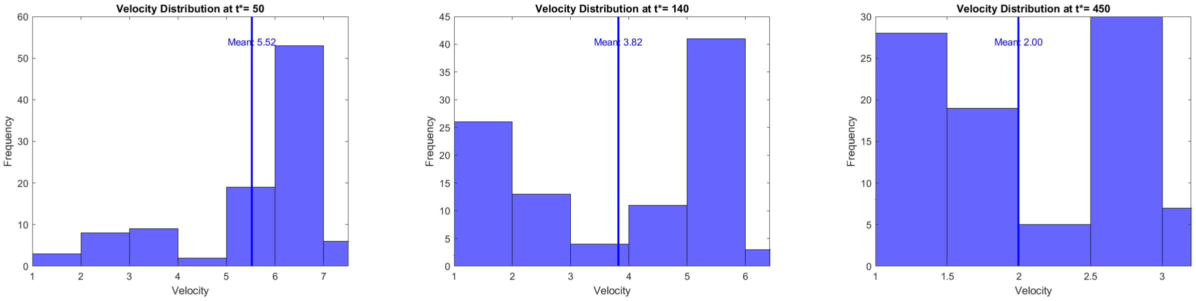

Figure C.11: The velocity distribution at several times for N_0=100, ϕ=1% and σ=0.2 (V_0=7.36).

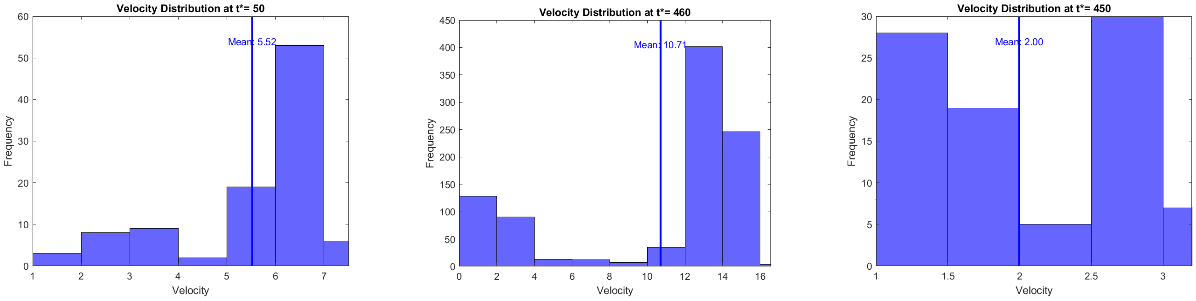

Figure C.12: The velocity distribution at several times for N_0=100, ϕ=1% and σ=0.4 (V_0=7.59).

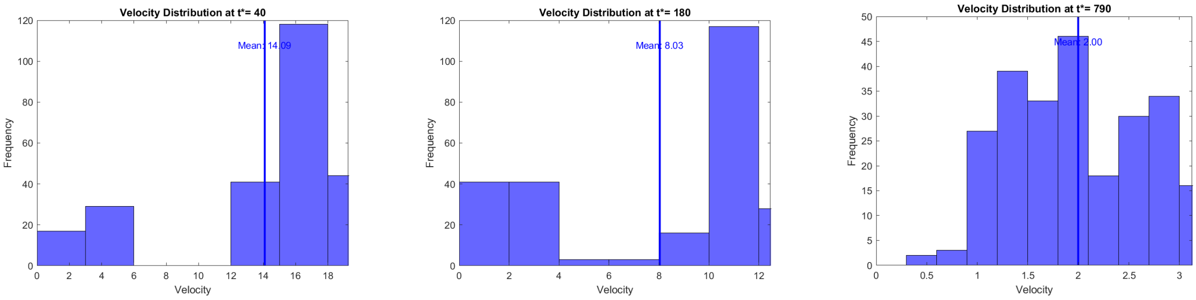

Figure C.13: The velocity distribution at several times for N_0=250, ϕ=5% and σ=0.2 (V_0=19.93).

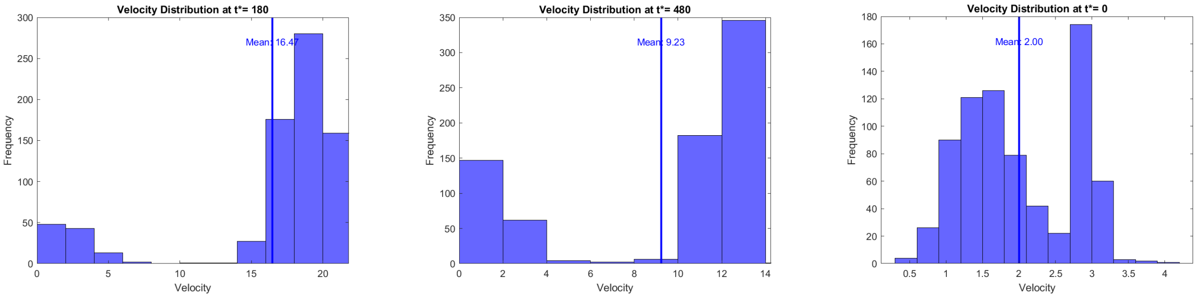

Figure C.14: The velocity distribution at several times for N_0=750, ϕ=1% and σ=0.2 (V_0=23.76).

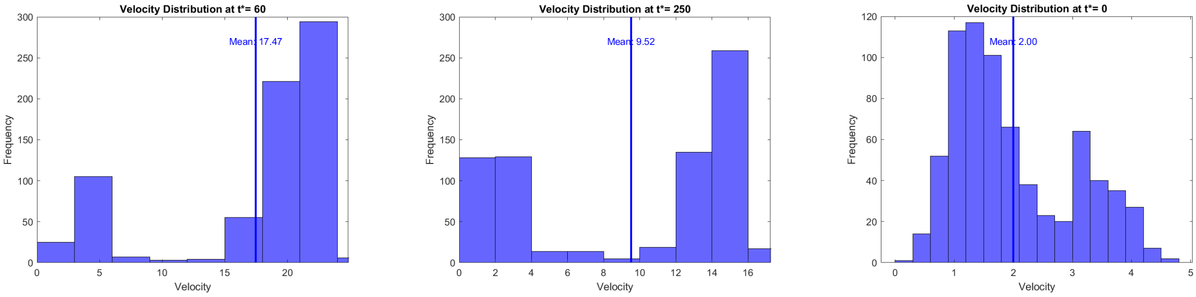

Figure C.15: The velocity distribution at several times for N_0=750, ϕ=1% and σ=0.4 (V_0=24.38).

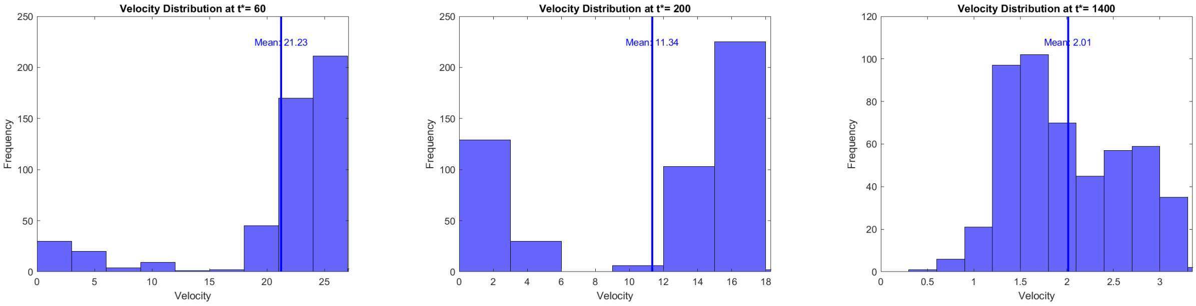

Figure C.16: The velocity distribution at several times for N_0=500, ϕ=5% and σ=0.2 (V_0=30.14).

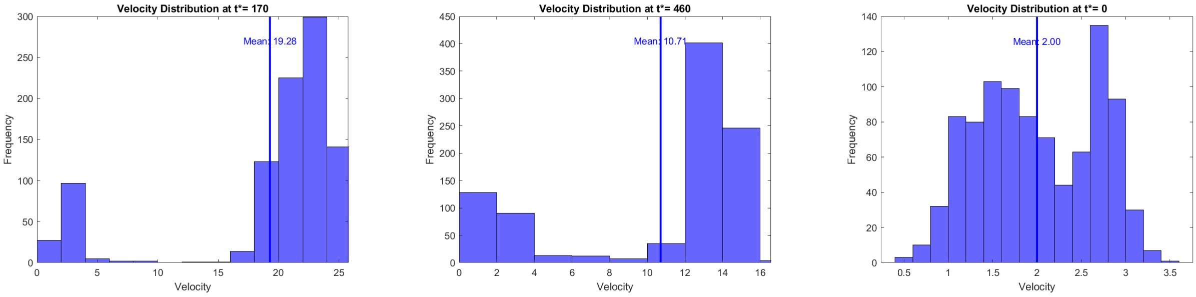

Figure C.17: The velocity distribution at several times for N_0=1000, ϕ=1% and σ=0.2 (V_0=28.16).

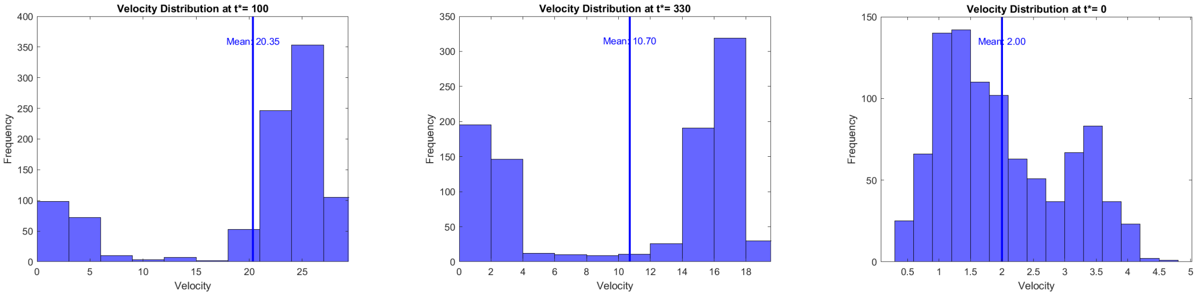

Figure C.18: The velocity distribution at several times for N_0=1000, ϕ=1% and σ=0.4 (V_0=28.43).

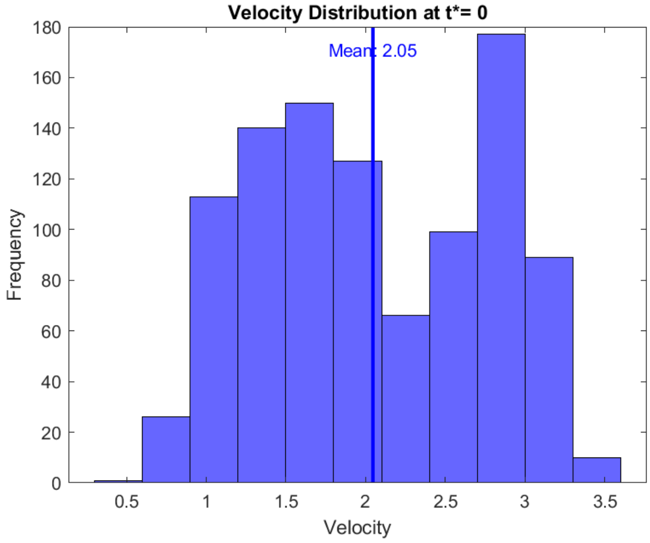

Figure C.19: The velocity distribution for N_0=1000, ϕ=1% and σ=0.2 (discrete particle size distribution).

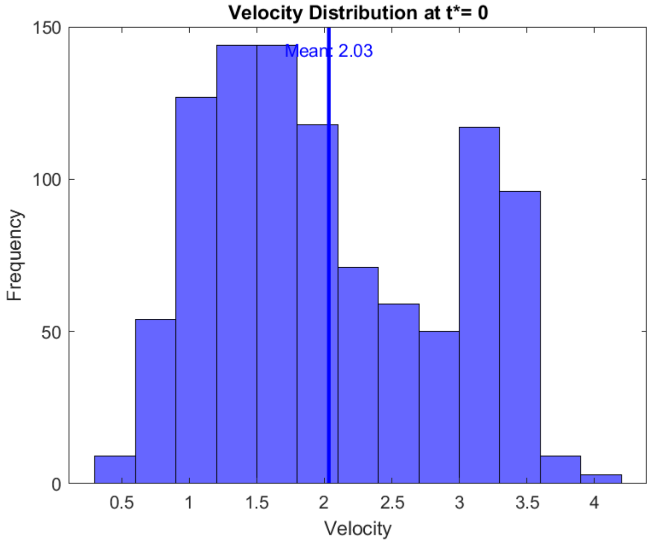

Figure C.20: The velocity distribution for N_0=1000, ϕ=1% and σ=0.3 (discrete particle size distribution).

D Size distributions in the cloud and tail

This section contains plots showing both static size distributions in the cloud and tail as well as the percentage of particles in the cloud belonging to a specific size range followed in time. This is shown for various σ, to show how these effects of particle segregation depend on the polydispersity.

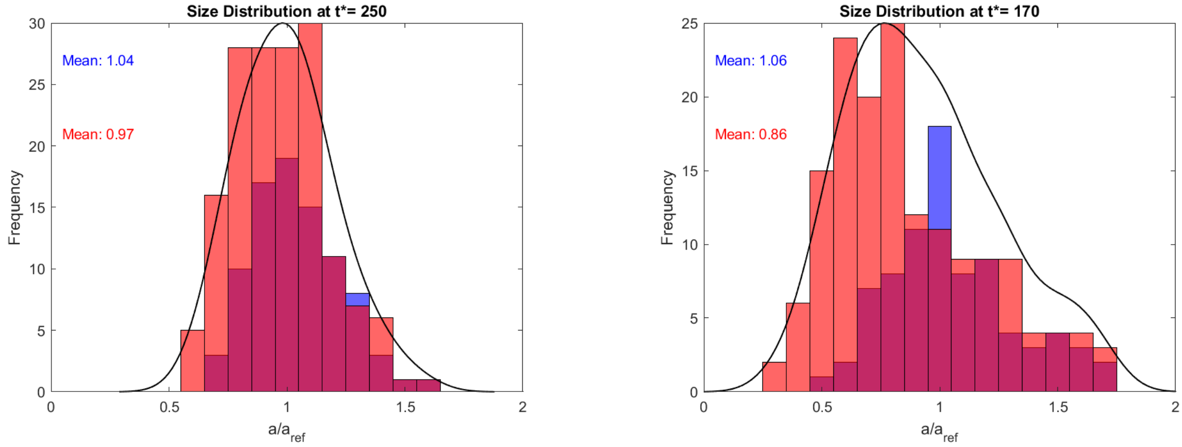

(a) $\sigma = 0.2$ (b) $\sigma = 0.4$

Figure D.1: The size distribution of two polydisperse particle clouds (N_0=250) at the time where the percentage of particles in the cloud has decreased to 35 %. The initial distribution of sizes inside the cloud is shown as a probability density function (PDF), but rescaled so that it is visible (the black curve). Sizes of particles belonging to the cloud are shown in blue and sizes of tail particles in red.

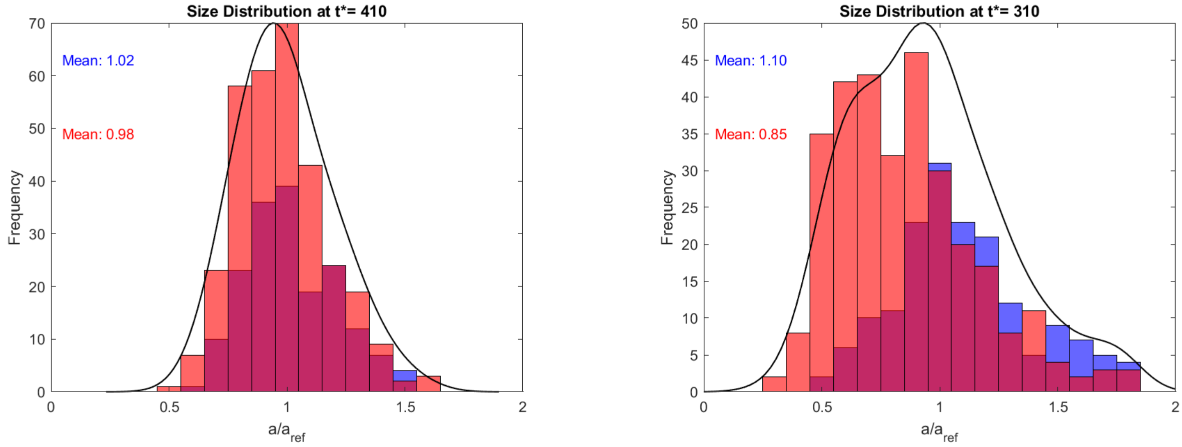

(a) $\sigma = 0.2$ (b) $\sigma = 0.4$

Figure D.2: The size distribution of two polydisperse particle clouds (N_0=500) at the time where the percentage of particles in the cloud has decreased to 35 %. The initial distribution of sizes inside the cloud is shown as a probability density function (PDF), but rescaled so that it is visible (the black curve). Sizes of particles belonging to the cloud are shown in blue and sizes of tail particles in red.

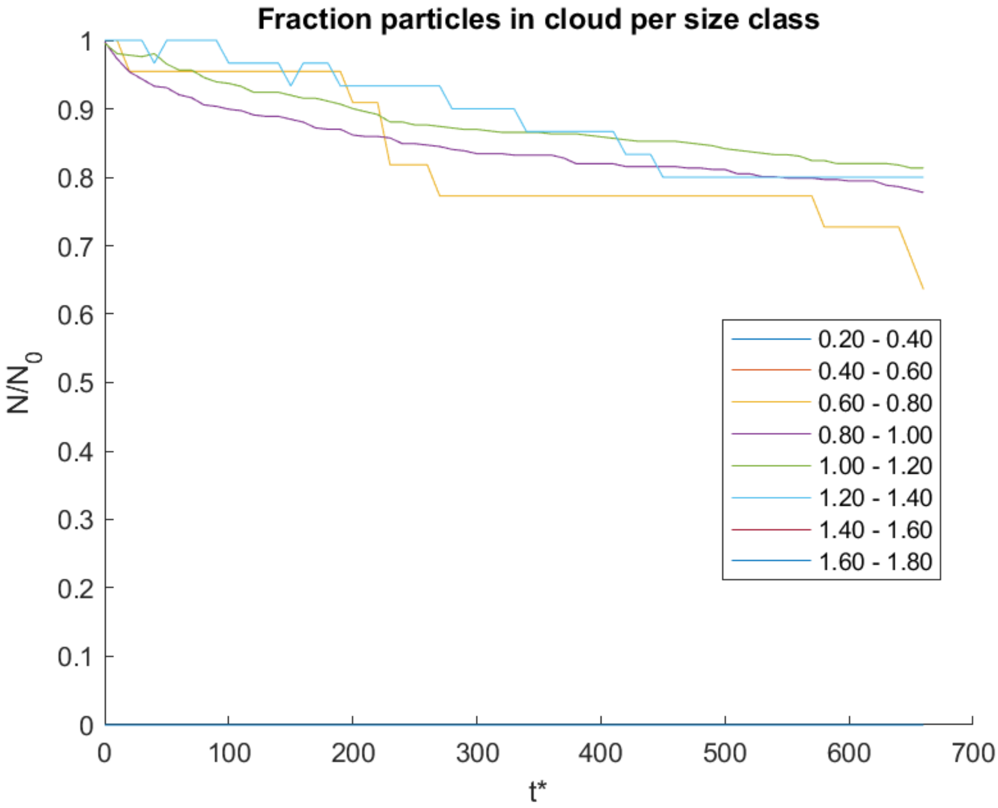

Figure D.3: The percentage of particles in the cloud (N_0=1000, ϕ=1%, σ=0.1) belonging to different size classes (size is relative to the mean).

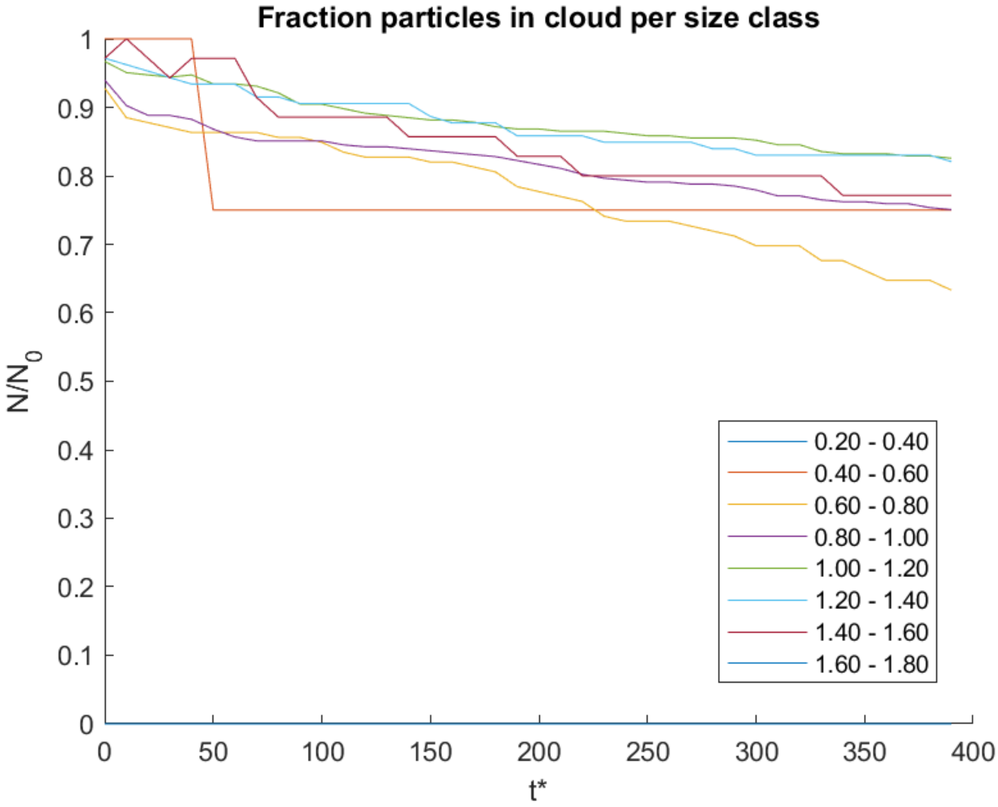

Figure D.4: The percentage of particles in the cloud (N_0=1000, ϕ=1%, σ=0.2) belonging to different size classes (size is relative to the mean).

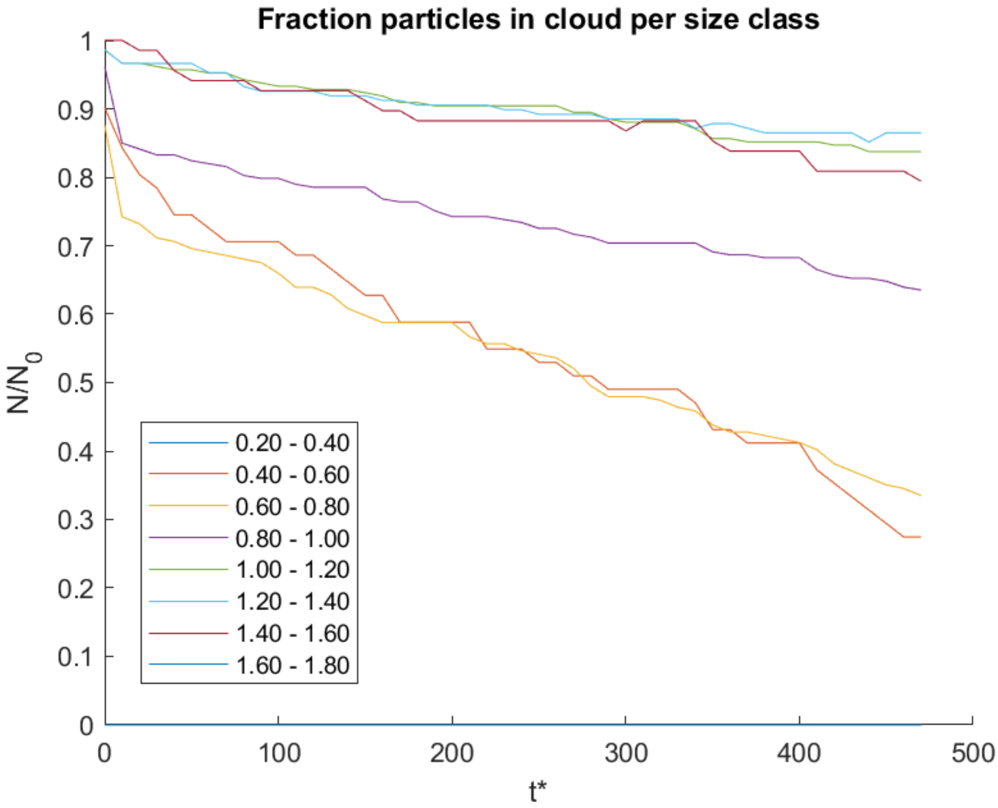

Figure D.5: The percentage of particles in the cloud (N_0=1000, ϕ=1%, σ=0.3) belonging to different size classes (size is relative to the mean).

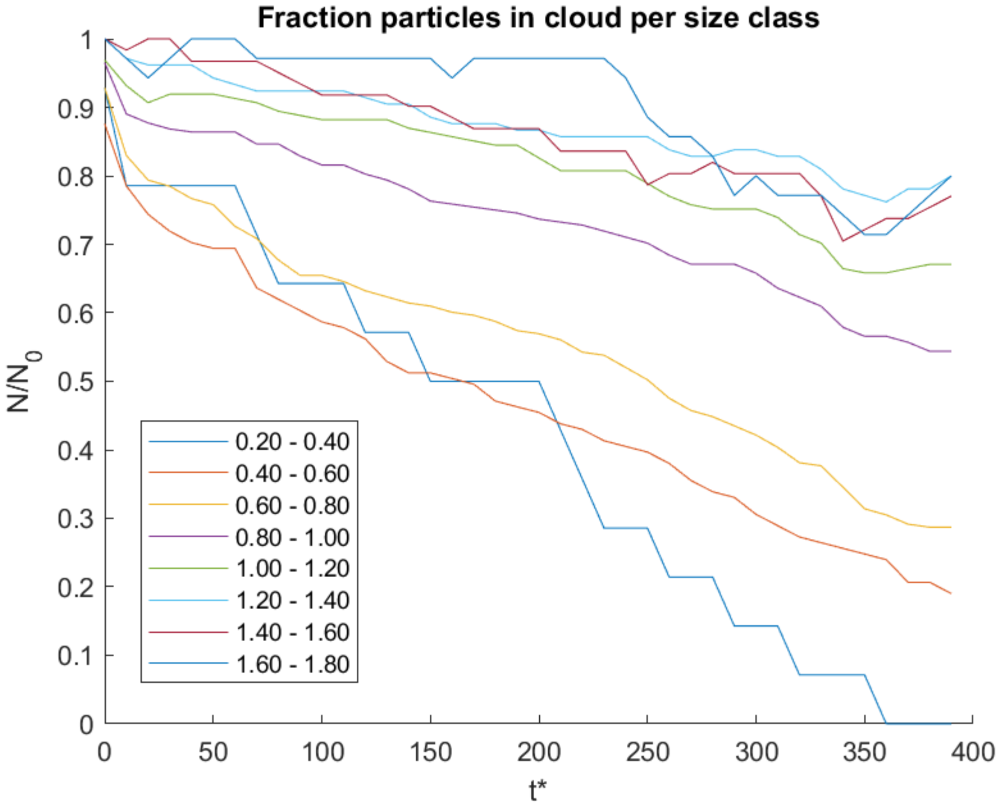

Figure D.6: The percentage of particles in the cloud (N_0=1000, ϕ=1%, σ=0.4) belonging to different size classes (size is relative to the mean).

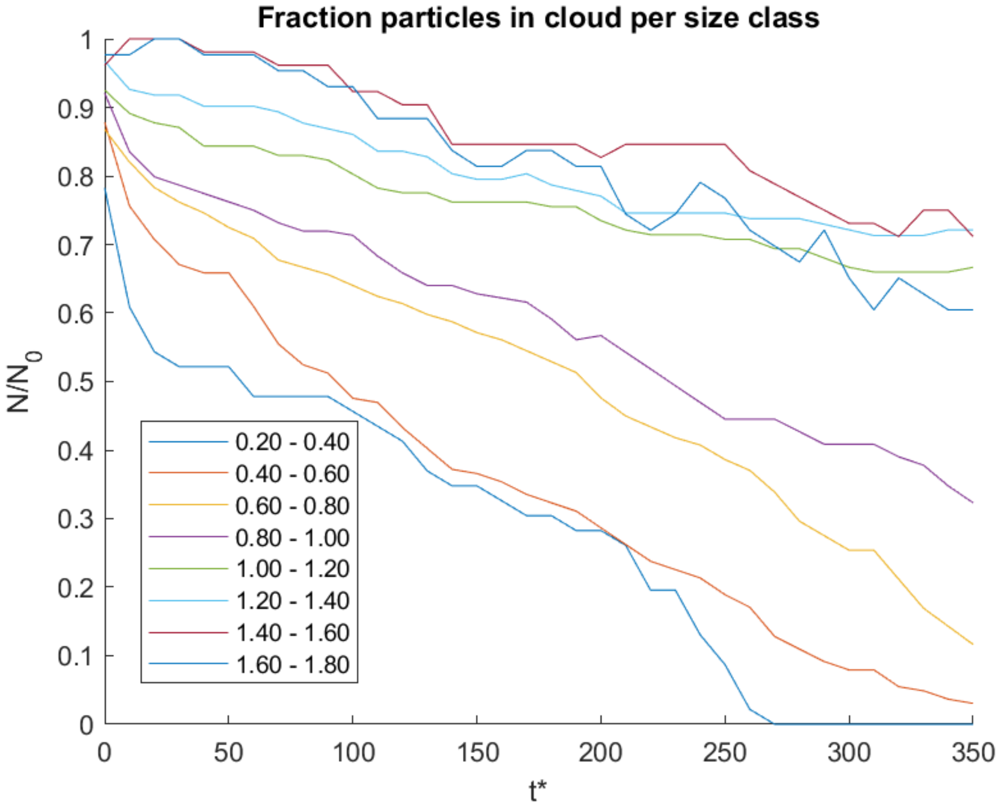

Figure D.7: The percentage of particles in the cloud (N$_0$=1000, ϕ=1%, σ=0.5) belonging to different size classes (size is relative to the mean).

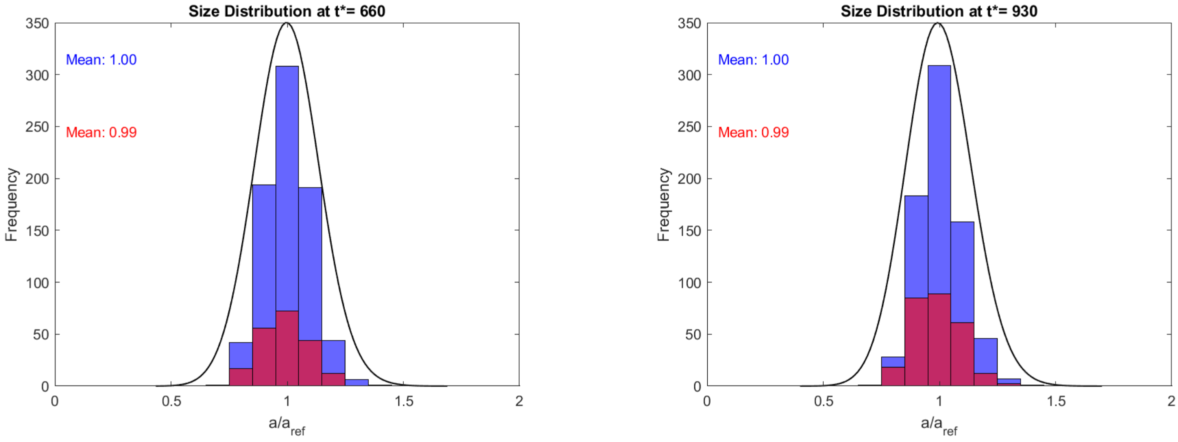

(a) σ=0.1 continuous PSD

(b) σ=0.1 discrete PSD

Figure D.8: The size distribution of two polydisperse particle clouds (left = continuous PSD, right = discrete PSD) at a time just before break-up of the cloud. The initial distribution of sizes inside the cloud is shown as a probability density function (PDF), but rescaled so that it is visible (the black curve). Sizes of particles belonging to the cloud are shown in blue and sizes of tail particles in red. For both clouds, N$_0$=1000 and ϕ = 1 %.

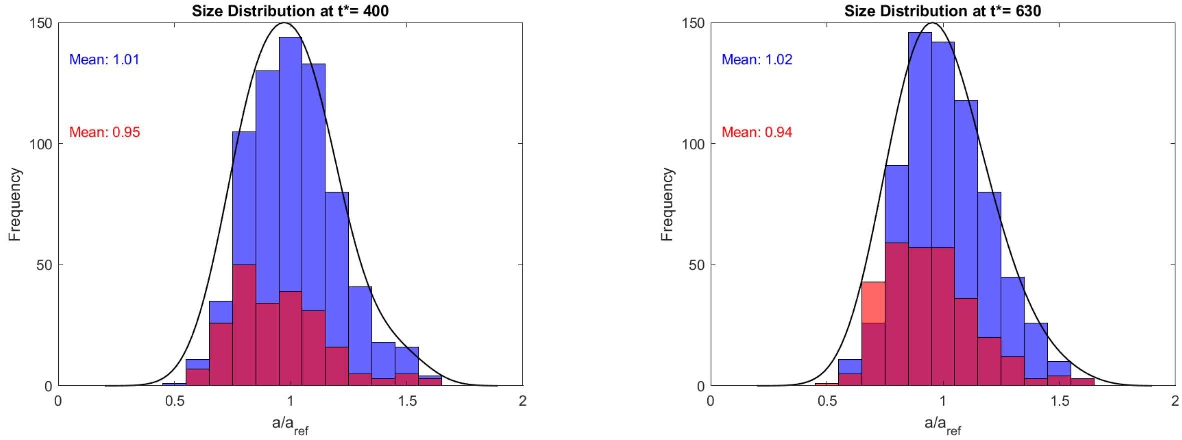

(a) σ=0.2 continuous PSD

(b) σ=0.2 discrete PSD

Figure D.9: The size distribution of two polydisperse particle clouds (left = continuous PSD, right = discrete PSD) at a time just before break-up of the cloud. The initial distribution of sizes inside the cloud is shown as a probability density function (PDF), but rescaled so that it is visible (the black curve). Sizes of particles belonging to the cloud are shown in blue and sizes of tail particles in red. For both clouds, N_0=1000 and ϕ = 1 %.

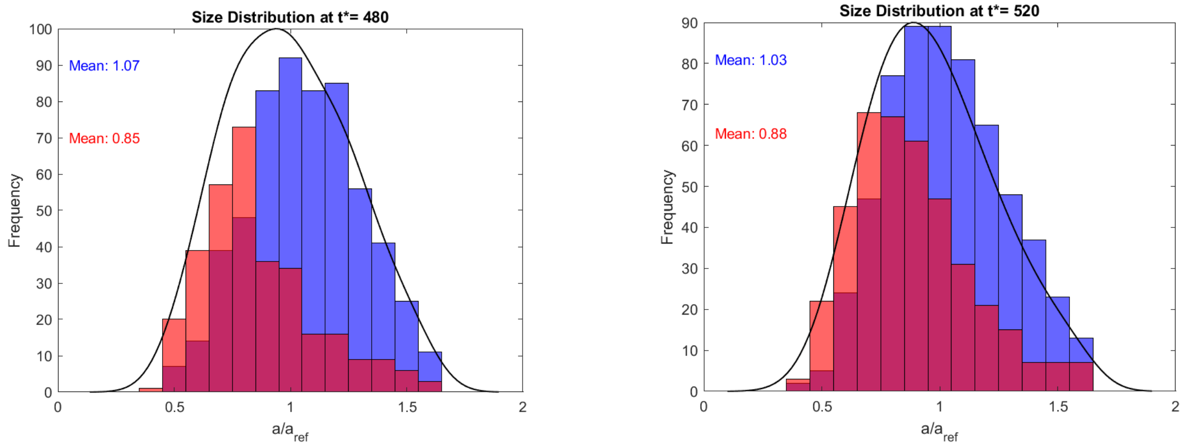

(a) σ=0.3 continuous PSD

(b) σ=0.3 discrete PSD

Figure D.10: The size distribution of two polydisperse particle clouds (left = continuous PSD, right = discrete PSD) at a time just before break-up of the cloud. The initial distribution of sizes inside the cloud is shown as a probability density function (PDF), but rescaled so that it is visible (the black curve). Sizes of particles belonging to the cloud are shown in blue and sizes of tail particles in red. For both clouds, N_0=1000 and ϕ = 1 %.

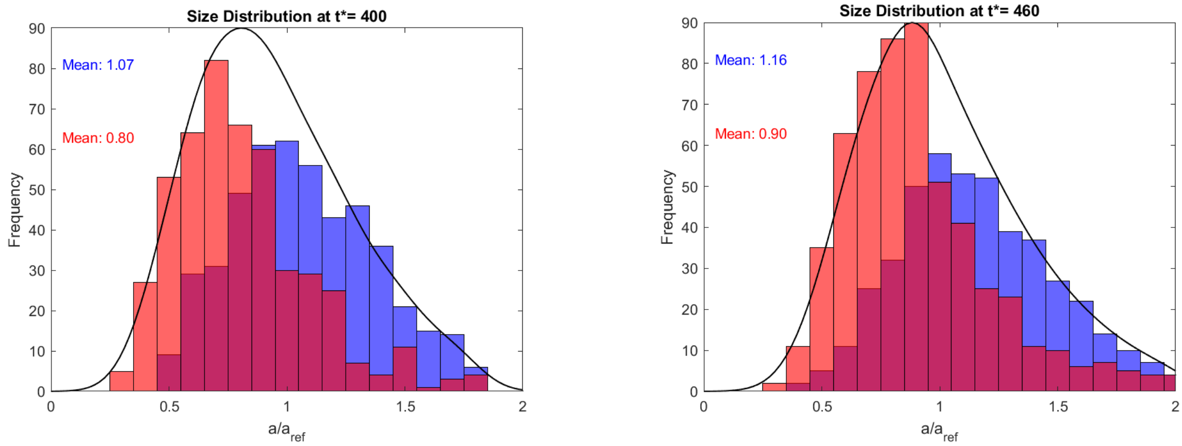

(a) σ=0.4 continuous PSD

(b) σ=0.4 discrete PSD

Figure D.11: The size distribution of two polydisperse particle clouds (left = continuous PSD, right = discrete PSD) at the time where the percentage of particles in the cloud has decreased to 35 %. The initial distribution of sizes inside the cloud is shown as a probability density function (PDF), but rescaled so that it is visible (the black curve). Sizes of particles belonging to the cloud are shown in blue and sizes of tail particles in red. For both clouds, N_0=1000 and $\phi = 1$ %.

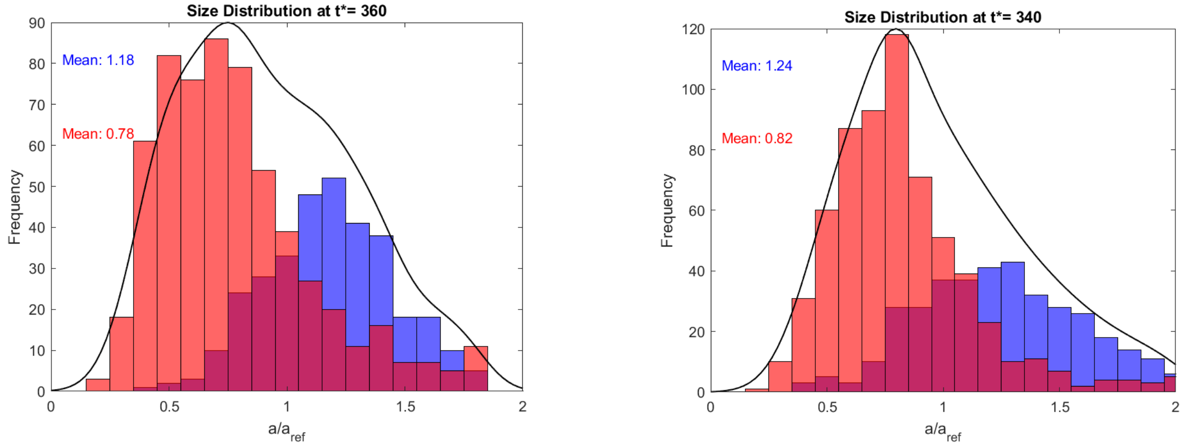

(a) σ=0.5 continuous PSD

(b) σ=0.5 discrete PSD

Figure D.12: The size distribution of two polydisperse particle clouds (left = continuous PSD, right = discrete PSD) at the time where the percentage of particles in the cloud has decreased to 35 %. The initial distribution of sizes inside the cloud is shown as a probability density function (PDF), but rescaled so that it is visible (the black curve). Sizes of particles belonging to the cloud are shown in blue and sizes of tail particles in red. For both clouds, N_0=1000 and $\phi = 1$ %.

E Plots of cloud velocity and leakage

This section contains plots of the relative cloud velocity and particle number for polydisperse clouds with a continuous and discrete size distribution and for several σ, showing clearly the increased leakage rate and subsequent deceleration with σ and the similarity between particle clouds with continuous and discrete particle size distributions.

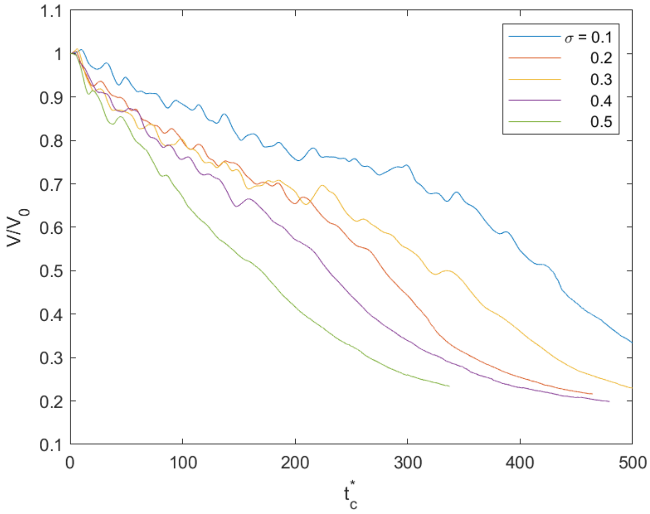

Figure E.1: The cloud velocity for clouds with varying polydispersity degrees with a continuous size distribution.

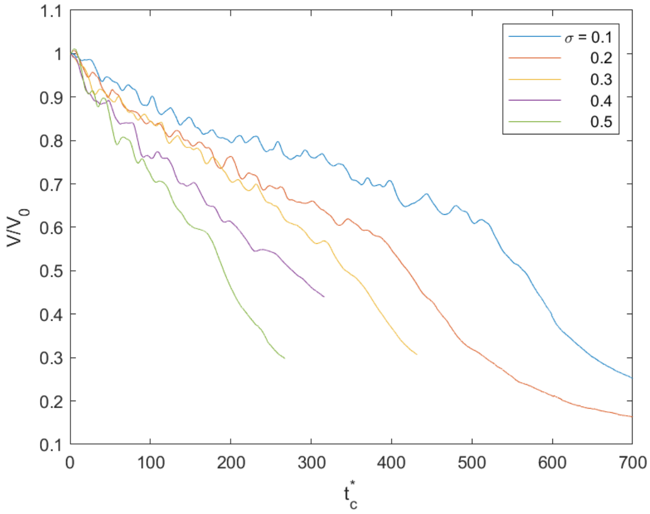

Figure E.2: The cloud velocity for clouds with varying polydispersity degrees with a discrete size distribution.

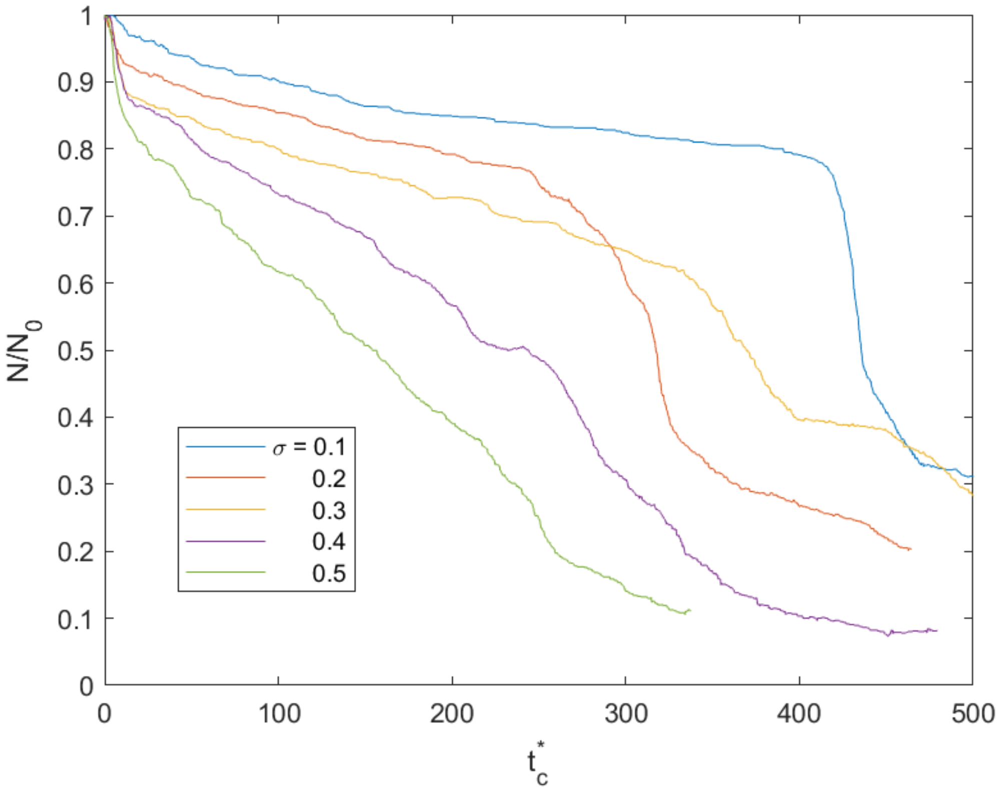

Figure E.3: The cloud relative particle number for clouds with varying polydispersity degrees with a continuous size distribution.

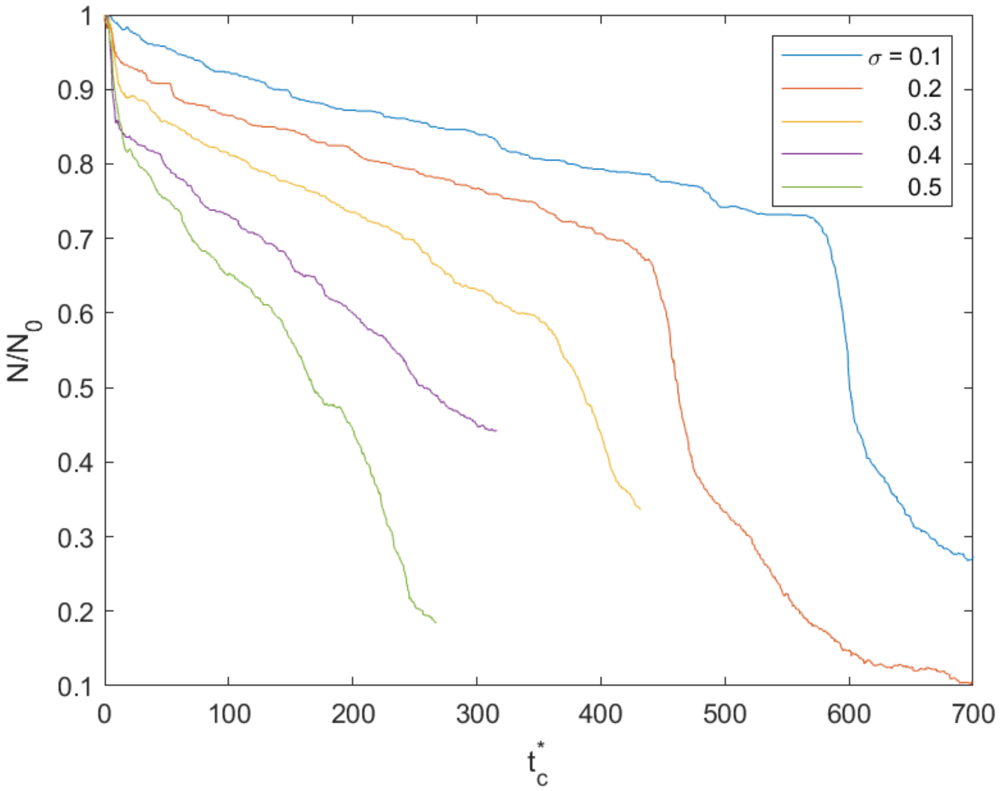

Figure E.4: The cloud relative particle number for clouds with varying polydispersity degrees with a discrete size distribution.

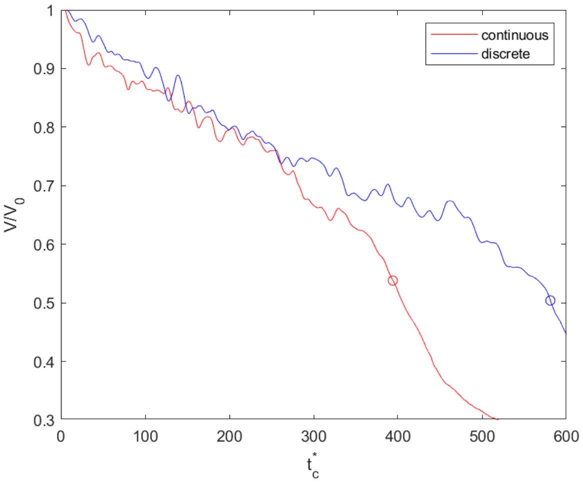
continuous
discrete
V/V$_0$
t_c^*
1
0.9
0.8
0.7
0.6
0.5
0.4
0.3
0
100
200
300
400
500
600

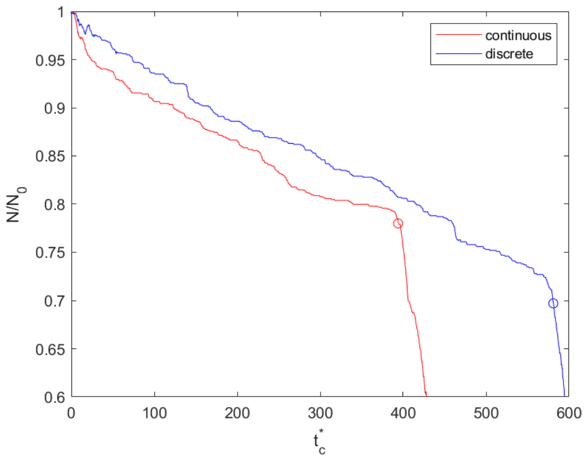
continuous
discrete
N/N$_0$
t_c^*
1
0.95
0.9
0.85
0.8
0.75
0.7
0.65
0.6
0
100
200
300
400
500
600

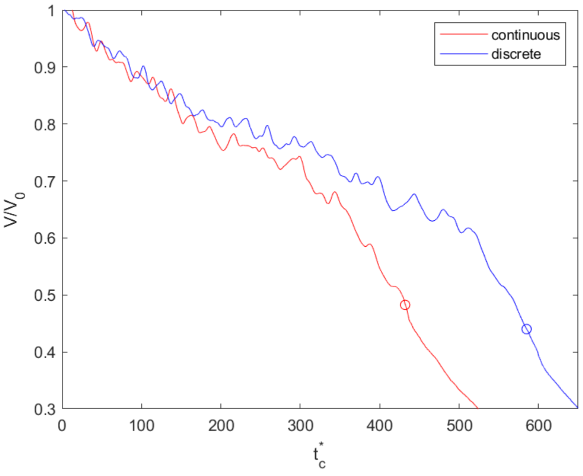
continuous
discrete
V/V$_0$
t_c^*
1
0.9
0.8
0.7
0.6
0.5
0.4
0.3
0
100
200
300
400
500
600

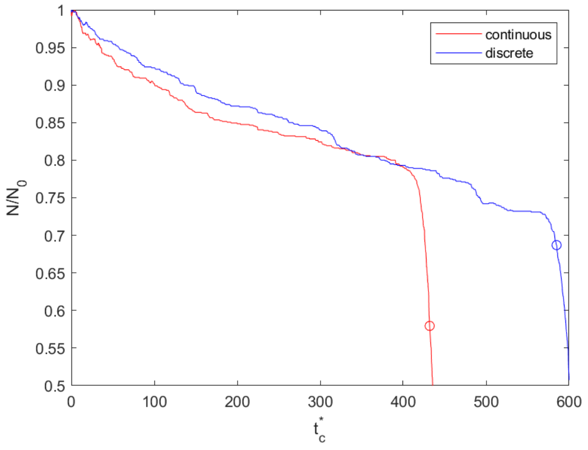
continuous
discrete
N/N$_0$
t_c^*
1
0.95
0.9
0.85
0.8
0.75
0.7
0.65
0.6
0.55
0.5
0
100
200
300
400
500
600

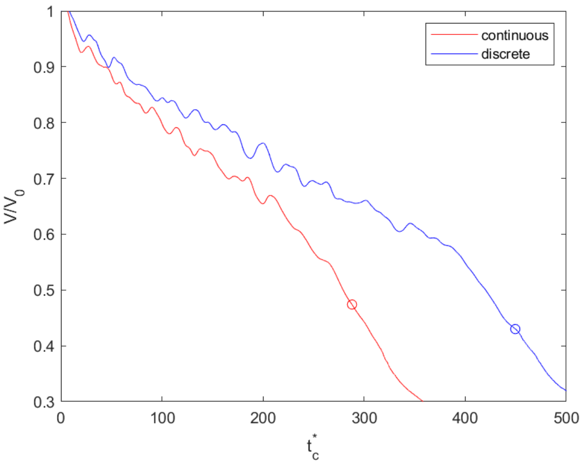
continuous
discrete
V/V$_0$
t_c^*
1
0.9
0.8
0.7
0.6
0.5
0.4
0.3
0
100
200
300
400
500

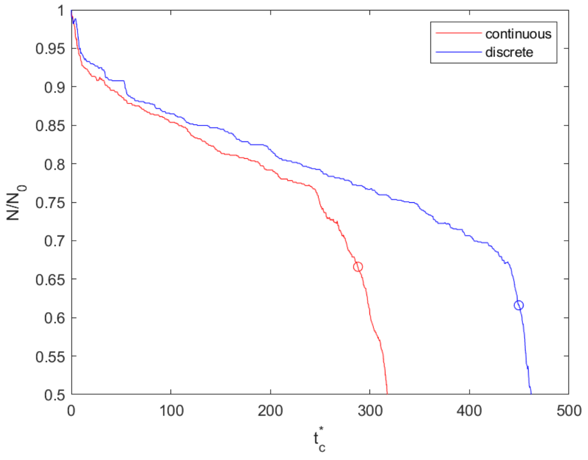
continuous
discrete
N/N$_0$
t_c^*
1
0.95
0.9
0.85
0.8
0.75
0.7
0.65
0.6
0.55
0.5
0
100
200
300
400
500

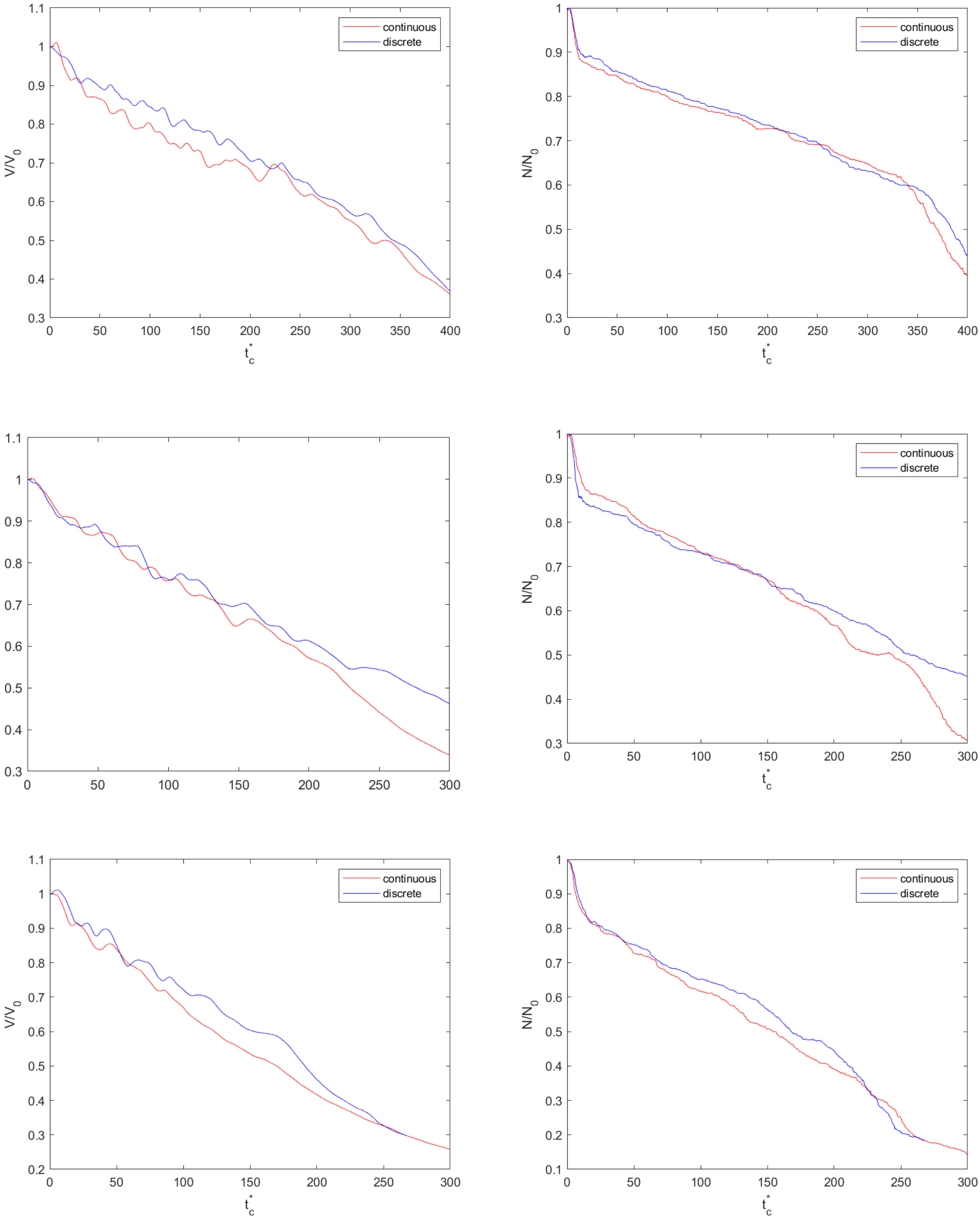

Figure E.6: The relative velocity and particle number of polydisperse particle clouds with continuous and discrete size distributions. The figures are in order of polydispersity degree for $\sigma = 0.05$, 0.1, 0.2, 0.3, 0.4 and 0.5. Circles indicate the moment of break-up.

F Preliminary results

This study was focused on finding the conditions for which average velocities measured from settling suspension drops reach velocities sufficiently close to the Stokes velocity. Now, we will provide a preliminary analysis to see what can be derived from the obtained data. Equations 40 - 47 give the size limit as a function of N_0 and ϕ. The relation can also be thought of as giving the maximum number of particles initially in the drop, as a function of the mean size and volume fraction. In practice, it is more convenient to have a direct relation between mean particle size and volume fraction. We can achieve this by fixing the size of the drop and, using an iterative method, find the (maximum) number of particles and volume fraction of the drop that satisfy the equations. We found that this procedure will always result in a curve (volume fraction against particle size) that can be very well described by a quadratic equation. For example, figure F.1 shows this curve for a suspension drop with volume 0.1 mL as well as the initial number of particles in the drop N_0. Note that if N_0 lies outside the interval that was studied here (100 to 1000), this is because of extrapolation of the data. If we disregard these cases, we would come to the conclusion that for a drop of volume 0.1 mL, the maximum mean particle size is 300 µm.

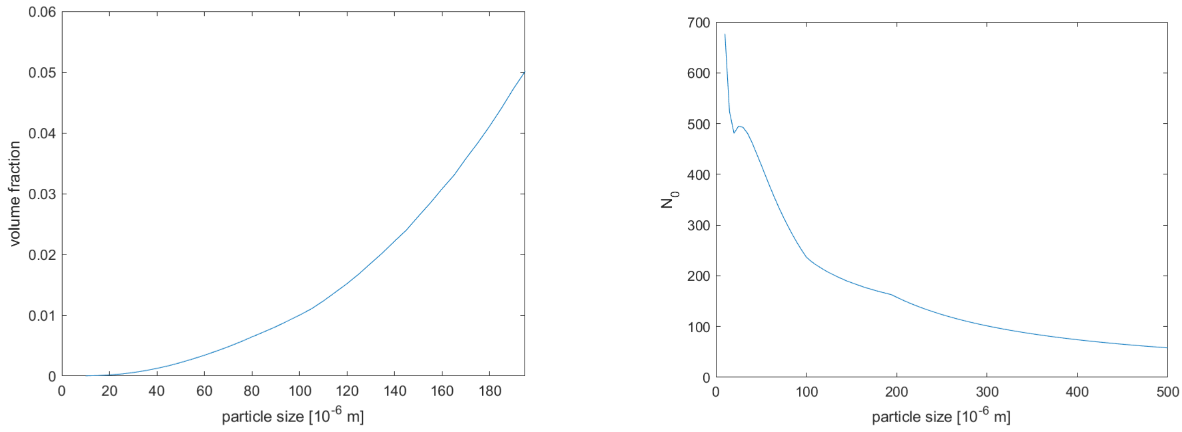

(a)

(b)

Figure F.1: Curve of (a) volume fraction and (b) number of particles against the size of the particles in the drop (monodisperse case) for a drop of volume 0.1 mL.

The tank height, or rather the height at which the particles' velocities are measured relative to the discharge point, is very important as it determines the available distance particles can travel (and decelerate). Figure F.2 shows the curves for two different tank heights. A tank height of 25 cm instead of 100 cm will result in a quarter the size limit (or maximum N_0). This leads to a less dense drop in case of fixed volume. For the small tank, it is clear that the drop will only contain a significant amount of particles for small particle sizes. For particle size greater than 50 µm, N_0 falls outside the scope of this study, indicating the importance of tank height. Note that the curve for the one meter high tank cuts off at a certain size only because of reaching the maximum volume fraction.

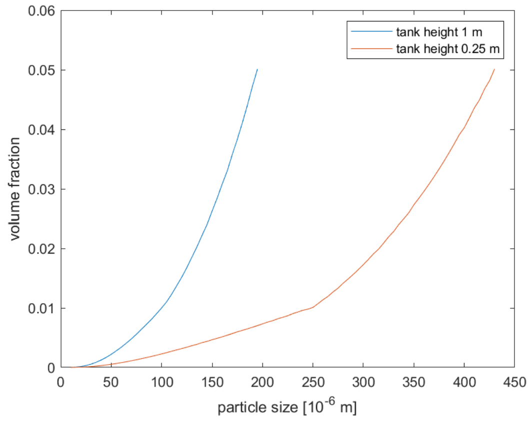

(a) (b)

Figure F.2: Curve of (a) volume fraction and (b) number of particles against the size of the particles in the drop (monodisperse case) for a drop of volume 0.1 mL, for two different tank heights.

We repeated the same analysis for polydisperse drops. To this end, we used the data corresponding to $\sigma \approx 0.3$. The results are shown in figures F.3 - F.4, for two different drop sizes. The most important difference is that the polydisperse drops (are allowed to) contain more particles, which is favorable for the experiments as there will be less margin for error. Due to the higher N_0, the prepared suspension will need to be slightly more dense for the same particle size. For the larger drop, the maximum volume fraction is reached at larger particle size, in both cases. Here, it can be seen that with an increased drop size and a polydisperse drop, the range of N_0 for particle sizes until 500 m is now contained within the studied interval (100-1000). Note that for small sizes, N_0 for the polydisperse drop will exceed 1000 because of extrapolation, but as this value is the maximum number of particles this does not limit the particle size.

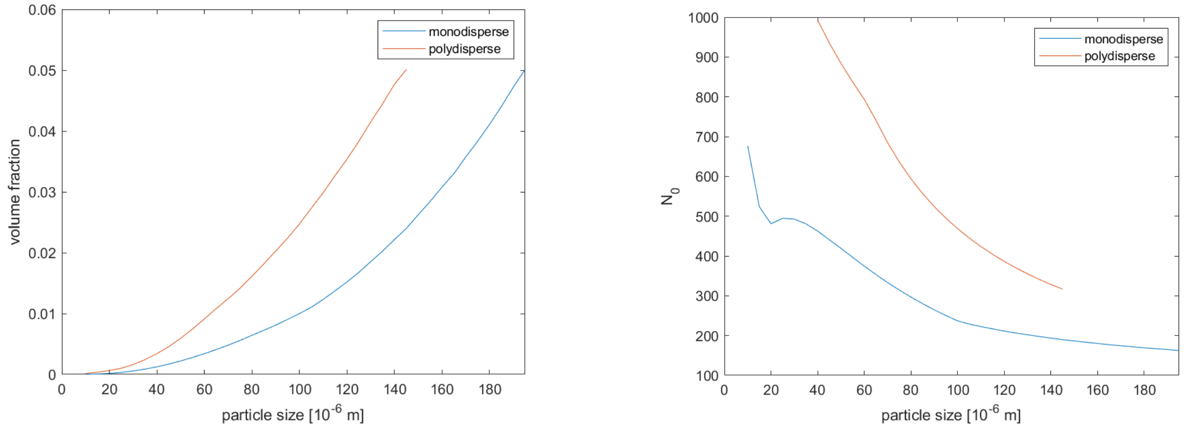

(a) (b)

Figure F.3: Curve of (a) volume fraction and (b) number of particles against the size of the particles in the drop (monodisperse case) for a monodisperse and polydisperse drop of volume 0.1 mL.

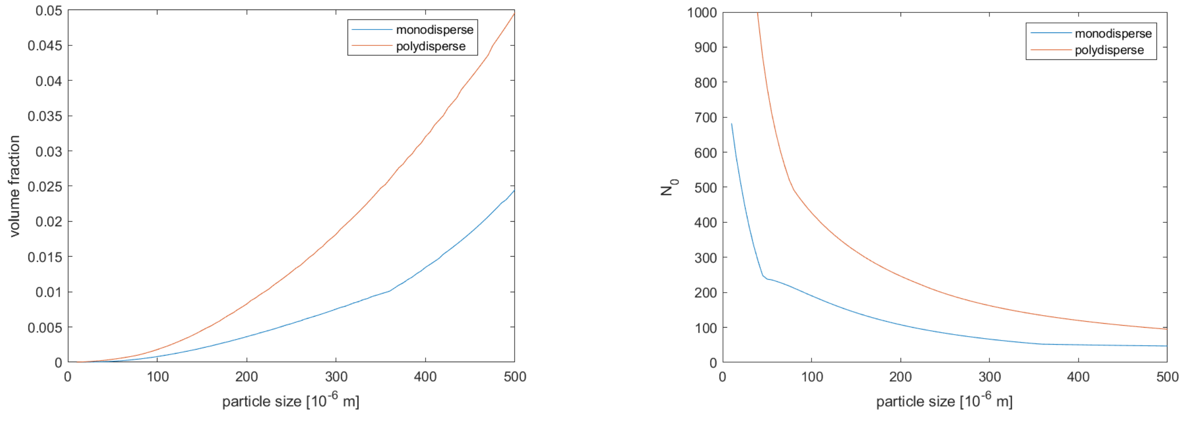

(a) (b)

Figure F.4: Curve of (a) volume fraction and (b) number of particles against the size of the particles in the drop (monodisperse case) for a monodisperse and polydisperse drop of volume 1 mL.

Finally, we noted that using the mean size for calculating the volume gives an error in the case of highly polydisperse suspensions, because the radii are cubed to obtain the volume, i.e. $\langle a \rangle \neq \frac{1}{N}\sum_i a_i^3$. Figure F.5 shows the difference in the resulting curves. For larger sizes, the difference in required volume fraction is significant.

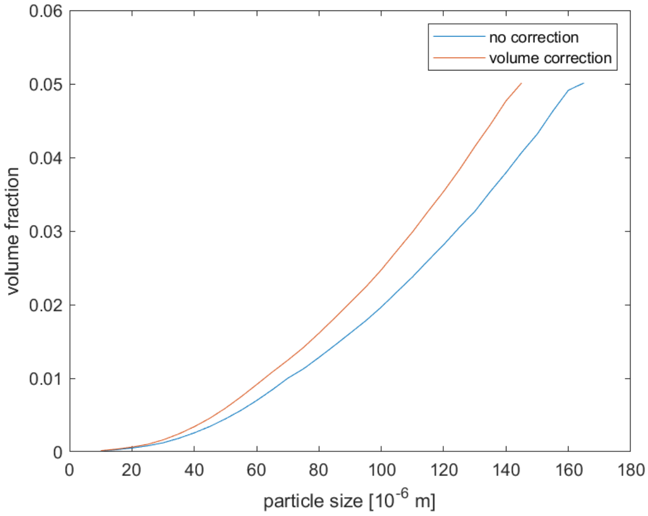

Figure F.5: The volume fraction of the suspension drop against the size of the particles in the drop for a polydisperse drop, using either the mean size of particles for calculation of the volume or the actual expected volume according to the size distribution.